ABSTRACT

Title of Document: BOTTOM-UP MULTIFERROIC NANOSTRUCTURES.

Shenqiang Ren, Doctor of Philosophy, 2009

Directed By: Professor Manfred Wuttig
Department of Materials Science and Engineering

Multiferroic and especially magnetoelectric (ME) nanocomposites have received extensive attention due to their potential applications in spintronics, information storage and logic devices. The extrinsic ME coupling in composites is strain mediated via the interface between the piezoelectric and magnetostrictive components. However, the design and synthesis of controlled nanostructures with engineering enhanced coupling remain a significant challenge. The purpose of this thesis is to create nanostructures with very large interface densities and unique connectivities of the two phases in a controlled manner. Using inorganic solid state phase transformations and organic block copolymer self assembly methodologies, we present novel self assembly "bottom-up" techniques as a general protocol for the nanofabrication of multifunctional devices.

First, Lead-Zirconium-Titanate/Nickel-Ferrite (PZT/NFO) vertical multilamellar nanostructures have been produced by crystallizing and decomposing a gel in a magnetic field below the Curie temperature of NFO. The ensuing microstructure is nanoscopically periodic and anisotropic. The wavelength of the

PZT/NFO alternation, 25 nm, agrees within a factor of two with the theoretically estimated value. The macroscopic ferromagnetic and magnetoelectric responses correspond qualitatively and semi-quantitatively to the features of the nanostructure. The maximum of the field dependent magnetoelectric susceptibility equals 1.8 V/cm Oe.

Second, a magnetoelectric composite with controlled nanostructures is synthesized using co-assembly of two inorganic precursors with a block copolymer. This solution processed material consists of hexagonally arranged ferromagnetic cobalt ferrite (CFO) nano-cylinders within a matrix of ferroelectric Lead-Zirconium-Titanate (PZT). The initial magnetic permeability of the self-assembled CFO/PZT nanocomposite changes by a factor of 5 through the application of 2.5 V. This work may have significant impact on the development of novel memory or logic devices through self assembly techniques. It also demonstrates a universal two-phase hard template application.

Last, solid-state self assembly had been used recently to form pseudoperiodic chessboard-like nanoscale morphologies in a series of chemically homogeneous complex oxide systems. We improved on this approach by synthesizing a spontaneously phase separated nanolamellar $BaTiO_3$-$CoFe_2O_4$ bi-crystal. The superlattice is magnetoelectric with a frequency dependent coupling. The $BaTiO_3$ component is a ferroelectric relaxor with a Vogel-Fulcher temperature of 311 K. Since the material can be produced by standard ceramic processing methods, the discovery represents great potential for magnetoelectric devices.

BOTTOM-UP MULTIFERROIC NANOSTRUCTURES.

By

Shenqiang Ren

Dissertation submitted to the Faculty of the Graduate School of the
University of Maryland, College Park, in partial fulfillment
of the requirements for the degree of
Doctor of Philosophy
2009

Advisory Committee:
Professor Manfred Wuttig, Chair/Advisor
Professor Ichiro Takeuchi
Professor Lourdes Salamanca-Riba
Dr. James Cullen
Professor John Cumings
Professor H. Dennis Drew (Dean's Representative)

Dedication

This work is dedicated to my family.

Acknowledgements

"Where there is a will, there is a way."

I would like to express my very gratefulness to my thesis advisor, Professor Manfred Wuttig, for his insightful guidance, persistent support and enthusiastic encouragement throughout the course of my doctoral work. I really appreciate the abundant freedom he gave me in conducting my ideas reflected in this dissertation. Actually I have been consistently impressed by such freedom which I consider vital in my research since our first chat over the phone when I was still in Nanjing, China in 2004. I have also benefited a lot from our frequent discussions in which his remarkable insights, enlightenment, intelligence, rigorous scholarship and dedication to science instilled me in every aspect of my daily research. I deeply appreciate the tremendous time and sincere efforts he made discussing my projects and advising me. It would not have been possible to accomplish my scientific goals without his guidance.

I wish to express my great gratitude to Professor Robert M. Briber for his knowledgeable guidance in the study of self-assembly of block copolymer for templating multifunctional nanostructures. I appreciate his valuable comments and support on my presentations at APS conference and Dean Award competition. I would also like to thank Professor Ichiro Takeuchi for his great support in providing me access to facilities in the Center for Nanophysics and Advanced Materials in this study and his kindness to serve for my thesis committee. I would profoundly like to thank Professor Lourdes Salamanca-Riba for teaching me to perform the optical reflection and diffraction measurement. I am also grateful to Professor Isabel K. Lloyd who provided me access to TGA, DTA instruments and the space in her lab to prepare my sol-gel precursors. I am also grateful to Professor John Cumings for his valuable advice on Lorentz-TEM and Matlab simulation. I also thank Professor Peter Kofinas for dielectric measurement system.

I would like to thank Prof. H. Dennis Drew for taking time out of his busy schedule to serve on my committee and evaluate my work. I want to thank Dr James Cullen for his advice on magnetic materials and his kindness to serve for my thesis committee. I thank all the members for taking time to read this dissertation for doing me the honor of serving on my committee.

I wish to thank my previous undergraduate academic advisor Professor Luqian Weng in China for his special encouragement. I am also grateful for the help, assistance and friendship of my colleagues, Dr. Peng Zhao, Dr. Liyang Dai, Lei Zheng. I thank all my friends at Maryland for their support, Dr. Tai-I Yang, Dr. Shixong Zhang, Dr. S.-H. Lim, Yueying Liu, Richard Bergstrom Jr., Dr. Yi Qi, Dr. Jason Hattrick-Simpers, Christopher Metting, Dr. Xin Zhang, Dr. Yijun Wang, Parag Banerjee and Chris Long,

Finally, I am very thankful to my parents in China, my mother-in-law in China, my grandmother in heaven for their continuous care and supports from a distance. I also would like to express my special appreciations to my very supportive and talented wife, Xin Zhao. Without her, I would not have got to this exciting moment. Thank you for being always understanding and caring.

Table of Contents

Dedication ii
Acknowledgements iii
Table of Contents v
List of Tables vii
List of Figures viii

Chapter 1 Introduction 1
  1.1 Multifunctional Materials 1
  1.2 Magnetoelectric Composite Materials 2
  1.3 Magnetoelectric Nanocomposite Thin Film 8
  1.4 Motivation of this Thesis 10
  1.5 Contents of this Thesis 12

Chapter 2 Solution Processing of Multiferroic Nanostructures 14
  2.1 Bottom-Up versus Top-Down 15
  2.2 Spinodal Decomposition 17
  2.3 Self-Assembly of Block Copolymer 21
  2.4 Eutectic Reaction 24
  2.5 Material Component of the Thesis 25

Chapter 3 Pseudo-Spinodally Decomposed Multiferroic Nanostructures 28
  3.1 Introduction 28
  3. 2 Pseudo-Spinodally Decomposed PZT-$NiFe_2O_4$ under Magnetic Field 29
  3.3 Growth Kinetics of PZT-$NiFe_2O_4$ Nanostructures 34
    3.3.1 Temperature Dependence 35
    3.3.2 Magnetoannealing Time Dependence 36
    3.4.3 Thickness Evolution of PZT-$NiFe_2O_4$ Nanostructure 38
  3.4 Ferroelectric /Magnetic Properties in PZT-$NiFe_2O_4$ Nanostructures 40
  3.5 Magnetoelectric Coupling Effect in PZT-$NiFe_2O_4$ Nanostructures 41

Chapter 4 Self-Assembled Multiferroic Nanostructures through Block Copolymer. 45
  4. 1 Introduction 45
  4. 2 Preparation 47
  4.3 Self-Assembled PZT-$CoFe_2O_4$ Nanostructure 48
  4.4 Ferroelectric Property in PZT-$CoFe_2O_4$ Nanostructures 54
  4.5 Magnetoelectric Coupling Effect in PZT-$CoFe_2O_4$ Nanostructures 56
  4. 6 Numerical Calculation of Dipole and Magnetoelectric Energies 57
  4.7 Vertical Multilamellar Ordered Nanostructure through Block Copolymer 60

Chapter 5 Spontaneous Phase Separated Multiferroic Bi-Crystal 68
  5. 1 Introduction 68
  5.2 Self-Assembled $BaTiO_3$-$CoFe_2O_4$ Nanostructures 69
  5. 3 Ferroelectric Properties of $BaTiO_3$-$CoFe_2O_4$ Nanostructures 73
  5. 4 Magnetic Properties of $BaTiO_3$-$CoFe_2O_4$ Nanostructures 75

5. 5 Magnetoelectric Coupling of $BaTiO_3$-$CoFe_2O_4$ Nanostructures 76

Chapter 6 Summary and Future Work 79

Chapter 7 Appendix: Experimental Technique 83
  7.1 Sol-Gel and Chemical Solution Deposition 83
  7. 2 Structure Characterization 87
    7.2.1 X-Ray Diffraction 88
    7.2.2 Transmission Electron Microscopy 88
    7.2.3 Atomic Force Microscopy (AFM) 89
  7.3 Electric Measurement 91
  7.4 Magnetic Measurement 92
    7.4.1 Vibration Sample Magnetometer 93
    7.4.2 Superconducting Quantum Interference Device Magnetometer 94
  7.5 Magnetoelectric Measurement 95

Bibliography…………………………………………………………………..106

Publication.…………………………………………………………………….116

List of Tables

Table i Multiferroic single phase……………..…………………………………...….14

Table ii Multiferroic composite systems…………………………………………...…16

Table iii Lattice compatibility of different FE-FM systems………………………...35

Table iv Theoretical and experimental values of the anisotropy energy...................64

Table v Evaluation of the Dipole Interaction energies U…………………………..67

List of Figures

Figure 1.1 Roadmap of this thesis……………………………………………………..11

Figure 1.2 Multiferroic oxides. The largest circle indicates the insulating oxides: electrically polarizable materials (green ellipse) and magnetically polarizable materials (orange ellipse). Within the ellipse, the circle indicates materials with a finite polarization (ferroelectrics) and/or a finite magnetization (ferro- and ferrimagnets). Depending on the definition, multiferroics correspond to the intersection between the ellipses or the circles. The small circle in the middle represents systems exhibiting a magnetoelectric coupling...13

Figure 1.3 Dependence of magnetic-field-induced electric polarization $P_3=P_3(\mathrm{H}_e// x_3)-P_3(\mathrm{H}e//x_1)$ on the film thickness h. ……………..……………….……..20

Figure 1.4 Schematic illustration of a nano‘1-1’ composite structure on a substrate (left) and hexagonally ordered “3-1” composite structure on a substrate (right) ……………..…………..……………………………………...……..21

Figure 2.1 Two approaches to control matter……………………..………………23

Figure 2.2 The multiferroic composite nanostructures prepared by “top-down” approach………………………………………………..…………….….……..25

Figure 2.3 The eutectic magnetoelectric BTO-CFO composite microstructure ...….27

Figure 2.4 Typical spinodal decomposition showing well-defined periodicities and separated phases...28

Figure 2.5 Spinodal decomposition of binary alloy with miscibility gap ……...….29

Figure 2.6 Electron graphs of Ticonal XX alloy. a). Left shows microstructure for applied magnetic field along perpendicular direction b), Right shows microstructure for magnetic field parallel to plane ……………………..….30

Figure 2.7 Architecture of 3D chessboard nanostructures……………..……...…….. ..32

Figure 2.8 Figure 2.8 Phase diagram of diblock copolymer melt and schematic representation of a symmetric AB diblock copolymer. L denotes the lamellar morphology, H - hexagonal, G - gyroid, C- spherical morphology, D – disordered state. ………..34

Figure 2.9 Schematic diagram of 50/50 ratio PS-b-PEO block copolymer system combined with ferromagnetic-ferroelectric $CoFe_2O_4$-PZT sol-gel precursors ……………………………………………………………...…...36

Figure 3.1 Create lamellar composite by Spinodal Decomposition…………..………..39

Figure 3.2 The DTA measurement of PZT/NFO sample………………...…………..40

Figure 3.3 Microscopic characterization of the synthesized PZT/NFO composite. above; TEM image of PZT/NFO sample annealed 2 hours at 460 ^{0}C. The inset shows the diffraction pattern of the as-spun amorphous state of the composite, middle; TEM image of a PZT/NFO sample annealed 12 hours at 480 ^{0}C, i.e. below the Curie temperature of NFO, in an in-plane magnetic field H_a=0.6 Tesla indicated by the arrow. The inset represents the diffraction pattern of the displayed structure, below; same as left but annealed in an out-of-plane magnetic field H_a=0.6 Tesla as indicated..42

Figure 3.4 Standing compositional waves in the PZT/NFO composite. The noise of this compositional analysis does not permit statements about the exact composition of the PZT and NFO regions. However, it can be seen that the concentration of the two groups of elements, Pb, Zr, Ti and Ni, Fe, forming the PZT and NFO components of the composite are maximized in a periodic fashion. The power Fourier transform displayed at the upper right indicates the existence of two waves. The four maxima indicate their mutual phase shift of ½λ..42

Figure 3.5 Temperature dependence microstructure. (a) Gel state 200 ^{o}C (b) Amorphous decomposing state 350 ^{o}C. (c) Amorphous decomposed state 400 ^{o}C. (d) Crystallized decomposed state 480 ^{o}C……………..……….45

Figure 3.6 Magnetoannealing time dependence microstructure at 500 ^{o}C. (a) 1 hour. (b) 4 hours. (c) 9 hours. (d) 16 hours (f) 25 hours...................................46

Figure 3.7 Thin film thickness dependence microstructure at 500 ^{o}C and 4 hours. (a) 100 nm. (b) 150 nm. (c) 200 nm. (d) 250 nm..48

Figure 3.8 MFM image of PZT/NFO sample…………………………..……..…..49

Figure 3.9 Ferromagnetic and Ferroelectric characteristics of a PZT/NFO composite annealed for 12 hours at 480^{0}C in an in-plane maagnetic field of H_a=0.6 T. left, $\vec{H}_a \parallel \vec{H} \perp \vec{k}$, $\vec{H}_a \perp \vec{H} \parallel \vec{k}$. The shaded area represents the difference of the demagnetization energies of a rotation ellipsoid parallel and perpendicular to its long axis. Right, ferroelectric P-E loop measurement. ……………………………………………………..…….50

Figure 3.10 Magnetoelectric characteristic and ME susceptibilities (upper inset) of a PZT/NFO film composite annealed for 12 hours at 480^{0}C in an in-plane magnetic field H_a= 0.6 T. ▬ ∗∗∗ $\vec{H}_a \perp \vec{H} \| \vec{k}$; ▬ ○○○, $\vec{H}_a \perp \vec{H} \| \vec{k}$. The inset on the lower right indicates the placement of the electrodes..51

Figure 3.11 Schematic for the evaluation of $<E_{\|}>$ and $<E_{\perp}>$………………………..52

Figure 4.1 Schematic diagram to generate nanoscopic dot array of inorganic materials on PS-*b*-PEO thin film……………………….……………………..55

Figure 4.2 AFM images of the PS-*b*-PEO template before and after heat treatment; a, after solvent annealing for 24hours at room temperature; b, after heating at a rate of 5 ^{o}C/min to 500 ^{o}C and holding for 2 hours. The (fast) Fourier transforms (FFTs) shown as inserts confirm the hexagonal order of the self-assembled gel thin film, a, and crystallized CFO cylinders, b. Section c displays the MFM phase image of the crystallized PZT/CFO nanocomposite……………………………………………...……..…..59

Figure 4.3 TEM results of self-assembled thin film nanostructures; a, Cross sectional TEM image of the PZT/CFO nanocomposite and, b, microbeam EDS elemental composition analysis as well as, c, results of microbeam characterization. The EDS spectrum of the bright columns indicates low Co and Fe content (4.3 at %), and the ratio between Lead (28.79 at %), Zirconium (12.38 at %) and Titanium (12.26 at %), is consistent with PZT. The EDS spectrum of the dark columns shows a 1:2.2 ratio of Cobalt (12.9 at %) to Iron (28.3 at %), which is consistent with CFO. The diffraction patterns were taken at the light and dark locations of the cross section, a, the diffraction rings indexed in red and blue correspond to the known lattice parameters and textures of CFO and PZT. ……………………….61

Figure 4.4Chemical composition analysis; a) microbeam EDS elemental composition analysis and, b) results of SAD characterization. The diffraction pattern was taken over a large area encompassing both the dark and light regions in the cross sectional image shown in Fig. 4.3a.......................................62

Figure 4.5 High Resolution Transmission Electron Microscopy (HRTEM) image of interface region; a, HRTEM image of the interface region marked in the cross section shown in Fig. 4.3a. The CFO(left)/PZT(right) interface is not epitaxial. The graph below, b, displays the results of the coordinate-matched Fe concentration profile indicating that interdiffusion occurred during the annealing process. Note the difference in scales of Figs 4.5b and 4.3a. If Fig. 4.5b would have been plotted on the scale of Fig. 4.3a the Fe composition profile would appear to be nearly rectangular. The fitting line merely serves to guide the eye..62

Figure 4.6 a, Schematic of an electroded sample. The electric field E_1 was applied through the electrodes marked "+" and "-." b, well-defined ferroelectric hysteresis of the annealed thin film; the saturation and remnant saturation polarization values, P_r and P_s, resulted from PUND measurements…….64

Figure 4.7 Ferromagnetic and ME characteristics of the hexagonal CFO cylinder array embedded in a PZT matrix magnetized parallel and perpendicularly to their axes, H_3 and H_1, with an applied magnetic, H_3 plus electric field, E_1. $\frac{\mu_i(H_3)}{\mu_i(H_3, E_1)} \approx 5$ ……………………………………….…..…...…66

Figure 4.8 AFM images of the PS-*b*-PEO template before and after of heat treatment at the PS-*b*-PEO ratio (PEO:PS =0.6); left, after solvent annealing for 24hours at room temperature; right, after heating at a rate of 5 °C/min to 500 °C and holding it for 2 hours. The FFTs shown as inserts confirm the 1D order of the CFO lamellae..70

Figure 4.9 TEM cross section of the 2D onion domain structure created by annealing a PS/PZT-b-PEO/CFO polymer for ≈ 0.2 Ms (64 hours) in a magnetic field of 0.8 T. The PZT and CFO precursors serve as contrasting agents.. 71

Figure 4.10 Initial growth kinetics of the 2D onion evolution in a PS/PZT-b-PEO/CFO polymer thin film in the presence of a magnetic field B. a, raw data; b, data normalized according to eq. (2): B_1= 0.05 T, B_2= 0.015 T, B_3= 0.8 T…………………………..…………………………...……..71

Figure 4.11 AFM phase images of the nanostructures created by room temperature annealing for times as long as ≈ 3840 min (64 hours) in magnetic fields as high as 0.8 T………………………..…...74

Figure 4.12 Fast Fourier transforms corresponding to the sequence of AFM images………………………………………………………………..……..75

Figure 5.1 Xray diffraction of BTO-CFO compound crystal……...…………..…. 79

Figure 5.2 Conventional SEM images of BTO-CFO compound crystal…..……....79

Figure 5.3 TEM images of nanostructure morphologies. (a) Low magnification image including a selected area electron diffraction pattern demonstrating the long coherence length of the periodic structure. (b) Conventional image; the dark and bright areas are CFO and BTO lamellae, respectively and the dark center line in the bright stripes is the image of a stacking fault. (c) [111] zone HRTEM images showing the atomic structure of each layer of the bicrystal. (d) Schematic diagram of the in-plane image corresponding to the common <111> zone axis. It shows the stacking fault in the BTO portion and the corrugated interface at which oxygen octahedra "belonging" to CFO and BTO overlap……………………......................81

Figure 5.4 Dielectric constant and loss factor of BTO-CFO compound crystal. (a-b) dielectric constant and loss factor versus temperature measured at various frequencies (from left to right: 21.5 Hz, 46.4 Hz, 100 Hz, 215 Hz, 464 Hz, 1000 Hz, 2150 Hz, 4640 Hz, 10 kHz). (c-d) dielectric constant and loss factor versus temperature subjected to an external magnetic field of 100 Oe. The inset of image d demonstrate linear variation of $10^{3}\cdot(T_m-T_{vf})$ as a function of ln(f) validating the Vogel-Fulcher relationship under different magnetic fields: 0 Oe, 100 Oe and 200 Oe. …………………...……......83

Figure 5.5 Lorentz TEM of BTO-CFO bicrystal…………………...……………….85

Figure 5.6 Magnetic and electric properties of BTO-CFO compound crystal. (a) magnetic hysteresis loop of BTO-CFO. The right-bottom inset shows the magnetoelectric α_{ME} -dependent variation of the external magnetic field (the bias AC field, 10 Oe). An example of the frequency dependent *M-E* coupling coefficient α= əE/əH is calculated from the M-E output voltage. (b) Polarization loop of the BTO-CFO compound crystal sample at room temperature..86

Figure 7.1 Applications of sol gel method according to S. Sakka ………………..……92

Figure 7.2 Sol-gel process to synthesize solid materials …………………..…..…94

Figure 7.3 Schematic drawing of spin coating process ……………………………..95

Figure 7.4 MFM maps the magnetic domains of the sample surface. ……………..…100

Figure 7.5 A, Schematic of electric measurement set-up; B, Pulse train for switching measurements …………………………...……………………………..…101

Figure 7.6 Schematic diagram of VSM …………………………….………...103

Figure 7.7 Schematic of a SQUID system ……………………………………...104

Figure 7.8 Experimental setup for ME_H effect ……………………………………105

Figure 7.9 Experimental setup for ME_E effect …………………..…………..……..105

Chapter 1

Introduction

1.1 Multifunctional Materials

Multifunctional materials combine multiple functions including electronic, magnetic, mechanical, photonic, optical, and biological functions. They are capable of exhibiting various controllable and predictable physical responses when subjected to diverse external conditions. They are expected to bring important breakthroughs in various technological fields. In this work, we study multifunctional composite materials and concentrate on those materials which couple three physical properties: magnetic, electric and mechanical properties, also termed magnetoelectrics or multiferroics.

Since the 1970s when the first magnetoelectric (ME) composite consisting of a piezoelectric phase and a ferromagnetic phase was reported, [1] a variety of ME composites have been fabricated. ME composites have drawn much attention since they show new classes of physical properties. These new classes of physical properties are characterized by a secondary coupling of individual physical properties of each component of a composite system. The concept of such "product property" is explained in the following section. To prepare ME nanocomposites, improved strategies are needed to provide very large interfacial areas and controlled connectivity between piezoelectric and magnetostrictive components. Solution-based approaches for the thin film deposition are particularly desirable and flexible. Therefore, the solution-based bottom up paradigm is a promising route toward nanoscale multifunctional materials' synthesis, a method that combines sol-gel chemistry with self-assembly and phase separation to produce ME thin film nanostructures or bi-crystals with a tailored morphology, see Fig 1.1. The bottom up nanotechnology builds upon synthesis of nanoscale objects and their assembly into functional architectures. This has already been successfully used in the preparation of photonic crystals,[2] three-dimensional superlattices of magnetic nanocrystals,[3] magnetic nanocomposites,[4] and ferroelectric nanostructures.[5]

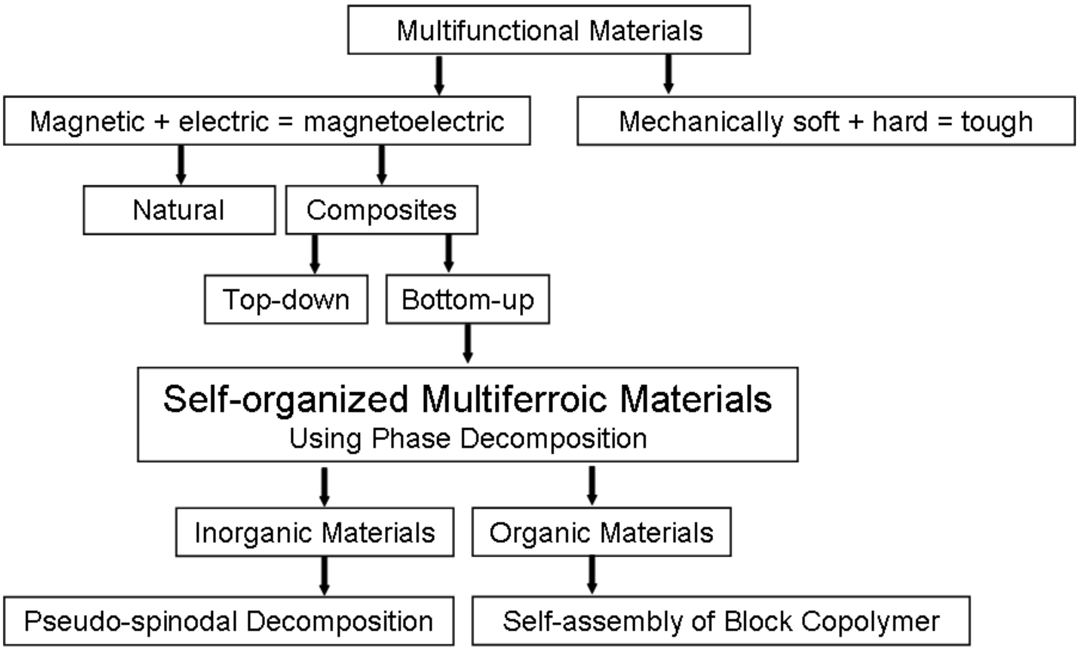

Figure 1.1 Roadmap of this thesis

1.2 Magnetoelectric Composite Materials

1.2.1 Background of Magnetoelectrics

Magnetoelectric materials (or Multiferroics) show simultaneous ferromagnetic and ferroelectric behaviors. Ferromagnetism is a phenomenon in which a material exhibits a spontaneous magnetization that can be switched by an externally applied magnetic field. A ferroelectric material exhibits a polarization even in the absence of an external electric field, and the direction of such spontaneous polarization can be reversed by an external electric field. Elasticity refers to a deformation in response to an applied stress. The simultaneous ferroelectricity and elasticity is known as piezoelectricity, which leads to the wide and well-established use of piezoelectric materials in transducer applications. Similarly, the coupling between ferromagnetism and elasticity leads to magnetostriction and the application of magnetomechanical actuators. Among these systems, magnetoelectrics are materials that are both ferromagnetic and ferroelectric, and more importantly, demonstrate a magnetoelectric coupling effect. As a result, they have an electric polarization variation as a response to an applied magnetic field, or an induced magnetization by an external electric field. This behavior could prove useful in spintronic applications, and could result in new types of transducers, actuators, and memory storage devices.

All of the magnetoelectric materials studied to date can be classified into two categories: single phase multiferroics which show ferroelectricity and ferromagnetism simultaneously in one phase and multiferroic composites which combine ferromagnetic and ferroelectric phases. The current trend is to extend the definition of multiferroic materials to include antiferroics whereas previously the definition was strictly defined to only include ferroics, see figure 1.2.[6]

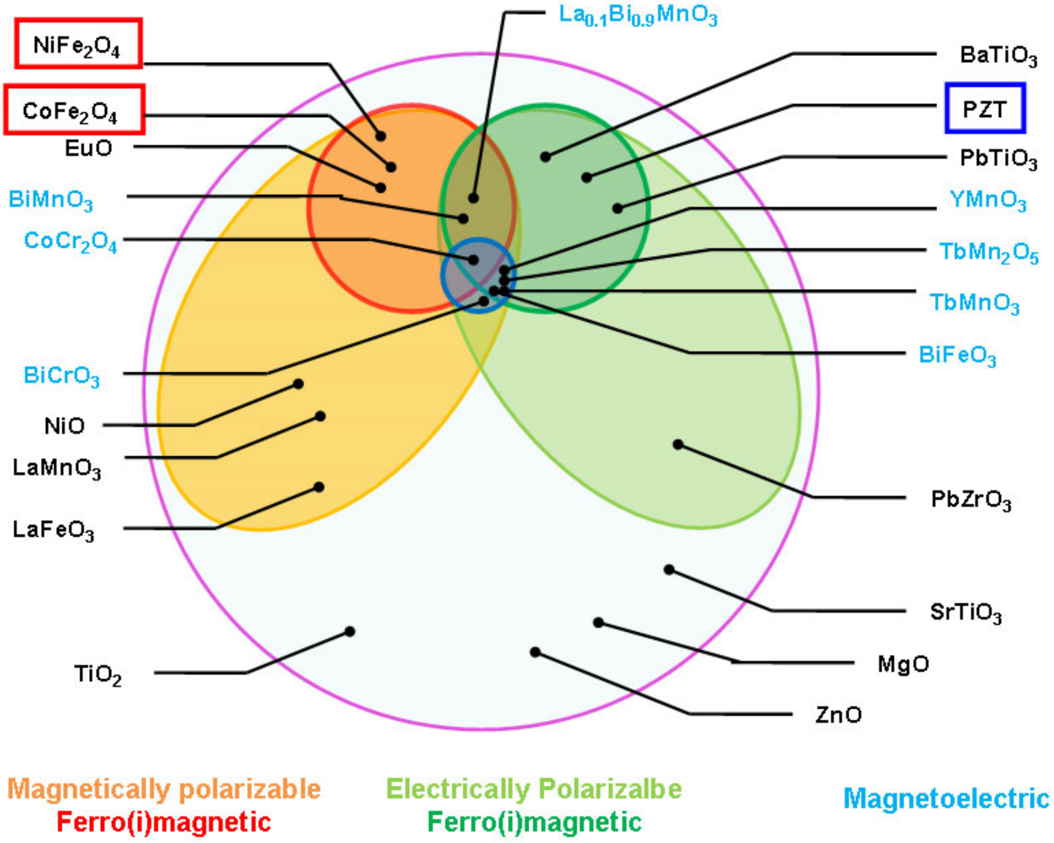

Figure 1.2. Multiferroic oxides. The largest circle indicates the insulating oxides: electrically polarizable materials (green ellipse) and magnetically polarizable materials (orange ellipse). Within the ellipse, the circle indicates materials with a finite polarization (ferroelectrics) and/or a finite magnetization (ferro- and ferrimagnets). According on the definition, multiferroics correspond to the intersection between the ellipses and the circles. The small circle in the middle represents systems exhibiting a magnetoelectric coupling.[6]

The most single-phase multiferroic materials is inapplicable due to their quite low Curie or Neel temperatures (Table I). They also demonstrate a very small ME coupling coefficient; the growth of crystals was usually a challenging task. Therefore, most applications discussed by Wood and Austin[7] were viewed as unpromising. The fundamental physics behind the lack of natural ME materials has been explored by Nicola A. Hill.[8] It was found that the d electrons in transition metals, which are essential for magnetism, reduce the tendency for off center ferroelectric distortion.

Consequently, an additional electronic or structural driving force is necessary for ferromagnetism and ferroelectricity to take place. There is a lack of research activities in single phase because of the general weakness of the ME effect, a shortage of compounds displaying it, the difficulties in developing useful applications, and a limited understanding of the microscopic sources of ME behavior. However, in this thesis, we will only focus on magnetoelectric nanocomposites consisting of piezoelectric and magnetostrictive components.

Table I Multiferroic single phase

REMn	FE T_C	$T_{\text{Néel}}$
$TbMnO_3$	27 K	41 K
$GdMnO_3$	23 K	43 K
$DyMnO_3$	18 K	39 K

Other	FE T_C	$T_{\text{Néel}}$
$BiFeO_3$	1083 K	653 K *
$BiMnO_3$	750 K	FM T_C=105 K
$YMnO_3$	900 K	70 K **

1.2.2 Magnetoelectric Composite Materials

The physical properties of composites, a material that is constituted from two or more single phases, are controlled by the properties of the components as well as by the interaction between them. Product properties refer to the effects which exist in the composite, but are not found in its end compounds. Product properties represent an effect in one of the phases which in turn leads to a second effect in the other phase.

The concept of "product property", an ME coupling effect in a composite material consisting of ferromagnetic and ferroelectrics through a strong mechanical coupling between two phases, was first proposed by van Suchtelen.[9] For ME product property:

$$\text{ME effect} = \frac{\text{electrical}}{\text{mechanical}} \times \frac{\text{mechanical}}{\text{magnetic}} \tag{1.1}$$

The coupling between the two order parameters is through a stress mediation, i.e., a magnetic field induces a stress of the magnetostrictive phase, which in turn distorts the piezoelectric phase in which an electric polarization is generated. The composite can be considered a new material with multiferroic properties. The ME effect is extrinsic in this case since it is not demonstrated by any of the constituent phases on their own.

The idea of synthesizing a composite displaying an ME effect was first proposed by Tellegen in 1948.[10] Actually, van Suchtelen, van den Boomgard *et al* grew the first artificial ME material by combining ferroelectric $BaTiO_3$ and piezomagnetic $CoFe_2O_4$ in an eutectic composite using unidirectional solidification method.[11,12,13] Depending on the growth conditions the composition used by van Suchtelen, van den Boomgard *et al* revealed ME voltage coefficients of up to $130 mVcm^{-1}\ Oe^{-1}$. Thus, even in the earliest experiments on ME composites the ME response exceeds the largest values observed on single-phase compounds by more than an order of magnitude.[14]

Subsequent to the pioneering experiment on $BaTiO_3/CoFe_2O_4$, a variety of titanate/ferrite compositions were investigated.[15,16,17,18,19,20,21,22,23] A material that combines a large piezoelectric constant and commercial availability is $PbZr_{1-x}Ti_xO_3$ (PZT) with $d_{33} \sim 250\ pmV^{-1}$, whereas, besides ferrites, $Tb_{1-x}Dy_xFe_2$ alloys (Terfenol-D) also display superior magnetostrictive behavior[24]. Therefore PZT/ferrite and PZT/Terfenol-D represent the most frequently studied composites thus far[25,26,27,28,29,30,31,32,33,34,35,36,37] although materials with higher piezoelectric coefficients do exist[38, 39]. Further, experiments on many doped titanate/ferrite composites like $Ba_{0.8}Pb_{0.2}TiO_3/CuFe_{1.8}Cr_{0.2}O_4$[40] were reported. Other piezoelectric constituents include $Bi_4Ti_3O_{12}$, polyvinylidene-fluoride (PVDF),[41] $PbMg_{1/3}V_{2/3}O$[42] and $PbX_{1/3}Nb_{2/3}O_3$-$PbTiO_3$ (X = Mg, Zn).[43] As alternative magnetostrictive ingredient manganites,[44] $LiFe_5O_8$, YIG[45] and Permendur[46] have been chosen. Various constituents have been reported as multiferroic composite materials. Table II lists several multiferrioc composite materials with their preparation methods that have been reported in the literature.

Table II Multiferroic composite systems

Morphology	Materials	Coupling (mV/Oe cm)
Composite	Terfenol-D&PZT in Polymer	42[26]
Composite	$BaTiO_3$ & $CoFe_2O_4$	130[11]
Laminate	$NiFe_2O_4$/PZT	1400[47]
Laminate	Terfenol-D/PZT	4800[20]
Laminate	Metglas/PVDF	7200[28]
Laminate	Metglas/PZT Fiber	22000[30]

Most of the present activities are devoted to ME effects in composite materials. Originally, sintered granular composites were used for producing composite ME effects. Subsequently it was discovered that the ME coupling can be greatly improved by using laminated double-, triple or multilayer composites in which the constituents are connected by glue, by epoxy or, most efficiently, by hot pressing. The ME response of the laminated composites is determined by four major aspects: (i) the magnetic, electrical and mechanical coefficients of the constituents; (ii) the thickness and number of the piezoelectric and magnetostrictive layers; (iii) the type of bonding between the constituents; (iv) the orientation of both constituents and applied electric or magnetic fields. With the laminated bulk PZT/Terfenol-D composite sample, Ryu[30] *et al* immediately acquired a ME voltage coefficient of up to 4.68Vcm^{-1} Oe^{-1}, which exceeded the highest value gained from any particulate composite at that time by a factor of 36. The highest values of ME coefficients, V_{ME}=22 V/cm Oe, are found in "1-2" composites that consist of PZT piezofiber layers laminated between two high-permeability magnetostrictive FeBSiC alloy.[47]

In spite of the potential of multiferroics for giant ME effects and ME phase control, the ME effect in ME composite bulk sample is much farther from practical applications. An important step for increasing the flexibility and the number of degrees of freedom in tuning the ME properties of multiferroics is the growth of thin multiferroic films. Some ideas for achieving this goal included new degrees of freedom in designing ME compounds, new experimental techniques and novel theoretical concepts for understanding ME behavior.

1.3 Magnetoelectric Nanocomposite Thin Film

Recently, attentions to ME materials have been gradually drawn toward nanocomposite thin films. Compared to bulk composites, ME composite thin films exhibit unique advantages. Their composition and connectivity can be modulated at the nanoscopic scale, and artificial thin film heterostructures can thus be achieved. These materials have potential applications in many devices and integrated units such as sensors, MEMS devices, and high density information storage devices.

In a film-on-substrate geometry, such nanocomposites can be created in three extreme forms: (i) "vertically aligned structure" (ii) "multilayer geometry" and (iii) “particulate nanostructure”. An interesting ME nano-composite thin film has 1-3 vertical ME nanostructures. Such structures were grown by Zheng *et al.* [48] They consist of $CoFe_2O_4$ nanopillars which are grown perpendicular to the $SrTiO_3$ substrate and which are embedded in a $BaTiO_3$ matrix. Such self-assembled “1-3” morphology heterostructure minimized constraint effect from the substrate, and generated a large interface between the ferroelectric and ferromagnetic phases. While it could be demonstrated that this composite had ME character, the determination of ME susceptibilities proved difficult. Several reasons for this discrepancy were identified, such as low resistivity of the magnetostrictive phase or eddy currents induced in the conducting phase by the applied ac voltage. If the resistivity is low, electric poling becomes difficult and the ME properties are reduced because of leakage currents.

In comparison with the vertical nanostructures, the 2-2 type horizontal heterostructures exhibit weak ME effects due to large in-plane constraint from substrates[49]. But the horizontal nanostructures are much easier to be fabricated. Moreover, they rule out the leakage problem due to their ferroelectric layers, which could lead to a visible ME effect. Murugavel *et al.*[50] and Singh *et al.*[51] reported $BaTiO_3$–$Pr_{0.7}Ca_{0.3}MnO_3$ perovskite superlattices grown on $SrTiO_3$ via PLD technique. Different 2-2–type combinations of ferroelectric perovskites (e.g., BTO, PZT) and magnetic oxides (e.g., $CoFe_2O_4$, $NiFe_2O_4$, and $La_{1.2}Sr_{1.8}Mn_2O_7$) have also been grown via PLD and spin-coating method.[52, 53] These layered films showed good coexistence of ferroelectric and ferromagnetic behaviors. However, the coupling effect in a multilayer structure will be negligible due to the clamping effect of the substrate, since the magnetoelectric coupling is purely through elastic interactions.

Few works was reported on the 0-3–type nanostructure.[54] Wan *et al.* [55]prepared a PZT-CFO composite thin film using a sol-gel process and spin-coating technique. The phase separation of the CFO and PZT phases in the films was verified by x-ray diffraction. The ferrimagnetic particulate CFO nanoparticles were embedded into PZT matrix after sintering. The films exhibited both good magnetic and ferroelectric properties, and the ME effect of these films was found to be strongly dependent on the magnetic bias and magnetic field frequency. Delicate designing and control of the two-phase coexisted microstructures are crucial to an effective ME output.

1.4 Motivation of this Thesis

Apparently, the ME coupling effect in composite thin films is a powerful addition to the class of ME coupling phenomena. Many new parameters can be tuned in order to optimize the ME response, such as the stoichiometry and nanostructure of the composite. In composite samples, the geometrical degrees of freedom determine the ME response more than in the case of single-phase compounds. The relative orientation of the constituents to each other is important. Moreover, composites of piezoelectric and magnetostrictive phases can be electromagnetically coupled via stress mediation between their interfaces. To obtain the highest ME coupling efficiency, we need to obtain large interface areas.

Recent studies have shown that different morphologies of epitaxial nanocomposite films could play a crucial role in obtaining maximum ME coupling. In a study of the magnetoelectric coupling effect in ferroelectric and magnetic nanocomposite thin films, a phase field simulation[56] was developed for the effects of the film thickness, morphology of the nanocomposite, and substrate constraint, shown in Fig. 1.3. The vertical stripelike and 1-3 type pillar morphologies could enhance the effect of ME coupling effect,[57] as shown in Fig. 1.3. Benefiting from the simulations, we have investigated different morphologies of magnetoelectric composite thin films through self assembly "bottom-up" techniques to explore their ME coupling effect. We focused primarily on self-assembled multiferroic nanostructures in order to reveal how naturally-ordered morphologies alter the fundamental physics of magnetoelectric coupling processes in the nanometer regime.

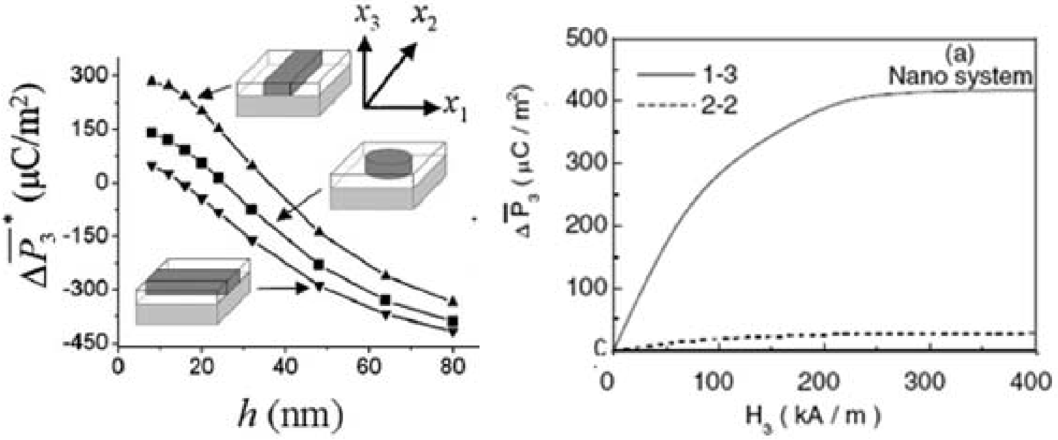

Figure 1.3: Dependence of magnetic-field-induced electric polarization $P_3=P_3(H_e// x_3)-P_3(He//x_1)$ on the film thickness h.[56]

Decomposition into phases with different functionalities but similar crystal structures has been observed in "3-1" and "2-2" magnetoelectrics, be it in bulk[58] or thin film materials.[59, 60, 61, 62] This thesis will describe studies of various self-assembled multiferroic nanocomposite thin film morphologies in pursuit of two goals (shown in Fig. 1.4):

- to exploit "1-1" mode of vertical multilamellar nanostructure and,
- to exploit "1-3"mode of hexagonally ordered nano-magnetoelectrics.

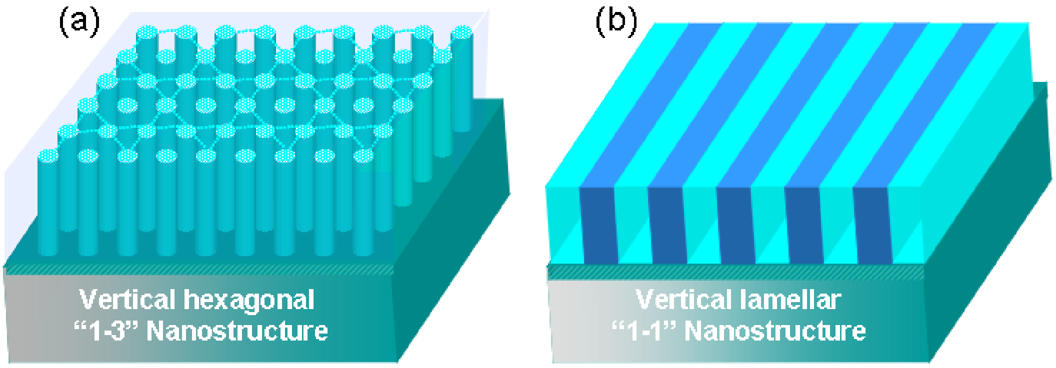

Figure 1.4, Schematic illustration of a hexagonally ordered "3-1" composite structure on a substrate (a) and nano'1-1' composite structure on a substrate (b).

1.5 Contents of this Thesis

The motivation of this work is to fabricate and analyze self-assembled vertical magnetoelectric nanostructures. The aims of this thesis are to investigate the structure and multiferroic interactions in composite systems and how these affect their physical properties, to understand the mechanisms at work in nanoscale structures such as thin films and how these affect bulk properties, and to contrast different structure morphologies of nanocomposites by a bottom up self-assembly paradigm.

Chapter 2 summarizes the materials and solution processing methods used in this work, including a brief background of spinodal decomposition, self-assembly of block copolymer and eutectic reaction in multiferroic complex oxide synthesis. Chapter 3 covers the growth and analysis of vertical lamellar ordered magnetoelectric nanostructure through pseudo-spinodal decomposition of the gel state. In chapter 4 we present the work on combining self-assembly of block copolymer with multiferroic sol-gel precursor to fabricate hexagonal "1-3" cylinder morphology and vertical multilamellar and oniontype ring magnetoelectric nanostructures. Chapter 5 describes a new phase separated nanolamellar $BaTiO_3$-$CoFe_2O_4$ magnetoelectric bi-crystal and its unique physical properties. Finally, chapter 6 gives a general conclusion and a proposed future exploration.

Chapter 2

Solution Processing of Multiferroic Nanostructures

At the turn of twenty-first century, we entered the nanoworld. A driving force of this nanorevolution is a continuous progress in microelectronics towards both increasing the integrated circuits' integration level and reducing their size of active elements. This is well illustrated by Moore's Law in figure 2.1. As one can see, the critical line of one micron was crossed in the 1990s, when we entered the nanoelectronics era at that time. Electron beam lithography had started to overtake the conventional UV photolithography, which cannot provide submicron resolution. What is next? Can we further shrink the size of existing electron devices? The answer is *no*, because of obvious physical limitations of top-down and low through put rates.

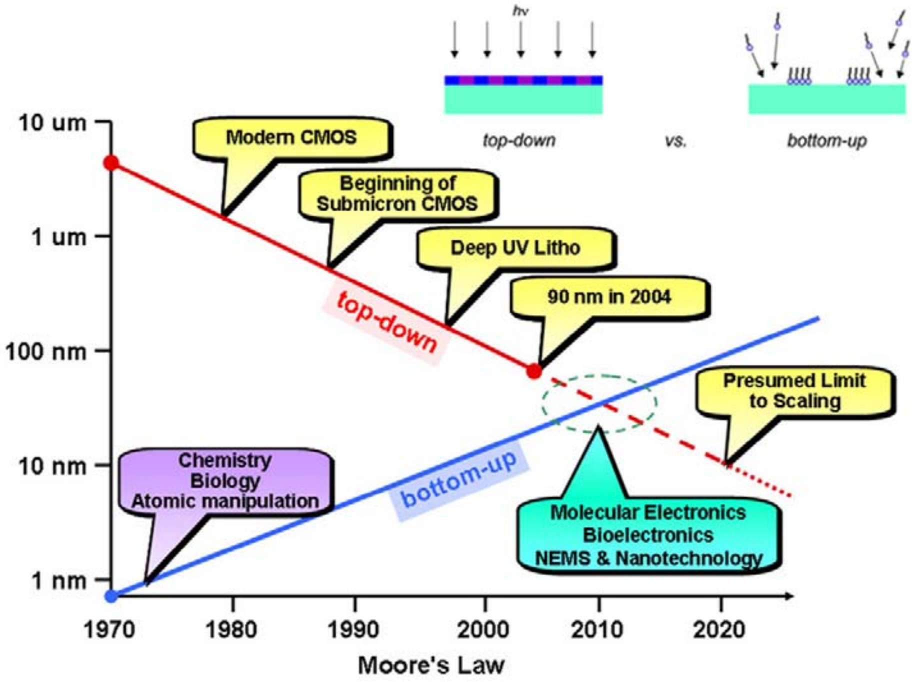

Figure 2.1 Two approaches to control matter at the nanoscale[63]

To date, the majority of solution-processing research has focused on soft materials and polymeric organic films. In contrast, this study addresses the solution-processed inorganic multiferroics, and covers from sol-gel processing and chemical solution deposition to the cutting-edge use of self assembly. The resulting multiferroic architectures are inherited from the self assembly and phase separation. These multiferroic inorganic two-phase components offer the potential for better performance and more robust thermal and mechanical stability than comparable organic-based systems.

In particular, this technique is compatible with high-throughput, low-cost, and low-temperature deposition processes such as spin coating, dip coating, printing, and stamping. Throughout the thesis, illustrations and examples of applications are provided to help fully appreciate the concepts and opportunities involved in this field.

2.1 **Bottom-Up versus Top-Down**

The two basic approaches to creating surface patterns and devices on substrates in a controlled and repeatable manner are the ‘top-down’ and ‘bottom-up’ techniques. Top-down methods essentially ‘impose’ a structure or pattern on the substrate being processed. For top-down fabrication, methods such as lithography, writing or stamping are used to define the desired features. In contrast, bottom-up methods are aimed to guide the assembly of atomic and molecular constituents into organized structures. The technique of self-assembly is one of the few practical strategies available to arrive at ensembles of nanostructures. The self assembly bottom-up process, defined as the autonomous organization of components into structurally well-defined aggregates, is characterized by numerous beneficial attributes; it is cost-effective, versatile, and facile; it occurs towards the system's thermodynamic minima, resulting in stable and robust structures[64] and atomic feature sizes.[65]

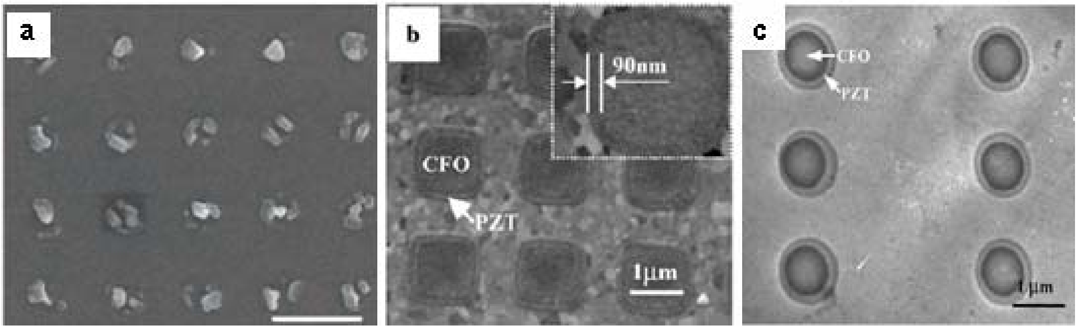

Figure 2.2 The multiferroic composite nanostructures prepared by "top-down" approach[66]

In addition, there is an intense interest in self-assembly of nanostructured materials. Besides the inherent interest of the physical processes involved, self-assembly holds promise for technological applications. Recent years have witnessed increasing success in the controlled self-assembly of quantum dots, quantum wires, and superlattices.[67] Traditional approaches tend to be based on physical methods, such as patterning. For instance, the top-down multiferroics were prepared by lithography process and physical thin film depositions, such as Pulsed Lased Deposition (PLD), Sputtering, or Molecular Beam Epitaxy (MBE). The physical properties obtained from "top-down" approach are weaker than the naturally ordered multiferroic thin films (Fig. 2.2). Moreover, it should be possible to develop a chemistry of organized matter based on higher-order architectures with enhanced properties. This has stimulated great interests in further development of chemical methods as cost-effective alternatives to such physical methods.

In this dissertation, I will outline how chemically self-organized growth and self-assembly serve as an efficient tool for the bottom-up fabrication of multiferroic structures and patterns on the nanometer scale. I will highlight how the interplay between block copolymer and sol-gel chemistry leads to nanoscale self-assembly and cooperative transformation and reorganization of hybrid inorganic–organic building blocks to produce emergent magnetoelectric oxide nanostructures with complex form and hierarchy. I will particularly focus on informative illustrations of how this approach might lead to useful nanometer scale functional structures.

2.2 Spinodal Decomposition

We consider spinodal decomposition a mechanism for structure formation. Spinodal decomposition in an alloy *AB* is the common tendency to phase separate into *A*-rich and *B*-rich phases. Similar mechanism occurred in diblock copolymer systems (see the following section). To obtain "1-1" and "1-3" self-assembled magnetoelectric nanocomposite, we use spinodal decomposition as bottom-up principle.

The theory of spinodal decomposition was first provided by John Cahn.[68, 69, 70, 71] The concept has led to advances in all subfields of materials science and engineering.

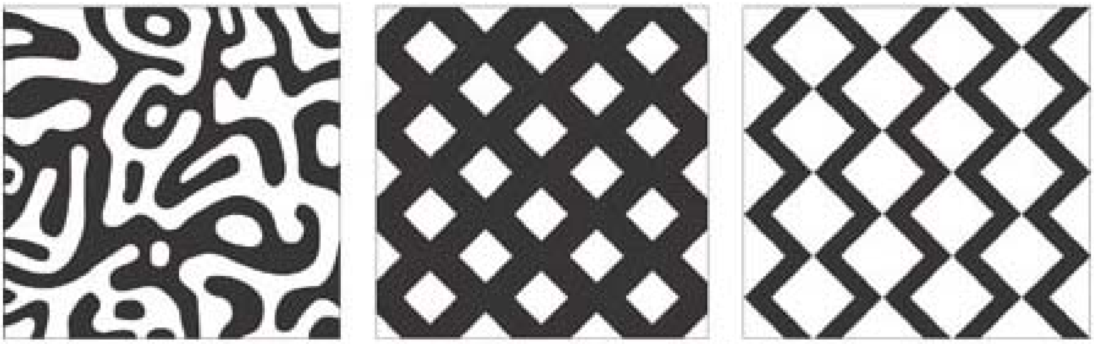

Figure 2.3**:** Typical spinodal decomposition showing well-defined periodicities and separated phases.[72]

The theory of Spinodal Decomposition (SD) in alloys has been known for quite a long time.[73, 74, 75, 76, 77, 78] It has been known that infinitesimal compositional fluctuations over large volumes can become thermodynamically unstable, decompose a solid solution spontaneously and eventually transform into well defined periodic phases of the solute and solvent. Some examples of such microstructures are shown in Figure 2.3. A thermodynamic modification to the Ficks 2nd law of diffusion approximates the energy associated with chemical potential gradients,

$$\frac{\partial c_B}{\partial t} = D\nabla^2 c_B - 2K\nabla^4 c_B \qquad (2.1)$$

where c_B = mole fraction of solute B in solvent A, D = Diffusivity, K = Gradient Energy Coefficient. It can be shown that a small sinusoidal change in composition, $c_B - co = A^* \cos\beta x$, where c_o is the equilibrium concentration, A the amplitude and β the wavelength of the fluctuation, will grow fastest at a critical wave number β_{crit} if

$$\left.\frac{\partial^2 f^{\hom}}{\partial {c_B}^2}\right|_T = 2K{\beta_{crit}}^2 \qquad (2.2)$$

where $f^{\hom}$ = free energy change of a homogenous material not subject to sinusoidal fluctuation. Equation 2.2 thus suggests that the minimum critical wavelength of modulation of the microstructure is given by

$$\frac{2\pi}{\beta_{crit}} = \left[- \frac{8\pi^2 K}{\partial^2 f^{\text{hom}} \Big/ \partial c_B^{\,2}} \right]^{1/2} \tag{2.3}$$

A graphical representation of this approach can be realized by plotting the inflection points in the free energy vs. composition diagram (i.e., $\partial f^{\text{hom}}/\partial c_B = 0$) onto a phase diagram. The resulting line is known as the ‘spinodal line’. The area below ‘spinodal line’ is termed as the ‘spinodal region’, in which SD is most likely to occur. Outside the spinodal region, the classical homogenous nucleation region exists which requires activation energies to get them started. This is shown in Figure 2.4.[79]

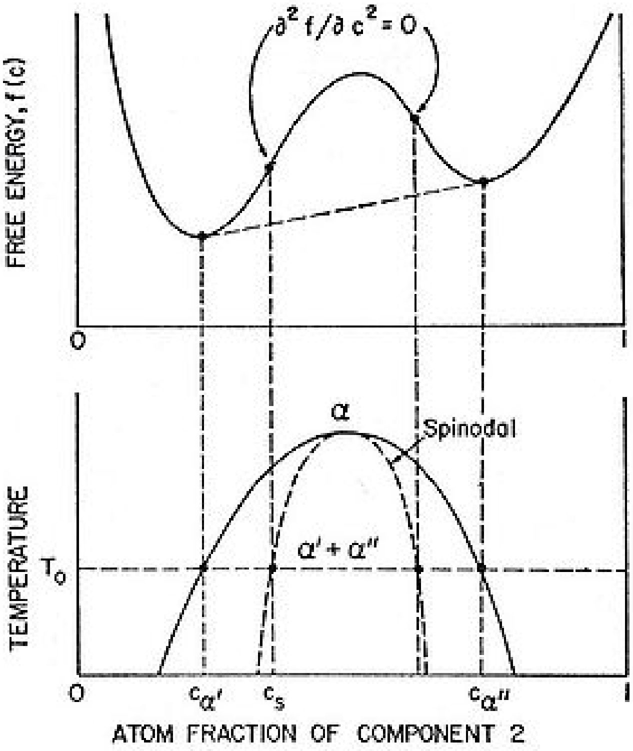

Figure 2.4: Spinodal decomposition of binary alloy with miscibility gap

Magnetic Field Effect during Spinodal Decomposition

It has been shown that an external magnetic field applied during the annealing process could provide further control over the SD microstructure if new formed phases are ferromagnetic.[68] Cahn observed that positive $\int dV\vec{H}.\delta\vec{M}$ magnetostatic energy existed most strongly along waves propagating parallel to the direction of M. In waves traveling perpendicular to M, there were no such energy terms. Thus compositional fluctuations which traveled parallel to M were most likely to be suppressed. This is shown in the microstructures of Fig. 2.5.[80]

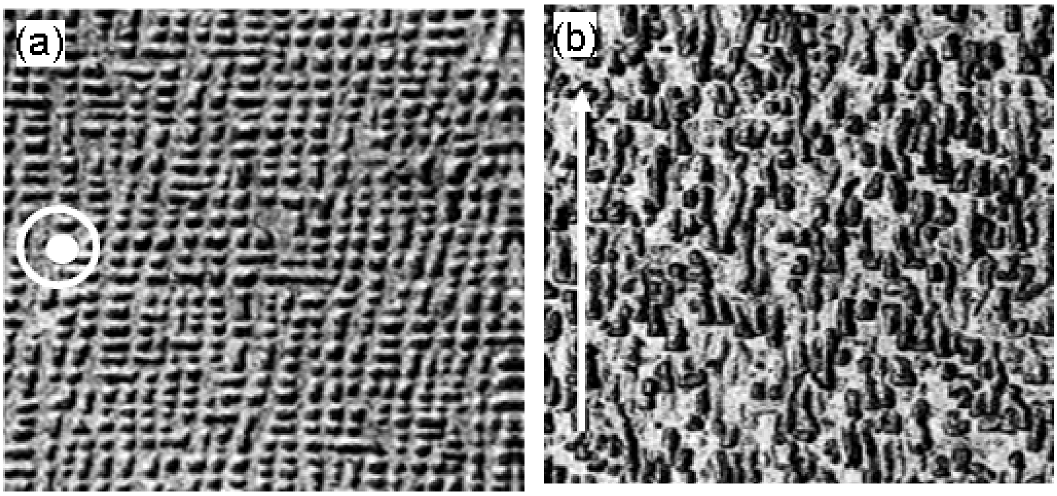

Figure 2.5: Electron graphs of Ticonal alloy. a). The left image shows microstructure for applied magnetic field along perpendicular direction. b). The right image shows microstructure for magnetic field parallel to plane.[80]

Since the development of SD theories, there have been extensive applications in building alloys with unique microstructures and properties. [81, 82] Lately, the field of nanotechnology has started to use SD as a simple but effective way to build nanostructures.[83] For example, interesting magnetic properties are developed when a ferromagnetic phase spinodally decomposes into nanospheres in a non-ferromagnetic matrix.[84] It has been observed in decomposing the oxide ceramics $ZnMnGaO_4$,[85]

$Mg(Mn_xFe_{1-x})O_4$,[86] Mn-doped $CoFe_2O_4$,[87]$(Nd_{2/3-x}Li_{3x})TiO_3$,[88] which are materials of different physical natures (Fig. 2.6). In chapter 3, we will talk about how to use pseudo-spinodal decomposition to assemble a multiferroic PZT-$NiFe_2O_4$ nanocomposite system.

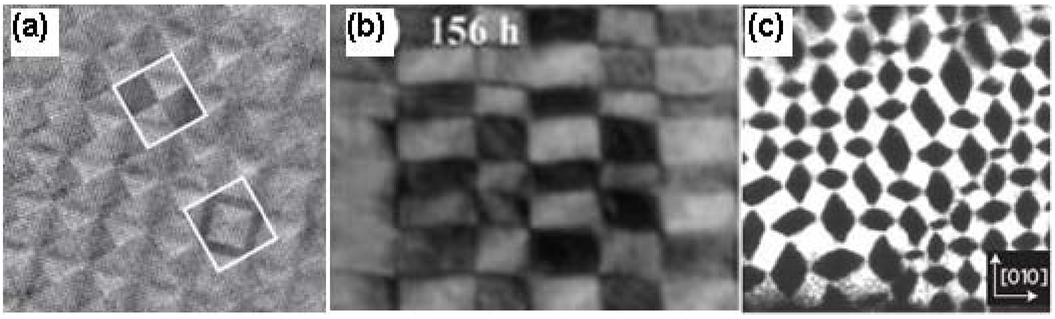

Figure 2.6 Architecture of 3D chessboard nanostructures; (a), chessboard of $(Nd_{2/3-x}Li_{3x})TiO_3$,[127] (b), $ZnMnGaO_4$[124], and (c), $Co_{39.5}$–$Pt_{60.5}$ alloy.[101] The scale bar is 10 nm.

2.3 <u>Self-Assembly of Block Copolymer</u>

Diblock copolymers are obtained by linking together two chemically distinct polymers, hydrophilic A and hydrophobic B. Bringing different polymers together introduces new interactions in the system. To deal with these interactions, polymer scientists widely use the Flory-Huggins interaction parameter χ_{AB} in the case of A and B polymers, defined by

$$\chi_{AB} = \frac{z}{k_B T}(\varepsilon_{AB} - \frac{\varepsilon_{AA} + \varepsilon_{BB}}{2}) \qquad (2.5)$$

where z is the number of nearest neighbor monomers, T denotes the temperature, K_B is the Boltzmann constant and ε_{AA}, ε_{BB} and $\varepsilon_{AB,}$ are the energies of the A-A, B-B and A-B interactions respectively. Since the thermal translational energy per macromolecule is of the order of k_BT, whereas the interaction energy per macromolecule is proportional to its length, the product $N\chi_{AB}$ rather than χ_{AB} is the relevant quantity. Due to the generally unfavorable interactions, chemically different polymers naturally tend to separate from each other. This separation occurs on a nanoscopic scale. In diblock copolymers, where chemically different polymers are covalently joint together, such a separation can only take place on a nanoscopic level. Here, the phase separation results in the spontaneous formation of a number of different well-ordered nanostructures, depending on the block copolymer composition and temperature. This property is widely used in nanotechnology. The equilibrium structure of the ordered state is determined by the minimum free energy, which consists of an interfacial free energy contribution and an elastic stretching contribution. The system can lower the interfacial contribution by reducing the interface area, which in turn increases the stretching free energy. When these two competing effects are balanced, the equilibrium structure is formed.

The phase behavior of a *diblock copolymer melt* as calculated by Matsen and Schick[89] in 1994 is presented in Figure 2.7. The lamellar (1), hexagonal (cylindrical) (*p6mm*), cubic (spherical) (*mmI*3) and gyroid (*daI*3) morphologies were found to be stable. The corresponding microstructures are schematically illustrated in Figure 2.7. We see that the diblock copolymer composition and the product $N\chi$ determine the stability regions in different morphologies. These morphologies are ideal to create and study multifunctional materials.

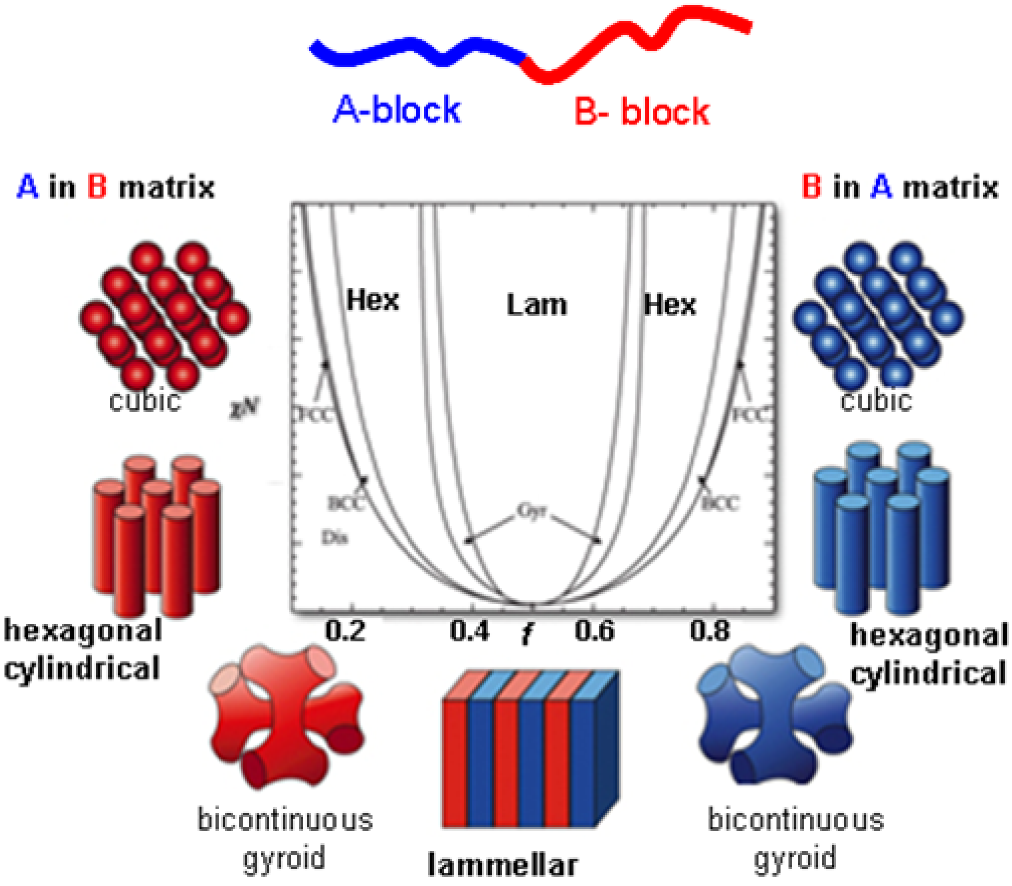

Figure 2.7. Phase diagram of diblock copolymer melt and schematic representation of a symmetric AB diblock copolymer. L denotes the lamellar morphology, H - hexagonal, G - gyroid, C- spherical morphology, D – disordered state.[128]

In chapter 4, we will talk about how to use self-assembly of diblock copolymer with multiferroic precursors to assemble multiferroic PZT-$CoFe_2O_4$ nanocomposite system.

2.4 Eutectic Reaction

In the past decades, considerable attention has been attracted in using directionally solidified eutectics for electronic devices. A eutectic is a mixture at such proportions that the melting point is a local temperature minimum, which means that all the constituents crystallize simultaneously at this temperature from molten solution. Such a simultaneous crystallization of a eutectic mixture is known as a eutectic reaction. The directional solidification of eutectics is a method used to produce an anisotropic composite directly from the melt. With such method, many attempts have been made to produce composite materials having designed physical properties. Solid products of a eutectic reaction can often be identified by their lamellar structures.

The $BaTiO_3$-$CoFe_2O_4$ eutectic system is interesting because it contains materials with large electric striction and magnetostriction. The magnetoeletric application of this system can be achieved by combining magnetic and electric properties through strain. Van den Boomgaard *et al*. have investigated the directional solidification of this system and shown that it is possibly applicable for new ME devices.[12] The growth morphology of this system is a plate structure, i.e., a structure with lamellae. The optical photographs of the directionally solidified $BaTiO_3$-$CoFe_2O_4$ eutectics show micron-scale spacing, see Fig. 2.8. The interface in the directionally solidified $BaTiO_3$-$CoFe_2O_4$ eutectic was bonded, but the electrical resistivity of the eutectic was too small to apply to a device due to the dissolution of a small amount of solute. If the eutectic system is to be applied to devices, it will be necessary to select properties which are non-sensitive to a small amount of solute, because any materials, even eutectic components, are dissolved solute.

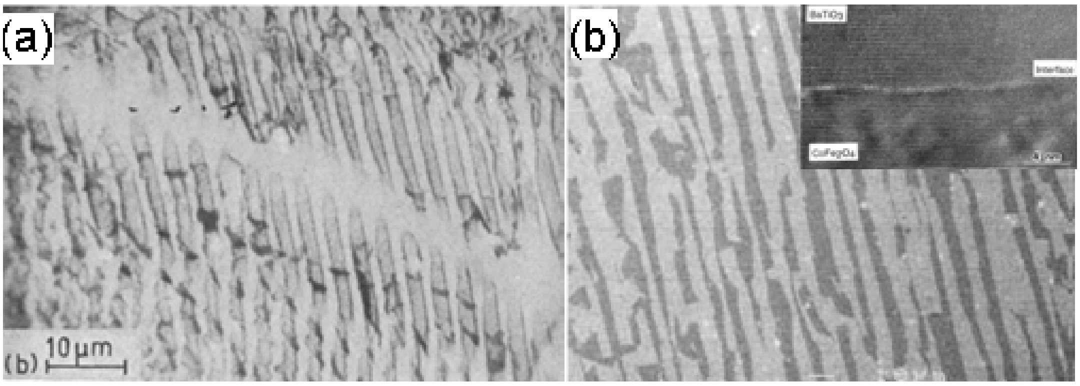

Figure 2.8 The eutectic magnetoelectric BTO-CFO composite microstructures[12]

In chapter 5, we investigate a modified solid state sintering method based on pseudo-spinodal decomposition of the Ba-Ti-Co-Fe-O quinary system. We will show how the phases spontaneously separate into nanolamellar $BaTiO_3$-$CoFe_2O_4$ superlattices with a sharp interface, which is related to a modified eutectic reaction.

2.5 Material Component of the Thesis

Ferroelectric component Lead-zirconate-titanate (PZT) is a typical ferroelectric ceramic with large piezoelectric coefficient, which is useful for piezoelectric devices. Ferromagnetic $NiFe_2O_4$ (NFO) and ferrimagnetic $CoFe_2O_4$ (CFO) components are used as magnetostrictive phase in this study. Table III presents the relative lattice differences of the perovskite/spinel nanocomposite systems, which provide the guidance for spinodally decomposed gel systems. We calculated the relative difference of the lattice parameter a, and the strain $\Delta a/a$, of some highly magnetostrictive ferrites with respect to different ferroelectric perovskites. According to the table III, NFO and PZT have the smallest lattice difference; therefore, we used them to study spinodally decomposed gel system. It is natural to start with the investigation of PZT/CFO nanocomposites in self-assembly block copolymer templating system. Because the magnetostriction of CFO is significantly larger than that determined for PZT/NFO. Since CFO is thermodynamically stable, the decomposition during sintering can also be expected to occur in air.

Table III Relative difference of the lattice parameter a, i.e. the strain Δa/a, of some highly magnetostrictive ferrites (FM) with respect to different ferroelectric perovskites (FE).

$\left\|\frac{\Delta a}{a}\right\| \approx \frac{2}{3}\left\|\frac{a_{FE}^3 - \frac{1}{8}a_{FM}^3}{a_{FE}^3 + \frac{1}{8}a_{FM}^3}\right\|$ [%]		Ferromagnetic Materials					
		$NiFe_2O_4$ a=8.33Å [90]	**$CoFe_2O_4$** a=8.39Å [48]	**$MnFe_2O_4$** a=8.5 Å [40]	**$CuFe_2O_4$** a=8.64Å [40]	**$ZnFe_2O_4$** a=8.43Å [91]	**Fe_2TiO_4** a=8.52Å [92]
Ferroelectric Materials	**PZT** A=4.084Å [93]	5.89	8.04	11.9	16.8	9.46	12.6
	$BaTiO_3$ a=4.028Å [94]	10.8	12.2	16.1	20.1	13.6	16.7
	$PbTiO_3$ a=3.98 Å [95]	13.6	15.7	19.6	24.5	17.2	20.2

The block copolymer, called polystyrene-b-polyethylene oxide (PS-b-PEO), is made up of polystyrene (PS), an amorphous polymer with a glass transition temperature of 100 degrees celsius, and polyethylene oxide (PEO), a crystalline polymer with an equilibrium melting temperature of 69 degrees celsius. Two different molecular weight poly(styrene)-b-poly(ethylene oxide) (PS-b-PEO) block copolymers are used with cylindrical and lamellar morphologies. Commercial polystyrene-*block*-poly(ethylene oxide) (PS-*b*-PEO) (molecular weight 40 000 g mol^{-1} and 9 000 g mol^{-1}; polydispersity 1.09) with a PEO volume fraction of 0.35 (Polymer Sources Inc.)

was used to generate a magnetoelectric nanostructure by heat treatment. The addition of multiferroic sol–gel precursors into both block copolymer self assembled molecular templates has allowed us to achieve variations in the phase morphologies (see Figure 2.9), as demonstrated by atomic force microscopy (AFM).

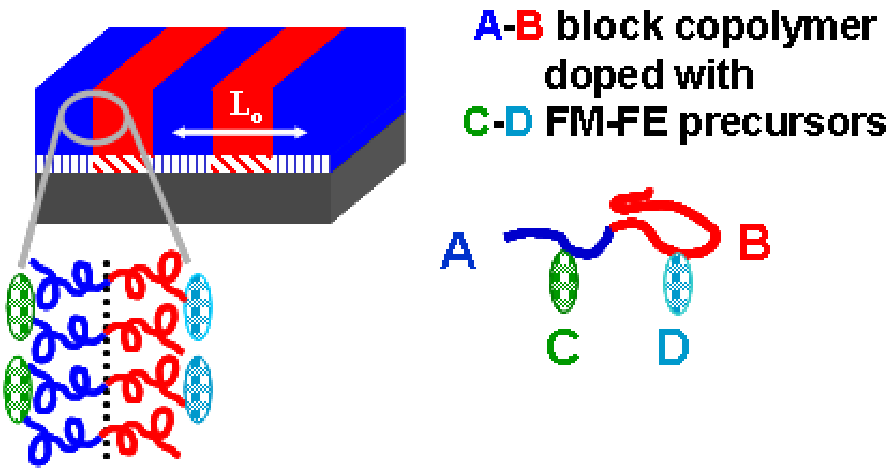

Figure 2.9. Schematic diagram of 50/50 ratio PS-b-PEO block copolymer system combined with ferromagnetic-ferroelectric $CoFe_2O_4$-PZT sol-gel precursors

Chapter 3
Pseudo-spinodally Decomposed Multiferroic Nanostructures

3.1 Introduction

Spinodal Decomposition (SD) is a fascinating phenomenon involving a spontaneous phase transformation of a homogeneous solid solution into 2 phases with regular periodicity in its microstructure. J.W. Cahn[68] proposed the thermodynamic theory showing conditions under which SD is possible and can propagate e.g. SD is hindered when elastic stresses are present between separating phases and in magnetic materials, SD can lead to microstructures oriented along an applied magnetic field direction applied during annealing.

Examples of studies relevant to this chapter, i.e. on decomposition in a magnetic field or of oxides are studies on Ticonal[96] and $CoFe_2O_4$-Co_3O_4, Al_2O_3-Cr_2O_3 and Al_2O_3-Cr_2O_3-Fe_2O_3.[97,98] There are also more recent theoretical phenomenological[99] and computational [100, 101] papers. And, experimental studies on spinodal decomposition in a magnetic field continue to this day with some recent examples having to do with Fe-Cr-Co alloys,[102] anisotropic giant magnetoresistance,[103] nanolamellar structures in Co-based alloys[104] and cobalt alloys in cermets,[105] among many others.

Spinodal decomposition will modify materials,[106] e.g. harden Al-Zn alloys, create new materials processing routes[107] or create better functional materials. In all cases pertaining to crystalline materials a, overwhelmingly cubic, parent phase is spinodally decomposed into two phases of the same symmetry and of the same functionality, e.g. mechanical or magnetic. Of course, decomposition into phases with different individual functionality is possible, but the known examples all relate to the spinodal decomposition to enable, alter or enhance *one* functionality. Decomposition into phases with different functionalities but similar crystal structures has only been observed in magnetoelectrics, be it in bulk[108] or thin film materials[48,109,59 ,110] None of those studies make explicitly use of spinodal decomposition.

Self-organized ME composites formed when multiphase targets were used to prepare films by PLD-techniques. In that case, epitaxial strains created the organizing force that lead to the formation of a regular strongly coupled[111,112] two phase 1-3 CFO/BTO nano-composite.[109,110, 113] While it could be demonstrated that this composite had ME character, the determination of ME susceptibilities proved difficult. In this chapter, the synthesis and characterization of a ME composite formed by pseudo-spinodal decomposition is reported. In that case only the innate thermodynamical driving force is utilized to produce a self-organized periodic nano-structured ME composite. If the decomposition is performed in a magnetic field a well-organized laminate with an anisotropic ME susceptibility can be expected. This mode of synthesis was envisioned long ago[108] but not pursued until now.

3. 2 Pseudo-Spinodally Decomposed Nanostructures under Magnetic Field

Textured or anisotropic magnetic materials usually show better performance in technical applications[114,115] than their isotropic counterparts. Among many methods to impose the desired texture and magnetic properties, magnetic field processing has been given special attention in the last few decades.[116,117,118,119] It is only effective during the very early stages of the reaction.[120,121] We used magneto-annealing to synthesize multiferroic $Pb_{1.1}(Zr_{0.53}Ti_{0.47})O_3/NiFe_2O_4$ thin films through a sol-gel spin coating technique.

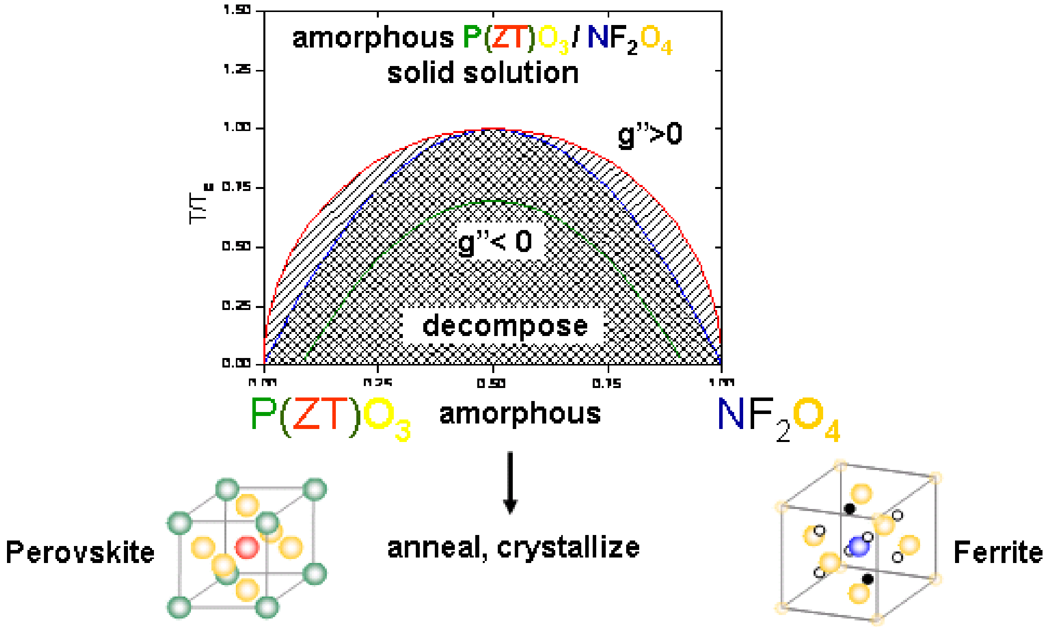

Figure 3.1 Formation of lamellar composite by Pseudo-Spinodal Decomposition

Stoichiometric $Pb_{1.1}(Zr_{0.53}Ti_{0.47})O_3/NiFe_2O_4$ thin films were prepared by thermal decomposition of mixed metal polymeric precursor gels followed by spin-coating onto commercially available oxidized silicon followed by and baking. The polymeric precursor solution was prepared using the Pechini method as described by Calzada:[122] The solutions containing Pb, Zr, Ti and Ni, Fe components were mixed by mechanical stirring at 80 ^{0}C. After refluxing and distilling for 1 h at 80 ^{0}C a lightly red colored sol was obtained which was deposited onto a Au-electroded commercial Si/SiO_2 substrate. Homogenous thin films were obtained by spinning at 3500 rpm for 20 s followed by drying on a hot plate at 180 ^{0}C for 5 min. The resulting approximately 200nm thick films were patterned to facilitate macocroscopic characterization, magneto-annealed for different of times and at different temperatures below the Curie temperature of NFO and finally rapidly cooled to room temperature in zero field. Preliminary DTA measurements (see Figure 3.2) of the baked gels assisted in designing the precise annealing schedule. The magnetic annealing field was directed parallel or perpendicular to the film plane.

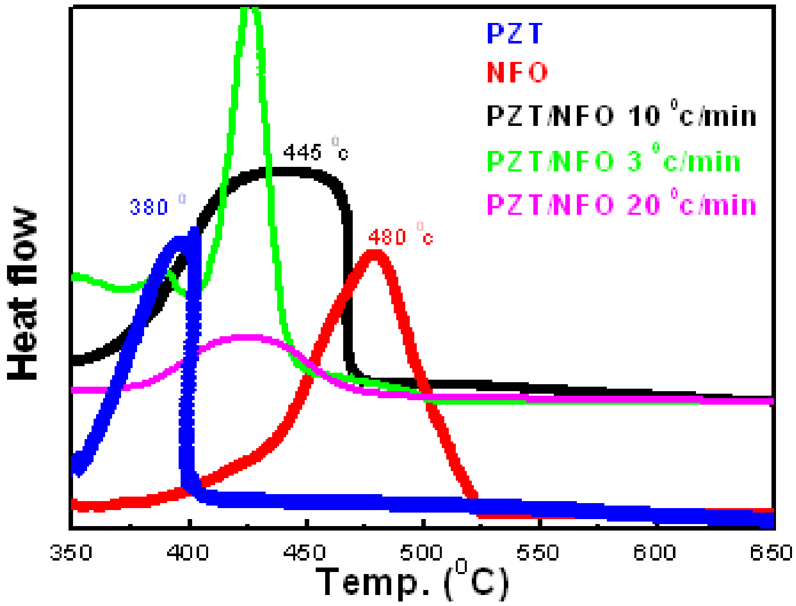

Figure 3.2. The Differential Thermal Analysis (DTA) measurement of PZT/NFO sample

XRD measurements confirmed that the composite consists of perovskite and spinel. The macroscopic characterizations indicated that the ferroelectric and ferromagnetic Curie temperatures of the composite were 20 degrees below the values of individual NFO and PZT films prepared by the sol-gel method used in this study. It may thus be concluded that the chemical compositions of the PZT and NFO components of the composite almost equal that of the “pure” components. Therefore, in the following, the known properties of PZT and NFO will be used in theoretical estimations and the composite will be referred to as a PZT/NFO composite. Selected results of microscopic characterizations are presented in Figs. 3.3 and 3.4 displaying structural, magnetic and compositional information of a film annealed in magnetic fields of 0.6 Tesla directed parallel and perpendicularly to the plane of the film. The images show how the microstructure of the film evolved in the course of the annealing process: Initially, after a short anneal of 2 hours at 460 ^{0}C the structure is dense but amorphous. At longer annealing times of 12 hours at 480 ^{0}C, i.e. below the Curie temperature of NFO, a striped pattern appears. The electron diffraction inset in Fig. 3.3, a, indicates that the composite is now polycrystalline as can also be inferred from the ferroelectric and ferromagnetic characterizations to be discussed below. All microstructures are periodic as indicated by the inserts displaying their Fourier transforms. The periodicity of the microstructure that grew as the magnetic field was directed perpendicularly to the plane of the film, Fig. 3.3, b, is not as clear as that for the parallel case although a diffraction ring can be (barely) discerned. Those transforms indicate the existence of decomposition waves with a wavelength of approximately 25nm. The same periodicity can be seen in the Fourier transform of a Lorentz-TEM pointing out that one component of the ME composite is ferromagnetic. Fig. 3.3, a, demonstrates that the wave vector, $\vec{k}$, of the stationary decomposition wave is aligned parallel to the annealing field, $\vec{H}_a$. The elemental composition analyses confirm that the periodic stripes are composed of NFO and PZT, respectively, see Fig. 3.4. This figure indicates that the chemical composition of the film alternates as it would in a spinodally decomposed solid. In addition, the power density in the upper right points to two standing decomposition waves that are mutually shifted by ½λ as expected.

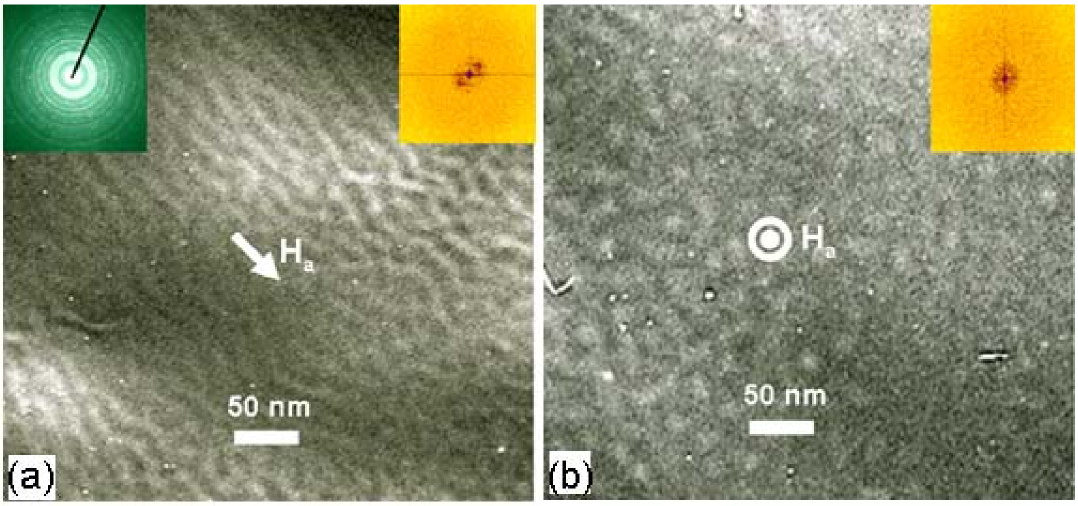

Figure 3.3: Microscopic characterization of the synthesized PZT/NFO composite. a; TEM image of a PZT/NFO sample annealed 12 hours at 480 ^{0}C, i.e. below the Curie temperature of NFO, in an in-plane magnetic field H_a=0.6 Tesla indicated by the arrow. The inset represents the diffraction pattern of the displayed structure, b; annealed in an out-of-plane magnetic field H_a=0.6 Tesla as indicated.

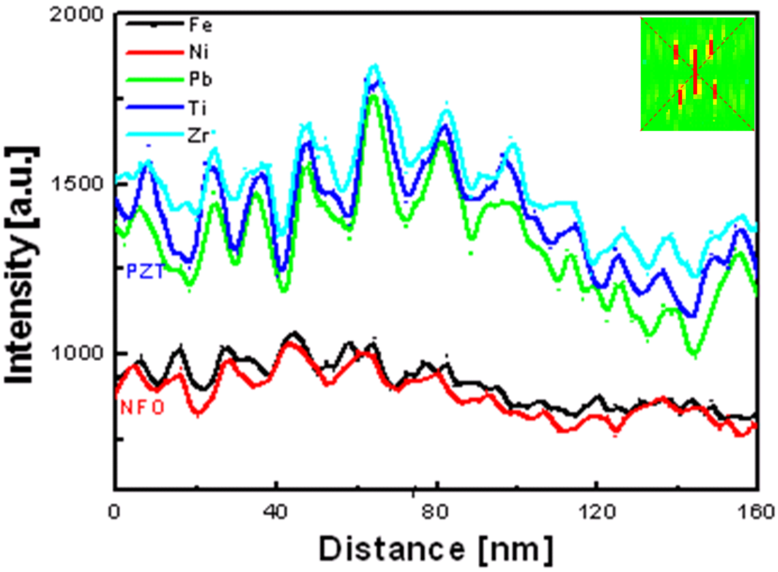

Figure 3.4: Standing compositional waves in the PZT/NFO composite. The noise of this compositional analysis does not permit statements about the exact composition of the PZT and NFO regions. However, it can be seen that the concentration of the two groups of elements, Pb, Zr, Ti and Ni, Fe, forming the PZT and NFO components of the composite are maximized in a periodic fashion. The power Fourier transform displayed at the upper right indicates the existence of two waves. The four maxima indicate their mutual phase shift of ½λ.

3.3 Growth Kinetics of PZT-$NiFe_2O_4$ Nanostructures

The images of the phase-separated film have the appearance of spinodal decomposition. Two kinds of composition waves appear as a solid decomposes under the influence of a magnetic field:[42] (1) waves whose wavelength is affected by the ferromagnetic nature of the solid, termed "parallel waves," and (2) waves whose wavelength is additionally affected by the magnetic poles that form upon decomposition, termed "perpendicular waves." The present experiment favors parallel waves whose wavelength is determined by parameters that are mostly unavailable. For large undercooling, as is the case in this experiment,[37] the wavelengths of the parallel and perpendicular waves approach each other. Hence, the wavelength of perpendicular waves will be estimated since the magnetic parameters controlling them are available. The ensuing wavelength, λ_t, would thus read $\left(\frac{2\pi}{\lambda_t}\right)^2 \approx \frac{\partial^2 s/\partial c^2 \,(T_s - T) + \pi(\partial M/\partial c)^2}{2(K + A)}$,[42] A→exchange energy. It can be estimated by neglecting the derivative of the entropy, s, and the gradient energy, K. By approximating further to finite differences and focusing on the observed structure, $\Delta M^2 = \mu_0 M_T^2$ and $\Delta c = 1$, M_T being the saturation magnetization of NFO at the annealing temperature, it follows that $\lambda_t^2 \approx 8\pi \frac{A}{M_T^2}$. Inserting into this expression an exchange energy for NFO estimated from its Curie temperature, $A \approx 6 \cdot 10^{-7}$ ergcm^{-1}, and the magnetic energy density of NFO determined in this study, $M_T = 30$ emu/cm^3, one obtains for $\lambda_t \approx 12$ nm. This length equals about one half of the observed wavelength, $\lambda \approx 25$ nm, see Fig. 3.3 a. In view of the approximations made the difference of λ_t and λ is not unexpected.

Details of the decomposition/crystallization of the PZT/NFO composite depend, in addition to the temperature, on the size of the applied external field, H_a. The magneto static energy H_aM_s increases the thermodynamic driving force and accelerates the decomposition in addition to favoring those decomposition waves that are aligned with respect to H_a. In the present set of experiments we observed time accelerations by a factor of approximately 20 in isothermally conducted decompositions at 480 ^{o}C. The difference of the SAD patterns of samples annealed and not annealed in a magnetic field indicates that the application of the magnetic field also enhances the crystallization. Under otherwise identical conditions the sample annealed in zero field is amorphous whereas it is crystalline after annealed in a field H_a= 0.6 Tesla. Equivalently, we found that the crystallization temperature is lowered, likely driven by the free energy difference between the non-magnetic amorphous and ferromagnetic crystalline NFO.

3.3.1 Temperature Dependence

PZT-$NiFe_2O_4$ thin films with a thickness of 100 nm were deposited on silicon substrate to investigate the role of growth temperature on the formation of the vertical nano-lamellae. The results show that the stripe nanostructure evolves systematically, as the growth temperature increases from 200 ^{o}C to 480 ^{o}C. As it was suggested from XRD and TEM analyses of the films, no phase separation was observed at growth temperatures below 400 ^{o}C. Since the spinodal decomposition under magnetic field is very temperature sensitive, it can be altered by changing the temperature or cooling rate. However, this has an effect of increasing the wavelength. The other factor affecting the morphology is the magnetostatic energy change. This is ordinarily small except near the Curie temperature. Since NFO phase's Curie temperature is about 480 °C, it has the largest temperature interval for magnetic annealing and also the potential of overcoming the elastic constant anisotropy.

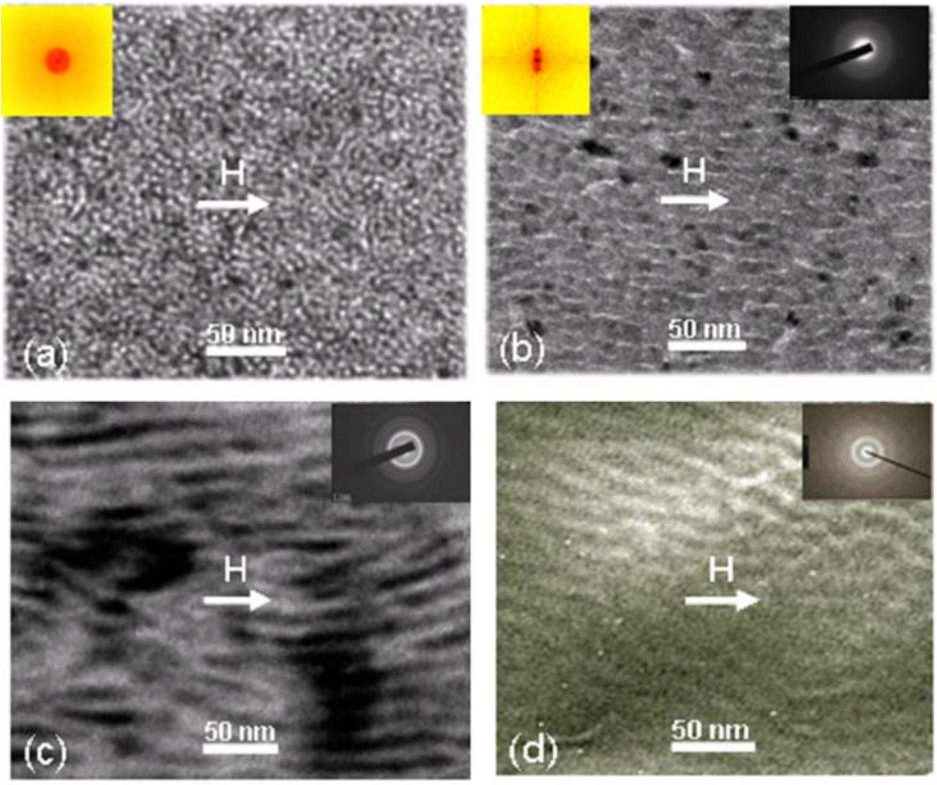

Figure 3.5: temperature dependence microstructure. (a) Gel state 200 °C (b) Amorphous decomposing state 350 °C. (c) Amorphous decomposed state 400 °C. (d) Crystallized decomposed state 480 °C.

3.3.2 Magnetoannealing Time Dependence

The formation of PZT-$NiFe_2O_4$ nanostructures is strongly dependent on the magnetoannealing time. Fig. 3.6 shows the surface morphologies which are taken from the plan view TEM samples grown at 500 °C with different magnetoannealing times. As the time increases, the degree for phase separation of PZT and $NiFe_2O_4$

increases. The figure shows nanostripe features which consist of alternative layers of $NiFe_2O_4$ phase (dark) and the PZT (bright). In the short-time annealed samples $NiFe_2O_4$ nanostripes did not form as we observed in the films with 1 hour annealing. Also, there is a slight misorientation of the $NiFe_2O_4$ phase observed from the Fig. 3.6 a. As annealing time increases, the structure of the annealed sample is distinctly different from the structures grown at larger times. From these results, it was found that the annealing time of about 9 hours at the temperature of 500°C is sufficient to crystallize and align.

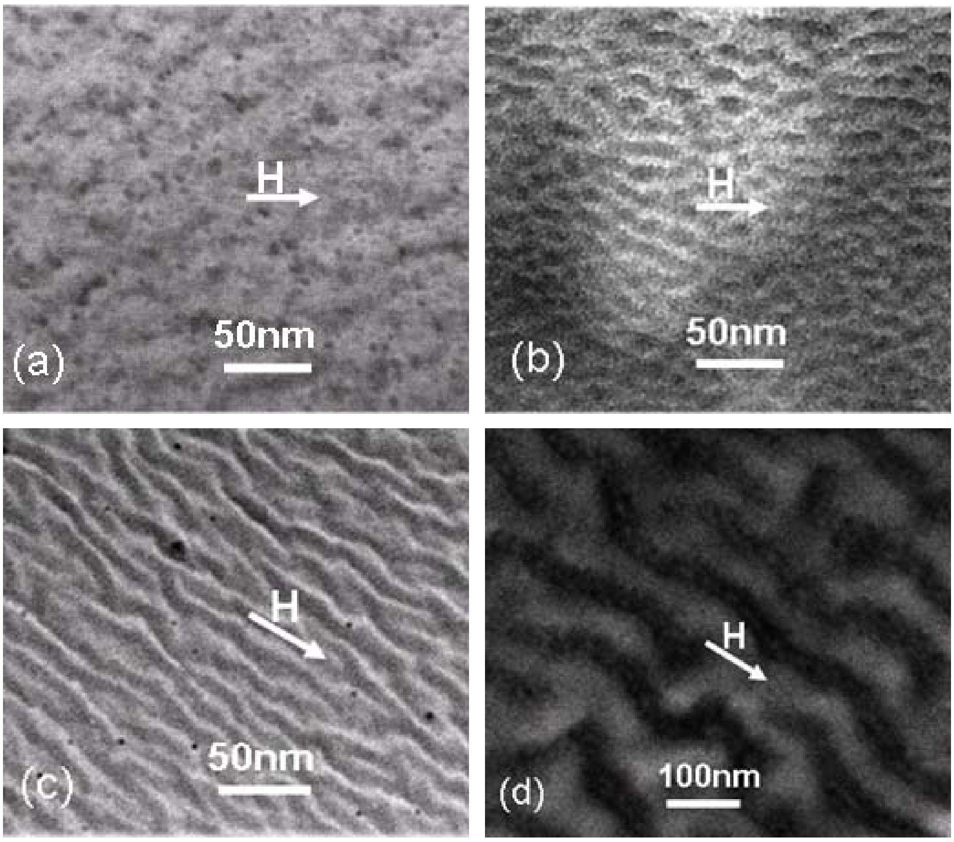

Figure 3.6: magnetoannealing time dependence microstructure at 500 ^{o}C. (a) 1 hour. (b) 4 hours. (c) 9 hours. (d) 16 hours.

3.4.3 Thickness Evolution of PZT-$NiFe_2O_4$ Nanostructure

The spontaneous formation of PZT-$NiFe_2O_4$ nanostructured films is a process that involves rich thermodynamics and kinetics. In order to understand the kinetic and thermodynamic factors governing the nanostructure formation, it is necessary to conduct systematic studies by methodical variation of the growth conditions. For example, in the thin films that were discussed in the previous sections, we evaluated the impact of growth temperature, magnetoannealing time, etc., are based on films with a fixed thickness of 100 nm. Interpretation of the film growth dynamics has been based on observations of the film surface in the final state. However, in order to better understand the growth evolution of the PZT-$NiFe_2O_4$ thin film nanostructure it is necessary to study the microstructure and morphology of films varying film thickness with special attention to the evolution at the film surface.

In this section, we discuss the thickness dependence of PZT-$NiFe_2O_4$ nanostructures. Each of the films can be interpreted as a frozen state after different time intervals during the continuous growth of a thicker film. Fig. 3.7 shows plan view TEM images taken from the samples grown at 500 ^{o}C and 4 hours with thicknesses of about 100 nm, 150 nm, 200 nm, 250 nm, respectively. Striking changes are observed in the patterns as the film thickness increases. Nano-stripes appear in the morphology in the 100 nm thin film (see Fig.3.7 a). At the film thickness reaches about 150 nm, irregularly-shaped domains are observed (Fig.3.7 b). As the thickness is increased further, the irregular domains gradually break and gradually form domains with finite size and with fairly circular shape (see Fig.3.7 c-d). The growth of the domains occurs at the expense of the local inhomogeneous intermediate phases.

As the thickness of the film increases further, the elastic contribution of these two phases to the total energy becomes important. In this stage, the straight interfaces become unstable resulting in break up of the large domains into a much finer domain structure. Therefore, the elastic interaction between these two phases plays an important role in driving the system to form well-organized structures.

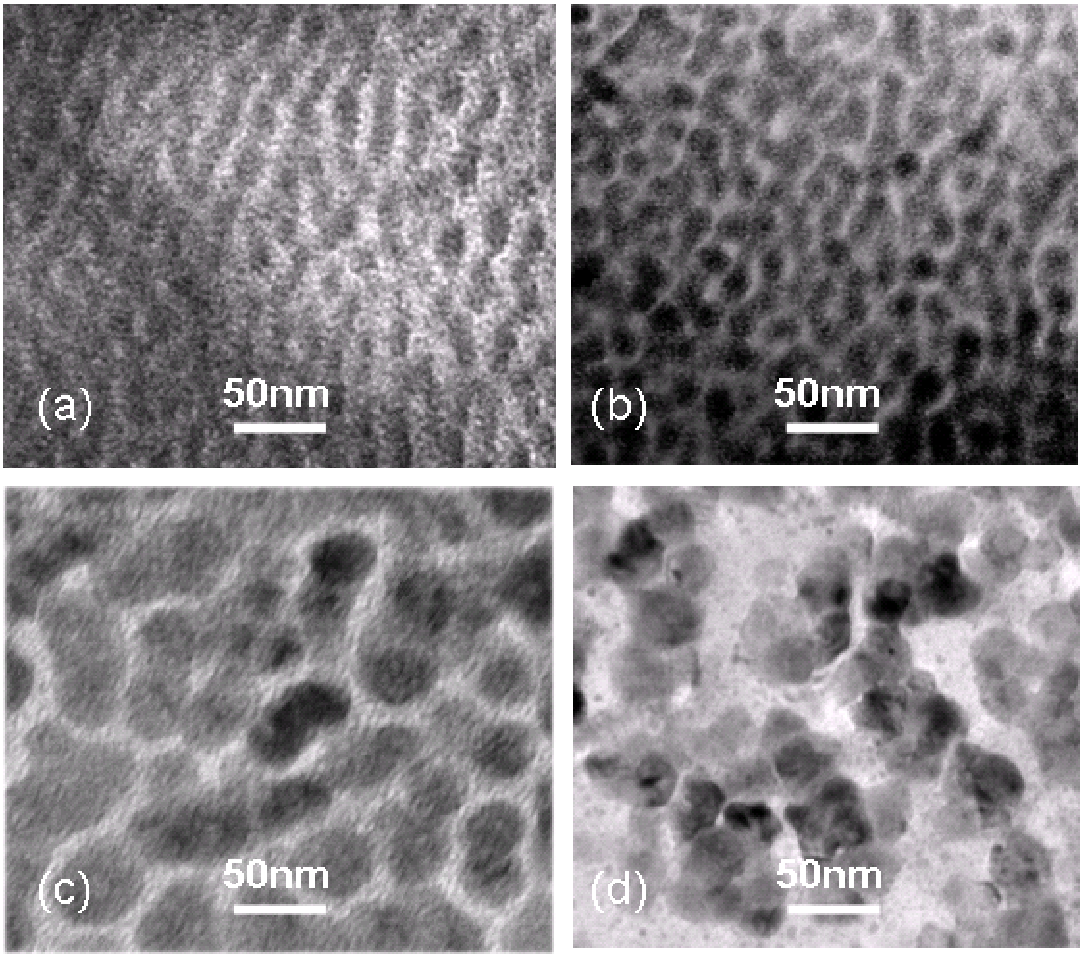

Figure 3.7: thin film thickness dependence microstructure at 500 ^{o}C and 4 hours. (a) 100 nm. (b) 150 nm. (c) 200 nm. (d) 250 nm.

3.4 Ferroelectric /Magnetic Properties in PZT-NiFe$_2$O$_4$ Nanostructures

The macroscopic properties of the ME PZT/NFO composite agree qualitatively and quantitatively with the microstructure, as expected from Fig. 3.3 a. The magnetic domain was investigated by MFM, shown at Fig 3.8. The magnetization curves shown in Fig. 3.9 are anisotropic, i.e. the PZT/NFO composite is magnetically harder when magnetized in the direction perpendicular to the stripe pattern in which the (average) demagnetization factor is larger. The difference of the anisotropy energies in both directions, ΔK, is given by the shaded area in Fig. 3.9, ΔK_{exp}= 0.2*10^6 ergs/cm^3. If this difference is of geometric origin it must equal the difference of the demagnetization energies in the two directions, $\frac{1}{2} M_s^2 \left(N_\perp - N_{//}\right)$. Choosing for M_s the saturation magnetization of NFO, M_s=265 emu/cm^3, and for the difference of the demagnetization factors the limiting value for an ellipsoid, $\left(N_\perp - N_{//}\right) = 2\pi$, $\Delta K_t \approx \pi M_s^2 = 0.22*10^6$ ergs/cm^3. It is noted that $\Delta K_{exp}/\Delta K_t$=0.9 signaling agreement.

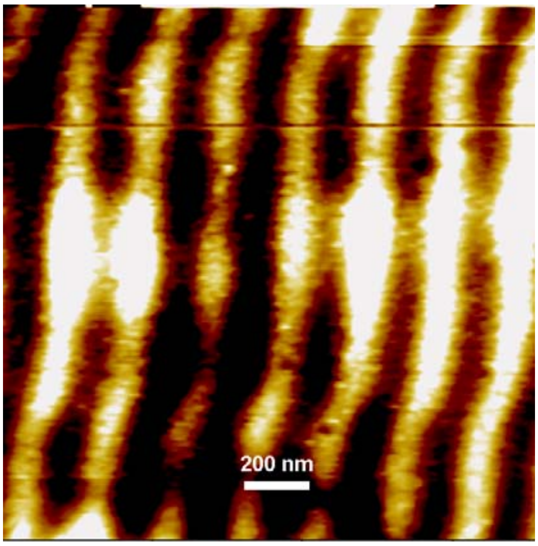

Figure 3.8: MFM image of PZT/NFO sample

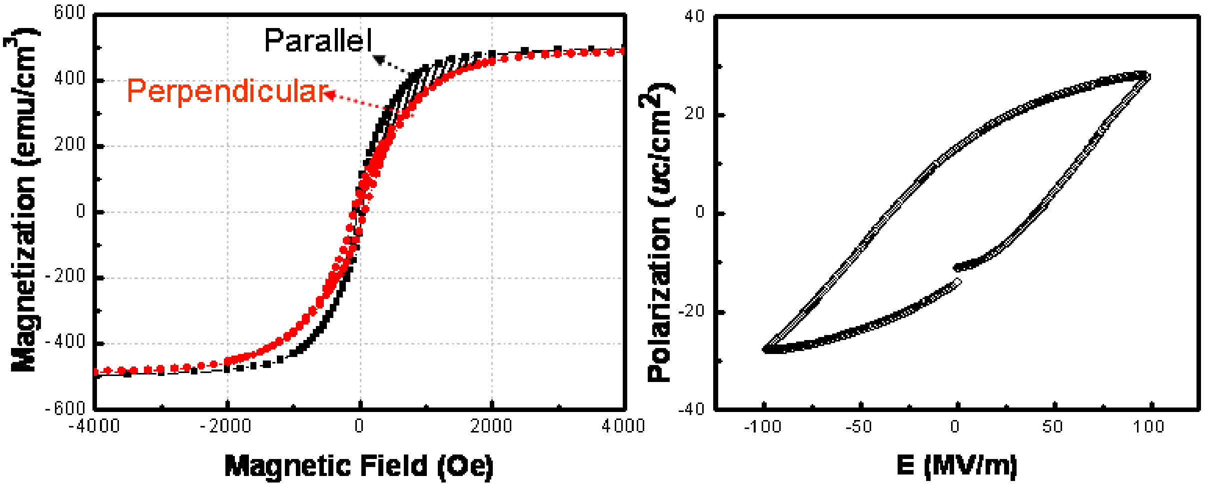

Figure 3.9: Ferromagnetic and Ferroelectric characteristics of a PZT/NFO composite annealed for 12 hours at 480^{0}C in an in-plane magnetic field of H_a=0.6 T. left, ■■■ $\vec{H}_a \parallel \vec{H} \perp \vec{k}$, ●●● $\vec{H}_a \perp \vec{H} \parallel \vec{k}$. The shaded area represents the difference of the demagnetization energies of a rotation ellipsoid parallel and perpendicular to its long axis. Right, ferroelectric P-E loop measurement.

3.5 Magnetoelectric Coupling Effect in PZT-NiFe$_2$O$_4$ Nanostructures

The magnetoelectric coupling between the ferroelectric PZT and ferromagnetic NFO components is elastically mediated, that is, the ME susceptibility $\alpha_H = \frac{\partial P^{PZT}}{\partial \sigma^{NFO}} \frac{\partial \sigma^{NFO}}{\partial H}$ is given by the product of the piezoelectric and magnetostrictive responses of the ferroelectric and ferromagnetic components.[123] Here, the magnetic field was applied perpendicular and parallel to the PZT/NFO stripe-like pattern structure depicted in Fig 3.10, lower inset. The negative magnetostriction of NFO shrinks the PZT thereby decreasing their polarization as shown in Fig 3.10.

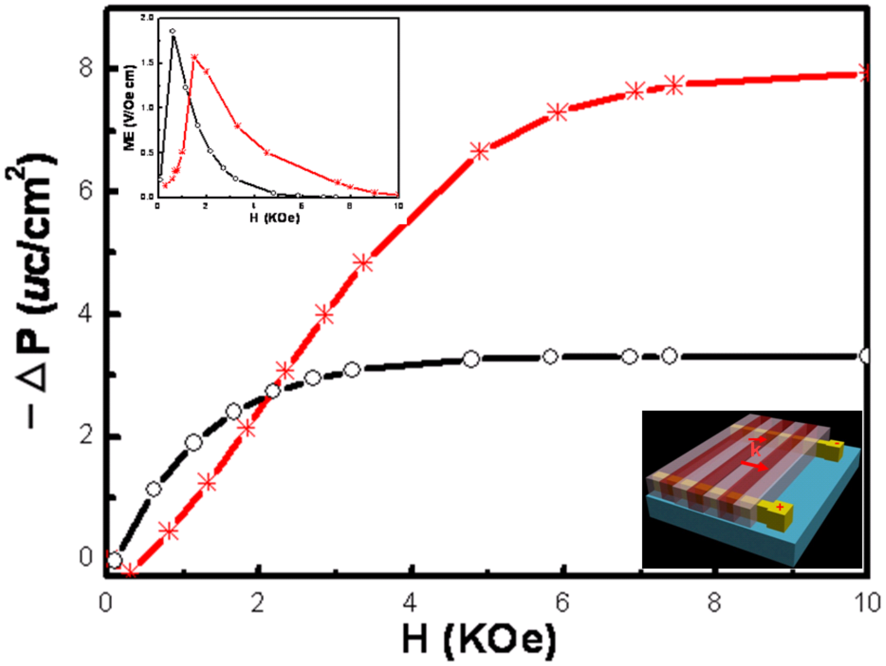

Figure 3.10: Magnetoelectric characteristic and ME susceptibilities (upper inset) of a PZT/NFO film composite annealed for 12 hours at 480^{0}C in an in-plane magnetic field H_a= 0.6 T. ▬ ✳✳✳ $\vec{H}_a \perp \vec{H} \parallel \vec{k}$; ▬ ○○○, $\vec{H}_a \perp \vec{H} \parallel \vec{k}$. The inset on the lower right indicates the placement of the electrodes.

The change in polarization saturates around -8 μC/cm^2 and -3 μC/cm^2 at 10 kOe for the two cases where $\vec{H} \parallel \vec{k}$ and $\vec{H} \perp \vec{k}, |\vec{k}| = \frac{2\pi}{\lambda}$. This saturation is attributed to that of magnetostriction of NFO. The average moduli are evaluated by considering not only the ME composite but also the substrate as shown in Fig. 3.11. The expected magnetically induced parallel and perpendicular polarization of PZT can be estimated

$$\Delta P^{PZT}_{\parallel,t} \approx \frac{4\lambda^{NFO} d^{PZT}_{33}}{\frac{1}{E^{PZT}} + \frac{1}{E^{NFO}} + \frac{2}{E^{SiO_2}}}, \quad \Delta P^{PZT}_{\perp,t} \approx \tfrac{1}{4}\left(E^{PZT} + E^{NFO} + 2E^{SiO_2}\right)\lambda^{NFO} d^{PZT}_{13}$$

λ^{NFO}→magnetostriction constant of NFO. Note that ΔP is independent of the wavelength λ if the composite is symmetrical as is the case here, see insert of Fig. 3.2,

a. However, the magnitude of the wavelength does affect the total charge that is accumulated at the electrodes.

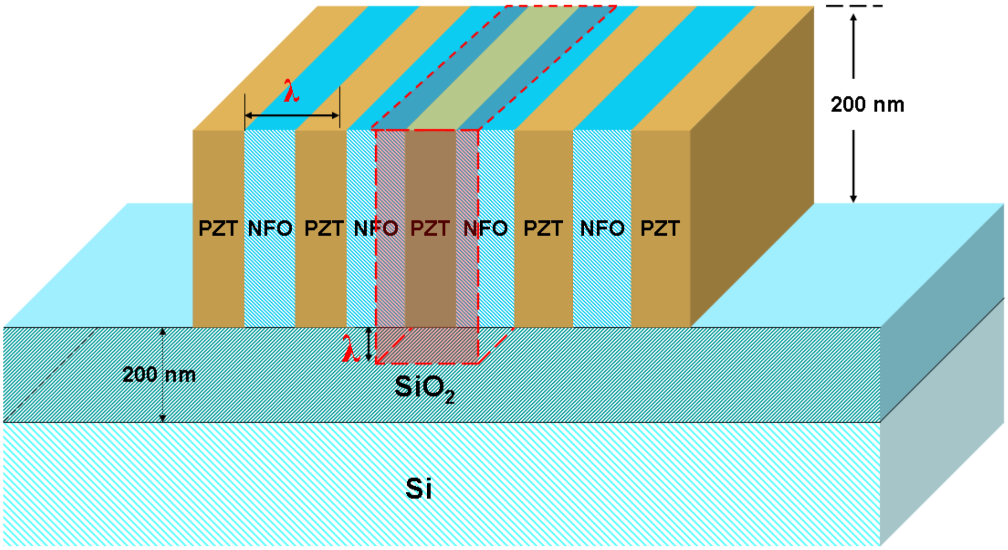

Figure 3.11: Schematic for the evaluation of $<E_{\|}>$ and $<E_{\perp}>$.

With E^{PZT}= 60 GPa, d_{33}^{PZT} =250 pc/N, d_{13}^{PZT} =125 pc/N, λ^{NFO}=-33ppm, E^{NFO}= 200 GPa[124] and E^{SiO_2} =60 GPa[125] $\Delta P_{\|,t}^{PZT}$ = -6 μC/cm^2 and $\Delta P_{\perp,t}^{PZT}$ = -3.9 μC/cm^2. Both expected polarizations agree within 30% with the experimentally observed values, see Fig. 3.10. Using the maximum value of the derivative $\frac{d\lambda^{NFO}}{dH}$ [126] the theoretical estimates for the ME susceptibilities become $\alpha_{H\|,t}$ (PZT/NFO) =2.37 V/cm Oe and $\alpha_{H\perp,t}$(PZT/NFO) =2.4 V/cm Oe. Differentiating the experimentally observed $\Delta P^{PZT} = f(H)$ yields maxima $\alpha_{H\|}$ (PZT/NFO) =1.5V/Oecm and $\alpha_{H\perp}$(PZT/NFO) =1.8 V/cm Oe, see upper inset of Fig. 3.10, corresponding approximately to the above estimates and previous observations.[127] In general, the ME susceptibility is a tensor.[128] Only two of its components are presented here.

3.6 Conclusion

In summary, this chapter demonstrates that magnetoelectrics can be synthesized by pseudo-spinodal decomposition. The observed wavelength of the decomposition wave agrees within a factor of two with the estimated value, and, the experimentally determined macroscopic magnetic and magnetoelectric characteristics of the PZT/NFO ME composite agree reasonably well with those estimated theoretically for the underlying nanostructure. It appears that the method described in this chapter can serve to synthesize a number of functional composites.

Chapter 4
Self-Assembled Multiferroic Nanostructures through Block Copolymer

4. 1 Introduction

Self-assembled ME nanostructures have attracted much interest owing to their potential application in multifunctional devices, transducers, actuators, and sensors.[129, 130] The most critical issue is the control of their size, spacing and distribution of the components. The use of self-assembly to synthesize structured inorganic composites on the nanometer scale is attractive since no special machining, other than combining the “right” components under the “right” conditions is required.[131, 132] Block copolymer self-assembly is particularly interesting. It has several advantages over other methods, in that building blocks promise ultra fine pattern precision and parallel structure formation allows for mass production.[133, 134, 135, 136] Additionally, depending on the volume fraction between the blocks, a variety of morphologies can be formed in which the domain sizes can be tuned from a few nm to several 100 nm by varying the molecular weights. It was thus appealing to use block copolymers as directing agents to form ordered mesostructures in organosilicates.[137, 138, 139] There have also been numerous efforts to use self-assembled block copolymers as a tool for single phase fabrication of nanostructures, and most of the issues have been dealt with in the bulk state.[140, 141] However, none have dealt with two phase structures as we will report here.

Magnetoelectric synthesis via diblock copolymers is very attractive as it can potentially yield a variety of composite geometries. Sol-gel chemistry using block copolymers as a structure-directing agent has been utilized as a useful approach for generating self-assembled single phase nanostructures.[142, 143] Kim reported[144] the use of sol-gel chemistry to fabricate hexagonally packed arrays of titania nano-domains incorporated into poly(ethylene oxide) (PEO) domains (Fig. 4.1). Deep UV light was used to develop the copolymer template. Zhang et al[145] have recently demonstrated that the solvent-annealing of thin films of polystyrene-*block*-poly(ethylene oxide) (PS-*b*-PEO) diblock copolymers leads to highly ordered arrays of PEO cylinders oriented normal to the film surface. The long-range lateral order and the orientation in the annealed PS-*b*-PEO thin films arise from the repulsive interactions between PS and PEO.[146] Highly ordered semiconductor nanostructures have attracted interest due to their potential applications in optical, optoelectronic, magnetic, and micromechanical devices. The most critical issue lies in controlling the size, spacing, and size distribution of the nanoscopic elements

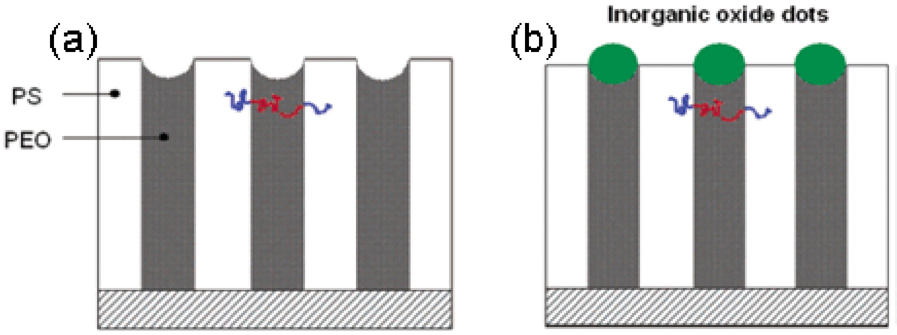

Figure 4.1. Schematic diagram to generate nanoscopic dot array of inorganic materials on PS-*b*-PEO thin film.[146]

It thus appears possible to prepare nano-structured inorganic composites by combining the diblock copolymers' self-organizational powers with sol-gel chemistry. A block copolymer with high order-disorder transition temperature will be preferred as a template to maintain ordered structures during the required heat treatment. PEO is such a polymer that is also known to be soluble in water and alcohol, and block copolymers containing PEO blocks have been extensively studied as nonionic surfactants to direct the self-organization of sol-gel.[147] In this chapter, the synthesis of magnetoelectric cobalt ferrite, $CoFe_2O_4$, (CFO), – lead zirconium titanate, $Pb_{1.1}(Zr_{0.53}Ti_{0.47})O_3$ (PZT), nano-composites based on the above principles is reported. Block copolymers of PS-*b*-PEO were chosen as templates and standard CFO and PZT sol-gel technologies were used. In this manner the pattern created by the diblock copolymer was transferred to the ferroic components.

4. 2 Preparation

The directed assembly of a homogeneous block copolymer with sol-gel composite precursors was achieved using PS-*b*-PEO copolymers. The PZT and CFO components were dissolved in propylene glycol monomethyl ether (PGME) and 2-methxyethanol, respectively, and combined with tetrahydrofuran (THF) which is capable of dissolving PS-*b*-PEO. This method permits to fabricate cylinders or lamellae of almost any type of inorganic material. In order to generate a hexagonal cylindrical morphology, the solutions were mixed in a ratio of precursor volume fraction PEO: PS =0.35.[148] A thin film of block copolymer containing the sol-gel precursors was spin-coated on a pre-treated substrate, solvent dried and annealed at a high temperature.

Commercial polystyrene-*block*-poly(ethylene oxide) (PS-*b*-PEO) (molecular weight 40 000 g mol^{-1}; polydispersity 1.09) with a PEO volume fraction of 0.35 (Polymer Sources Inc.) was used to generate a magnetoelectric nanostructure by heat treatment. A solution of PS-*b*-PEO in THF (10 mg mL^{-1}) was stirred for at least 1 h to ensure complete dissolution. Sol-gel $Pb_{1.1}Zr_{0.53}Ti_{0.47}$ (PZT) and $CoFe_2O_4$ (CFO) precursors were synthesized by mixed metal organic polymerization. The polymeric precursor solution was prepared using the Pechini method:[149] Acetylacetone was added to a mixture of titanium isopropoxide (99%) and zirconium propoxide (99%) with a 1:1 molar ratio of acetylacetone to (Ti, Zr) alkoxides. The solution was refluxed for 2 h at 80 ^{0}C, and lead acetate trihydrate (99%), diluted the lead component with 1,3-propanediol at a 1:5 molar ratio, was added. The final solution was dissolved into propylene glycol monomethyl ether (PGME) solvent. Cobalt 2-methoxyethoxide and iron acetylacetonate metal alkoxide were dissolved in the solvent 2-methoxyethanol. Subsequently, PZT precursor was added into a mixture of PS-*b*-PEO copolymer already containing the cobalt ferrite precursor, stirred for 5 min until a light red colored solution was obtained. The films were prepared on a silicon wafer by spin-coating, at 3000 rpm for 20 s.

The spun-cast films were annealed under chloroform vapor at room temperature for varying amounts of time. After solvent vapor annealing, the wafers were heated to 500 °C at 5 °C/minute and the end temperature was held constant for 2 h to decompose PS-*b*-PEO and crystallize the CFO/PZT composite.

4.3 Self-Assembled PZT-$CoFe_2O_4$ Nanostructure

The morphological evolution of a block copolymer thin film is demonstrated in Fig. 4.2. The figure shows two atomic force microscopy (AFM) images of the gel, Fig. 4.2a, and the crystalline composite, Fig. 4.2b. The self-assembly was assisted by a chloroform atmosphere. The sample was subsequently heated at a rate of 5 ^oC/min to

500 ^{o}C and held there for 2 hours to remove the PS-*b*-PEO and to crystallize the inorganics. The cylindrical nano-domains in the block copolymer thin films were thereby transferred to inorganic ferroelectric-ferromagnetic nanostructures. Highly dense, uniform arrays of hexagonally ordered domains were produced as can be seen from the Fourier transform insets of the height-contrast images.

The AFM/MFM images shown in Figs. 4.2 demonstrate that the nano-composite consist of two components, a ferromagnetic one that appears as dots in Figs. 4.2 b and c, plus one that fills the spaces between those dots. Structural and analytical transmission electron microscopy (TEM) studies were undertaken to determine the cross-sectional distribution of the phases, their local chemical composition and their distribution as well as their crystal structure.

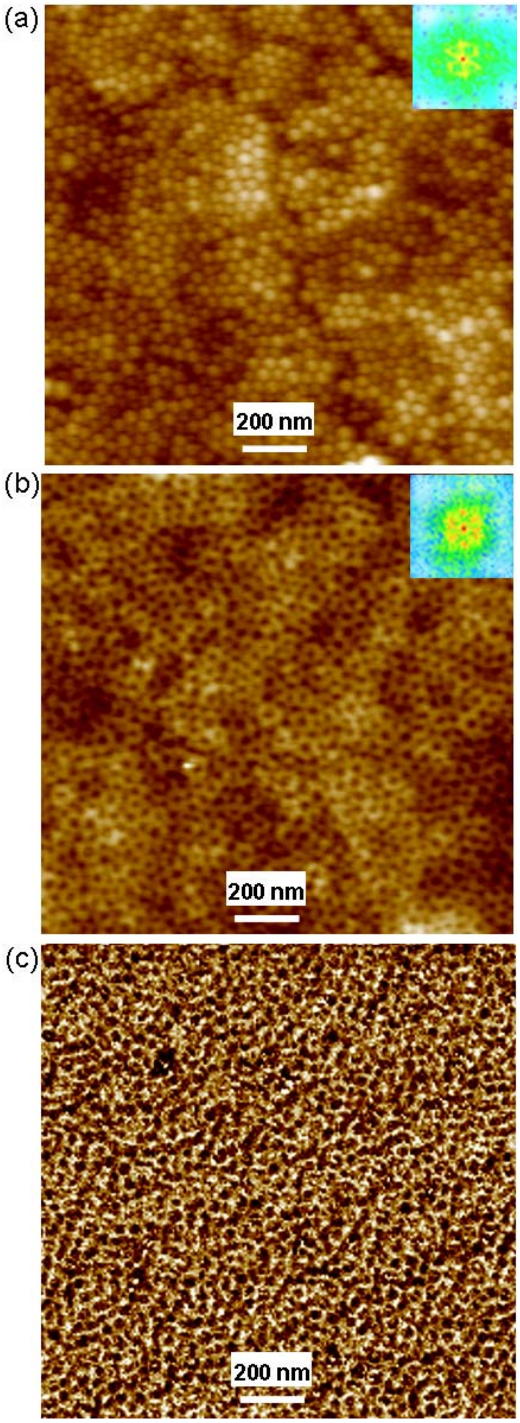

Figure 4.2: AFM images of the PS-*b*-PEO template before and after heat treatment; a, after solvent annealing for 24hours at room temperature; b, after heating at a rate of 5 °C/min to 500 °C and holding for 2 hours. The (fast) Fourier transforms (FFTs) shown as inserts confirm the hexagonal order of the self-assembled gel thin film, a, and crystallized CFO cylinders, b. Section c displays the MFM phase image of the crystallized PZT/CFO nanocomposite.

Results of the structural and chemical observations are presented in Figs. 4.3, 4.4 and 4.5. In conjunction with the AFM images, the composition profile shown below and the HRTEM image of the ME interface region together with its associated composition profile reveal that the magnetoelectric films consisted of cobalt ferrite (CFO) columns that are embedded in a lead zirconium titanate (PZT) matrix: the cross-sectional images of the crystallized film shown in Fig. 4.3a indicate that the cylindrical $CoFe_2O_4$ nano-rods are oriented perpendicularly to the substrate. The elemental composition line-scan displayed in Fig. 4.3b indicates the presence of alternating regions that are either Fe and Co or Pb, Ti and Zr rich. This observation is refined by the EDS spectra obtained from the bright and dark sections of the cross sectional image, Fig. 4.3a, shown in Fig. 4.4. The spectrum of the bright columns indicates only small Co and Fe contents (4.3 at %), and the ratio between Lead (28.79 at %), Zirconium (12.38 at %) and Titanium (12.26 at %), is consistent with PZT. The EDS spectrum of the dark columns shows a 1:2.2 ratio of Cobalt (12.9 at %) to Iron (28.3 at %), which is consistent with $CoFe_2O_4$.The notion that these regions consist of PZT and CFO is further supported by the selected area diffraction (SAD) patterns taken from the respective color coded portions of the cross section, compare Figs. 4.3a and 4.3c. The individual SAD ring patterns were matched to the lattice parameters obtained from self-prepared sol-gel PZT and CFO samples as well as to published data.[150, 151] Figure 4.3c indicates that the two sets match. And, the occurrence of the observed rings agrees qualitatively with the known film textures, (110) for PZT[152] and (311) for CFO[153]. It thus follows that the combined AFM/MFM, meso- and micro-scale structural and chemical analyses indicate that the sample consists of CFO columns that are embedded in a near-regular hexagonal pattern in a PZT matrix.

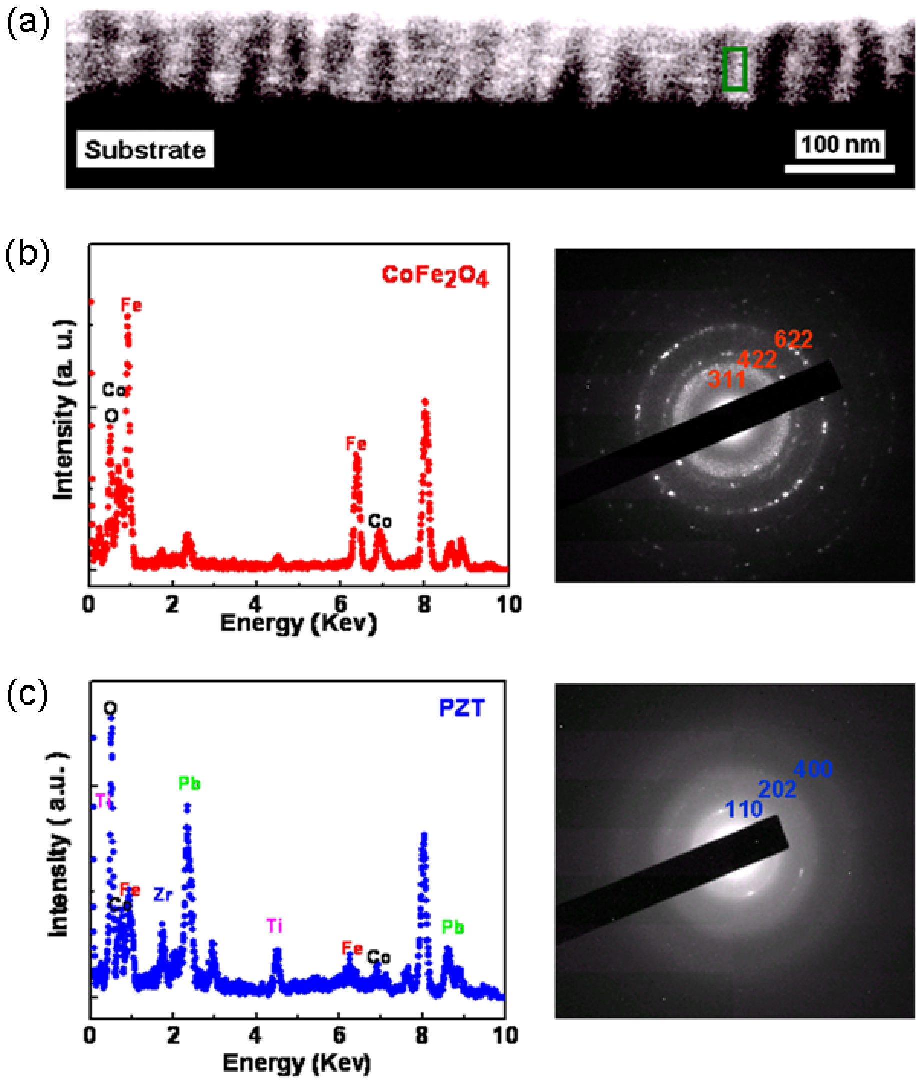

Figure 4.3: TEM results of self-assembled thin film nanostructures; a, Cross sectional TEM image of the PZT/CFO nanocomposite and, b, microbeam EDS elemental composition analysis as well as, c, results of microbeam characterization. The EDS spectrum of the bright columns indicates low Co and Fe content (4.3 at %), and the ratio between Lead (28.79 at %), Zirconium (12.38 at %) and Titanium (12.26 at %), is consistent with PZT. The EDS spectrum of the dark columns shows a 1:2.2 ratio of Cobalt (12.9 at %) to Iron (28.3 at %), which is consistent with CFO. The diffraction patterns were taken at the light and dark locations of the cross section, a, the diffraction rings indexed in red and blue correspond to the known lattice parameters and textures of CFO and PZT.

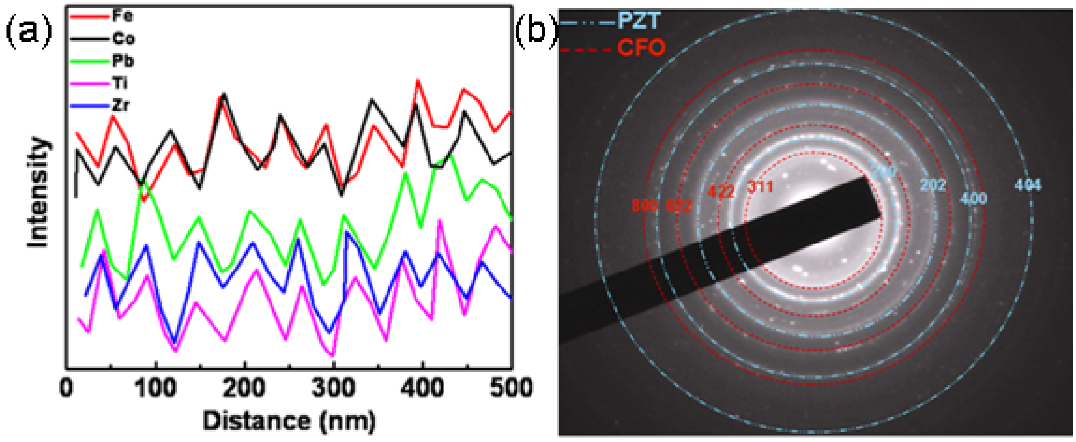

Figure 4.4: Chemical composition analysis; a) microbeam EDS elemental composition analysis and, b) results of SAD characterization. The diffraction pattern was taken over a large area encompassing both the dark and light regions in the cross sectional image shown in Fig. 4.3a.

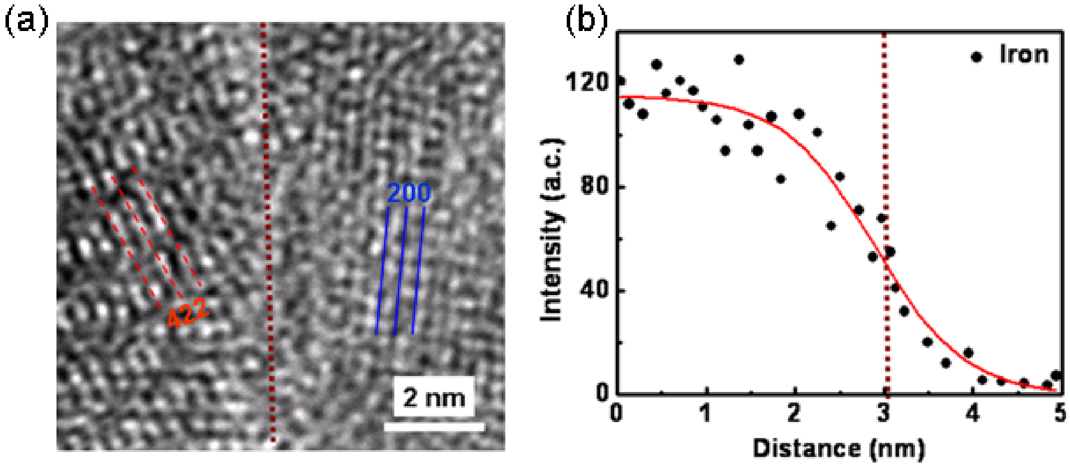

Figure 4.5: High Resolution Transmission Electron Microscopy (HRTEM) image of interface region; a, HRTEM image of the interface region marked in the cross section shown in Fig. 4.3a. The CFO(left)/PZT(right) interface is not epitaxial. The graph below, b, displays the results of the coordinate-matched Fe concentration profile indicating that interdiffusion occurred during the annealing process. Note the difference in scales of Figs 4.5b and 4.3a. If Fig. 4.5b would have been plotted on the scale of Fig. 4.3a the Fe composition profile would appear to be nearly rectangular. The fitting line merely serves to guide the eye.

4.4 Ferroelectric Property in PZT-$CoFe_2O_4$ Nanostructures

Microstructural investigations indicated that after this heat treatment the CFO and PZT components were polycrystalline and single phase, see above. Room temperature vibrating sample magnetometer, magnetic force microscopy (MFM) and 66A Radiant Technologies ferroelectric loop tracer data, prove that the ferro-magnetic and -electric characteristics of CFO and PZT are retained in the nanostructure. The dipolar interaction between the hexagonally arranged CFO cylinders leads to an antiferromagnetically frustrated magnetic ground state[154] with an almost zero remanence as can be seen in Fig. 4.7. The average ferromagnetic characteristics of the assembly, displayed in Fig. 4.7, can be understood in terms of the dipolar interaction energy of nearest neighbor cylinder pairs given by $U_0 = -4\pi\mu_0 \frac{M^2}{D_{12}^3} f(\Theta_1, \Theta_1)$. Here, the angles $\theta_{1.2}$ denote the planar orientation of the cylinders of moment M. The quantity D_{12} represents their distance. The resulting anisotropy energies characterizing the magnetization curves shown in Fig. 4.7 are derived and listed in Table IV that also contains numerical values for the theoretical estimates and the experimentally obtained values. Considering the approximations made, only nearest neighbor interactions, infinite CFO cylinders and substrate clamped electrostriction, the agreement is satisfactory.

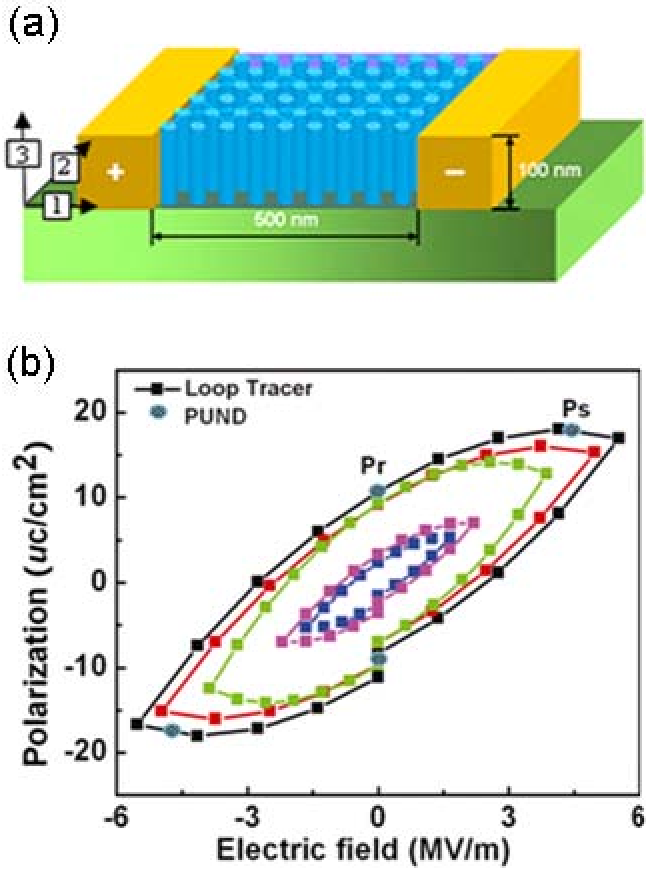

Figure 4.6: a, Schematic of an electroded sample. The electric field E_1 was applied through the electrodes marked "+" and "-." b, well-defined ferroelectric hysteresis of the annealed thin film; the saturation and remnant saturation polarization values, P_r and P_s, resulted from PUND measurements

Table IV: Theoretical and experimental values of the anisotropy energy, experimental shown in Fig. 4.7.

Theory				Exp.
Transition	Anisotropy Energy	Expression	Value [J/m^3]	
Antiferro→ferro	$U_{\uparrow\uparrow} - U_{\uparrow\downarrow}$	$2U_0$	1.1	1.1
Antiferro→collinear	$U_{\rightarrow\rightarrow} - U_{\uparrow\downarrow} + 2\cdot 2\pi\mu_0 M^2$	$-U_0+4\pi\mu_0 M^2$	1.8	1.5
Antiferro→ferro in E_1	$U_{\uparrow\uparrow} - U_{\uparrow\downarrow}+K_E$	$2U_0+K_E$	1.9	1.7

4.5 Magnetoelectric Coupling Effect in PZT-$CoFe_2O_4$ Nanostructures

The CFO/PZT nanostructure shown here corresponds to a 1-3 composite, which, among all ferromagnetic/ferroelectric composites, optimizes the ME interaction. For the present study the electro-and magneto-mechanical interaction coefficients $d_{13}^{PZT}>0$ and $\lambda_s^{CFO}<0$. Therefore, an electric field, E_1, applied perpendicularly to the axis of the CFO cylinders, see Fig. 4.6 for notation, will reduce their average magnetization as can be seen in Fig. 4.7. The total anisotropy energy of the cylinders magnetized parallel to their axes and subjected to a perpendicular electric field will be given by $U_{\uparrow\uparrow}-U_{\uparrow\downarrow}+K_E=2U_0+K_E$. The quantity K_E denotes the magnetic anisotropy energy density of the CFO cylinders created by the electromechanical stress exerted by the surrounding PZT matrix that can be approximated by $K_E \approx \frac{3}{2}\lambda_S^{CFO}\left[\frac{\left(\frac{1}{2}D_{12}\right)^2-r^2}{\left(\frac{1}{2}D_{12}\right)^2}Y^{PZT}+\left(\frac{r}{\frac{1}{2}D_{12}}\right)^2 Y^{CFO}\right]d_{31}E_1$. Table IV indicates that all anisotropy energy densities are of similar magnitude. It can thus be expected that the application of an electric field to the PZT matrix will reduce the magnetization of the CFO cylinders noticeably. The data shown in Fig. 4.7 confirm this expectation. They demonstrate that the initial permeability, μ_i, can be changed significantly by the application of an electric field: the ratio $\frac{\mu_i(H_3)}{\mu_i(H_3+E_1)} \approx 5$ leading to the corresponding coupling coefficient, $ME_E \approx$ 25 V/A (20V/Oecm). The magnitude of the coupling coefficient is the result of the balanced magnetic, magneto- and electromechanical energies and the absence of epitaxial bias stresses. The latter is due to the relaxed nature of the magetoelectric CFO/PZT interface displayed in Fig. 4.7.

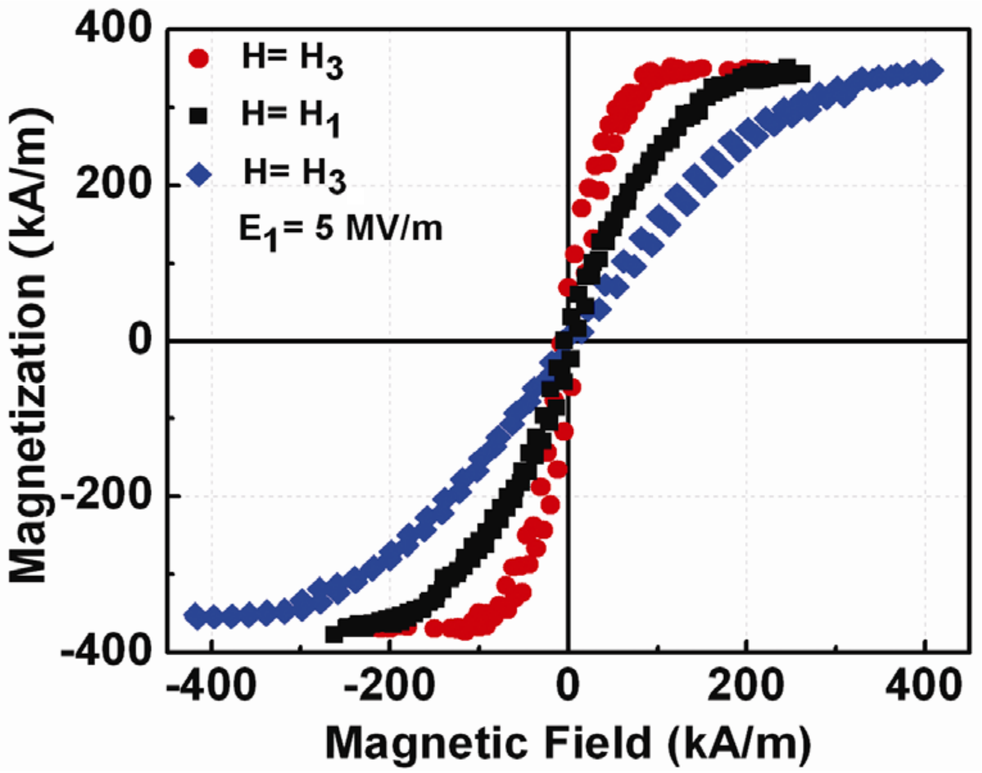

Figure 4.7: Ferromagnetic and ME characteristics of the hexagonal CFO cylinder array embedded in a PZT matrix magnetized parallel and perpendicularly to their axes, H_3, ●●● and H_1, ■■■, and, with an applied magnetic, H_3 plus electric field, E_1, ◆◆◆. The permeability of the nanostructure can be changed by the application of an electric field. The ratio of the initial permeabilities, $\frac{\mu_i(H_3)}{\mu_i(H_3,E_1)} \approx 5$.

4. 6 Appendix: Numerical Calculation of Dipole and Magnetoelectric Energies

Evaluation of the Dipole Interaction Energies

The full expression for the angular dependence of the dipolar interaction energy is given by $U = -U_o f(\Theta_1,\Theta_2) = -4\pi\mu_0 \frac{M^2}{D_{12}^3}\left[2\cos\Theta_1\cos\Theta_2 - \sin\Theta_1\sin\Theta_2\right]$. The resulting interaction energies for the antiparallel, collinear and parallel states are derived in Table V below. This Table also includes the demagnetization energy that must be supplied by the external magnetic field to set up the collinear state. Here, the demagnetization factor, 2π, has been used. The additional factor of two accounts for two cylinders. The resulting anisotropy energies $U_{\uparrow\uparrow} - U_{\uparrow\downarrow}$ and $U_{\rightarrow\rightarrow} - U_{\uparrow\downarrow} + 4\pi M^2$ have been entered into Table V of the main text that also includes the anisotropy energy $U_{\uparrow\uparrow} - U_{\uparrow\downarrow} + K_E$ where K_E represents the electrically induced anisotropy energy to be derived below.

Table V: Evaluation of the Dipole Interaction energies U

State	Symbol	Θ_1	θ_2	Interaction energy	Demagnetization energy
Antiparallel	$U_{\uparrow\downarrow}$	π /2	-π /2	$-U_0$	0
Collinear	$U_{\rightarrow\rightarrow}$	0	0	$-2U_0$	$2 \cdot 2\pi M^2$
parallel	$U_{\uparrow\uparrow}$	π /2	π /2	U_0	0

Derivation of the Magnetoelectric Anisotropy Energy Density of the PZT/CFO Composite

Figures 4.3, 4.4 and 4.5 together with the magnetic, electric and chemical characterizations discussed above demonstrate that the nanostructure under investigation consists of a regular array of CFO cylinders embedded in a PZT matrix. Therefore, the magnetoelectric energy density of a single CFO cylinder surrounded by a concentric PZT cylinder, K_E, will be derived with the goal to account for the electrically induced anisotropy shown in Fig. 4.7 of the main text and included with Table IV. The electromechanical strain tensor of the two dimensional space of interest shown in Fig.4.6 is given by $\varepsilon_i = d_{ij} E_j$, i,j=1,3 where the coefficients d_{ij}

represent the electromechanical coupling constants. The electric field E_1, applied to this structure, strains this "polycrystal," by $\varepsilon_{31}=d_{31}E_1$ and $\varepsilon_{11}=d_{11}E_1$. Since the system is elastically constrained by the substrate $\varepsilon_{11}=0$, hence $\sigma_1(E_1)=0$. The strain ε_{31} creates a stress $\sigma_3\approx Y_{ave}d_{31}E_1$ where Y_{ave} represents the average elastic modulus of the PZT/CFO composite. The magnetic anisotropy energy of the polycrystalline CFO cylinder is then determined by $K_E = \frac{3}{2}\lambda_S^{CFO}\sigma_3 = \frac{3}{2}\lambda_S^{CFO}Y_{ave}d_{31}E_1$. Approximating Y_{ave} by that of a cylindrical parallel composite consisting of the CFO core surrounded by a PZT shell of inner and outer radii r and $\frac{1}{2}D_{12}$,

$$Y_{ave} = \frac{\left(\frac{1}{2}D_{12}\right)^2 - r^2}{\left(\frac{1}{2}D_{12}\right)^2}Y^{PZT} + \left(\frac{r}{\frac{1}{2}D_{12}}\right)^2 Y^{CFO} \qquad (4.1)$$

It follows that

$$K_E \approx \frac{3}{2}\lambda_S^{CFO}\left[\frac{\left(\frac{1}{2}D_{12}\right)^2 - r^2}{\left(\frac{1}{2}D_{12}\right)^2}Y^{PZT} + \left(\frac{r}{\frac{1}{2}D_{12}}\right)^2 Y^{CFO}\right]d_{31}E_1 \qquad (4.2)$$

Numerical Calculations

The following entries were used for the evaluation of K_E, πM_S^2 as well as the dipolar and demagnetization energies: $M_S^{CFO} = 3.5\cdot10^5 A/m^3$, $\lambda_S^{CFO} = -350\cdot10^{-6}$,[155] $d_{13}^{PZT} = 125\cdot10^{-12}C/N$,[156] $Y^{CFO} = 140GPa$,[37] $Y^{PZT}=60GPa$,[157] $E_1=2\cdot10^7 V/m$. The quantities D_{12} and r represent the separation of the CFO cylinders. The values $D_{12}\approx4.5r$, r=12nm were chosen because they are in accord with the structural observations and lead to a reasonable fit in Table IV.

The dipolar interaction energy was evaluated using $U_0 = -4\pi\mu_0 \frac{M^2}{D_{12}^3}$ where the M's represent the moments of neighboring cylinders. With the observation that the magnitude of the moment and spontaneous magnetization are related as $M=VM_s$, V is the cylinder volume and M_s its spontaneous magnetization, it follows that the dipolar energy density is given by $U_0 = -4\pi\mu_0 \frac{M_s^2(\pi\ell r^2)^2}{D_{12}^3(\pi\ell r^2)}$, r and ℓ being the radius and length of a representative cylinder. The resulting numerical values are then U_0=0.53 J/m^3, K_E =0.84 J/m^3 and $2\pi M^2$=1.1 J/m^3.

4.7 Vertical Multilamellar Ordered Nanostructure through Block Copolymer

The morphological evolution of a block copolymer thin film is demonstrated in Fig. 4.8. by atomic force microscopy (AFM) images of the ratio PS-*b*-PEO (PEO:PS =0.6) thin films with PZT/CFO multiferroic sol-gel precursors. Solvent (chloroform, approximately 10 nm thick with 1 wt % solution) evaporation causes a strong and unidirectional field that induces self-assembly and propagates ordering through the entire film. Highly dense, uniform arrays of lamellar domains were produced as can be seen from the height-contrast images (Fig. 4.8). The samples were subsequently heated at a rate of 5 ^{o}C/min to 500 ^{o}C and held there for 2 hours to remove the PS-*b*-PEO and crystallize the inorganics. The lamellar microdomains of block copolymer thin films were thereby transferred to inorganic ferroelectric-ferromagnetic nanostructures, see Fig. 4.8.

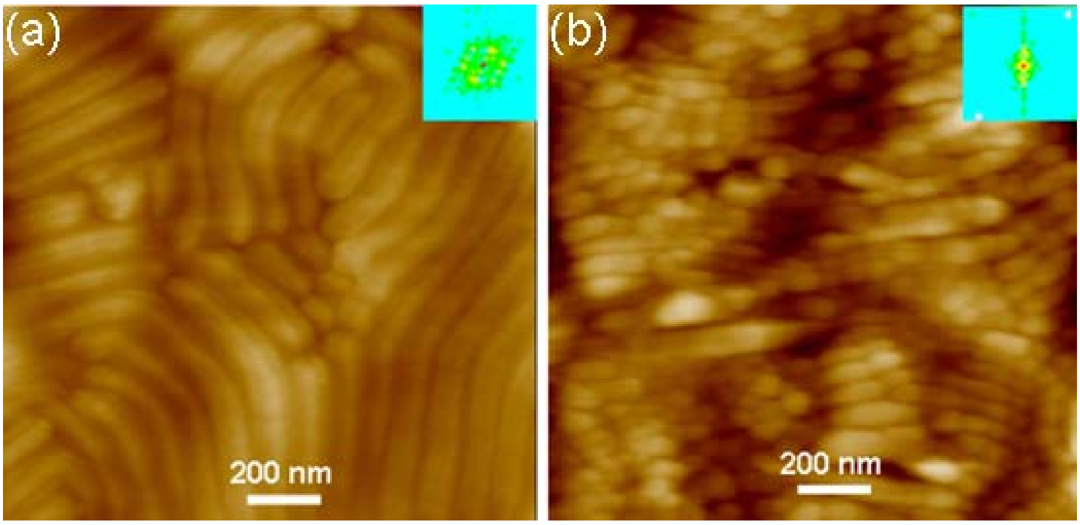

Figure 4.8: AFM images of the PS-*b*-PEO template before and after of heat treatment at the PS-*b*-PEO ratio (PEO:PS =0.6); left, after solvent annealing for 24hours at room temperature; right, after heating at a rate of 5 ^{o}C/min to 500 ^{o}C and holding it for 2 hours. The FFTs shown as inserts confirm the 1D order of the CFO lamellae.

If the multilamellar thin film sample was in a magnetic field of different strength directed perpendicularly to the film surface, onion-type nanostructures were induced. Rings with up to 46 layers, a period of 15 nm and diameters as large as 1.5 μm, can be seen. A Transmission electron microscopy (TEM) image of the resulting domain structure is shown in Fig. 4.9. Energy dispersive X-ray spectrometer (EDS) spectra obtained from the bright and dark rings of the film confirms the chemical composition of the separated blocks. In this state and at room temperature the domains are superparamagnetic and strongly paraelectric, respectively.

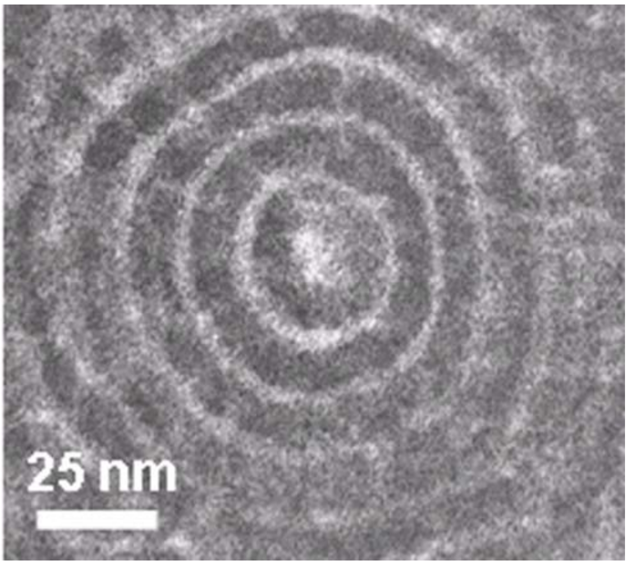

Figure 4.9: TEM cross section of the 2D onion domain structure created by annealing a PS/PZT-b-PEO/CFO polymer for ≈ 0.2 Ms (64 hours) in a magnetic field of 0.8 T. The PZT and CFO precursors serve as contrasting agents.

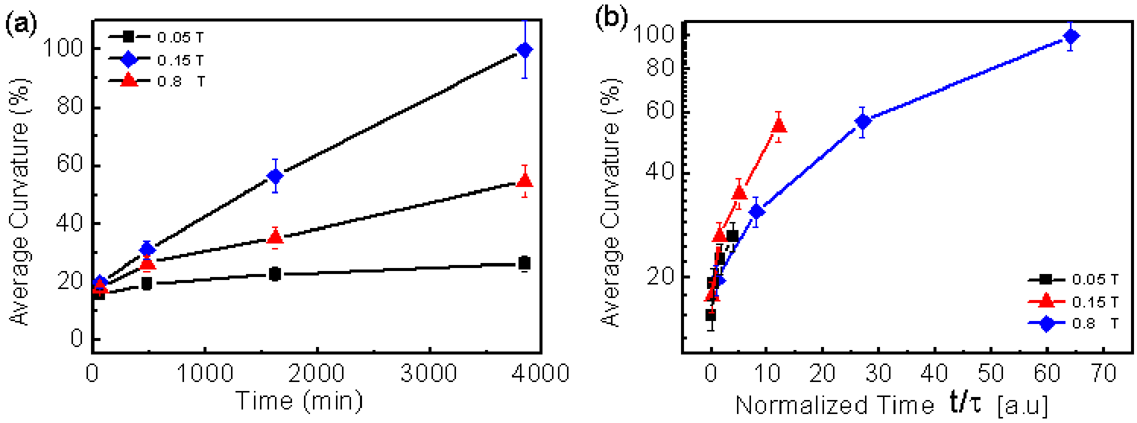

Figure 4.10 Initial growth kinetics of the 2D onion evolution in a PS/PZT-b-PEO/CFO polymer thin film in the presence of a magnetic field B. a, raw data; b, data normalized according to eq. (2): ■■■ B_1= 0.05 T, ▲▲▲ B_2= 0.015 T, ◆◆◆ B_3= 0.8 T.

The kinetics of the 2D onion evolution has been analyzed using Gwyddion software[158] which determines the average curvature of the lines seen in the AFM nanostructures. Figure 4.10 presents the raw and normalized data. The analysis leading to the normalization is based on the observation that the paraelectric precursor, likely an associated electric charge, is required for the 2D onion-type formation, which points to a Lorentz force driven organization mechanism. This force is given by $\mathbf{F}=q[\nabla \mathbf{A} x \mathbf{v}]$ where the three variables q, **A** and **v** denote the charge(s) in the PZT precursor, the magnetic vector potential due to the applied field and the thermodynamic diffusion velocity of the polymer. This driving force can be included with the Cahn-Hilliard equation describing the evolution of the lamellar order[159,160] by adding the Lorentz term that drives the curvature. The linearized equation that can model the initial evolution of the observed 2D onion structure is then

$$\frac{\partial \Phi}{\partial t} = M[(g_{\Phi\Phi} + qB)\frac{\partial^2 \Phi}{\partial x^2} + (g_{\Phi\Phi} - qB)\frac{\partial^2 \Phi}{\partial y^2} - K(\frac{\partial^4 \Phi}{\partial x^4} + \frac{\partial^4 \Phi}{\partial y^4})],\ g_{\Phi\Phi}<0. \tag{4.3}$$

The symbols M, $g_{\Phi\Phi}$ and K denote the polymer chain mobility, second derivative of the free energy and gradient energy, respectively. The maximal radial growth velocity with the wave vector $k_{r,m}^2 \propto \frac{qB}{K}$ leads to the characteristic time of the initial exponential evolution of the curvature, $\tau_{r,m} \propto \frac{1}{k_{r,m}^2 D}$, D=MkT – diffusivity. The kinetic raw data shown in Fig. 4.10, a, can therefore be normalized as

$$\frac{t}{\tau_i} \propto \frac{t}{B_3/B_i} \tag{4.4}$$

where the indices of the flux densities refer to the data sets indicated in the caption of this figure. Hence, the time axis of the kinetic data can be normalized as $t' = t \cdot B^{(i)}/B^{(j)}$. It can be seen from Fig. 4.10 b, that the initial exponential growth of the curvature does normalize approximately in that fashion in agreement with the assertion that the Lorentz force induces the 2D onion structure. Further growth must be described by the full nonlinear extension of the analysis. Fast Fourier transforms (FFTs) corresponding to the sequence of AFM images in Fig. 4.11, displayed in Fig. 4.12, demonstrate the conceptual evolution of the 2D onion morphology: the known laminar pattern evolves if the anneal is conducted without a magnetic field; at small magnetic fields lamellar order predominates; at intermediate fields a modulated two dimensional lamellar structure appears while upon further increasing the magnetic field to 0.8T the 2D onion structure develops. The FFTs indicate that for small fields, B, lamellar order predominates but an increasing Lorentz force modulates the emerging lamellae as signaled by the FFT in Fig. 4.12 taken after an anneal of 3840 min at 0.05 T. For large magnetic fields the kinetics will approach the overdamped steady state motion of a charge in a magnetic field. Circular loops are formed, which, in the presence of a persistent lamellar order, become concentric cylinders separated by the interlamellar distance. We have observed similar diffusion enhanced dislocation free self-organization of plane-parallel lamellae in electric fields.

The onion-type nanostructures presented here may be technologically useful. Similar materials, termed mesoporous multilamellar vesicles, have been the synthetic target of numerous investigations, because the structures could serve as efficient catalyst supports, adsorbents or controlled-release materials for drug delivery.[161,162,163] Wiesner et al were able to synthesize Au core/silica shell nanoparticles by tailoring their size distributions.[164] For most applications, it is desirable that the vesicle core and shell have different compositions, which is usually difficult to achieve. The present approach opens a simple pathway to the design of such compositionally heterogeneous structures.

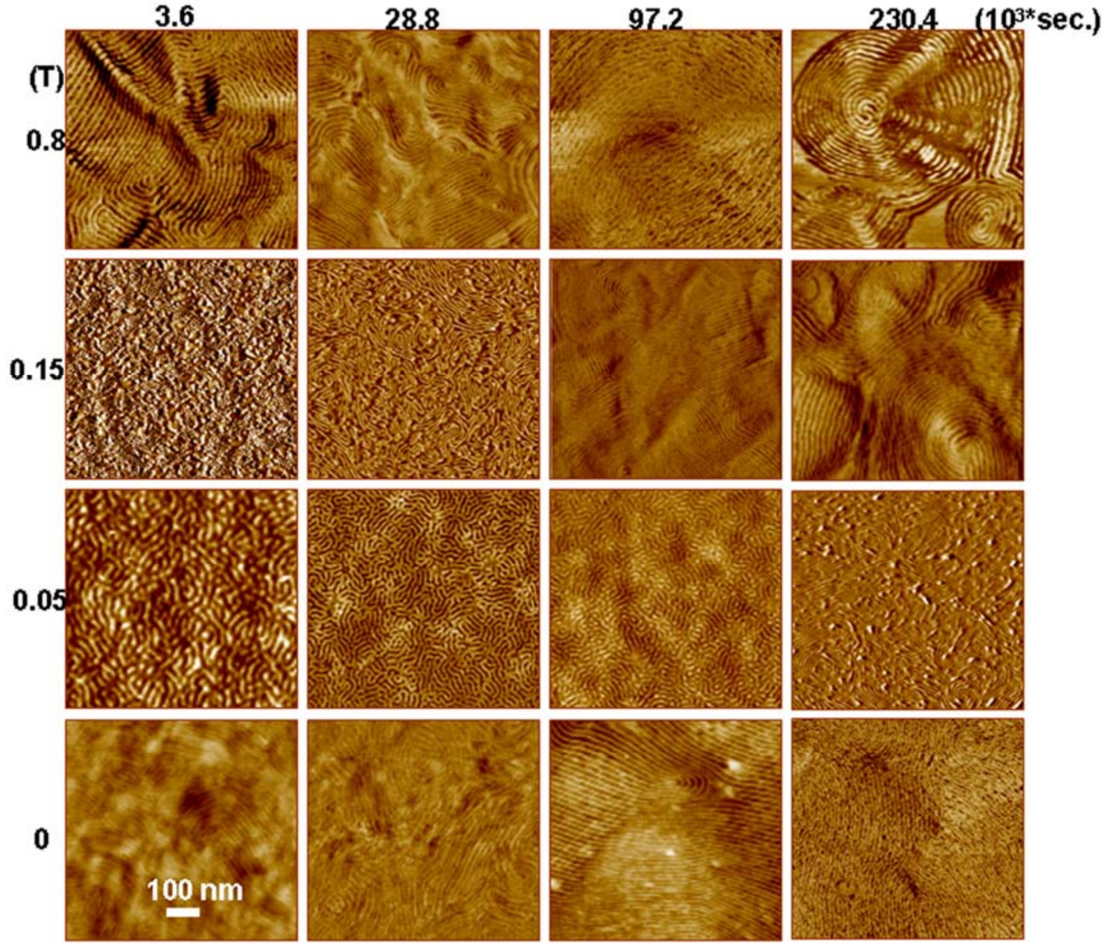

Figure 4.11: AFM phase images of the nanostructures created by room temperature annealing of a PS/PZT-b-PEO/CFO polymer for times as long as ≈ 3840 min (64 hours) in magnetic fields as high as 0.8 T.

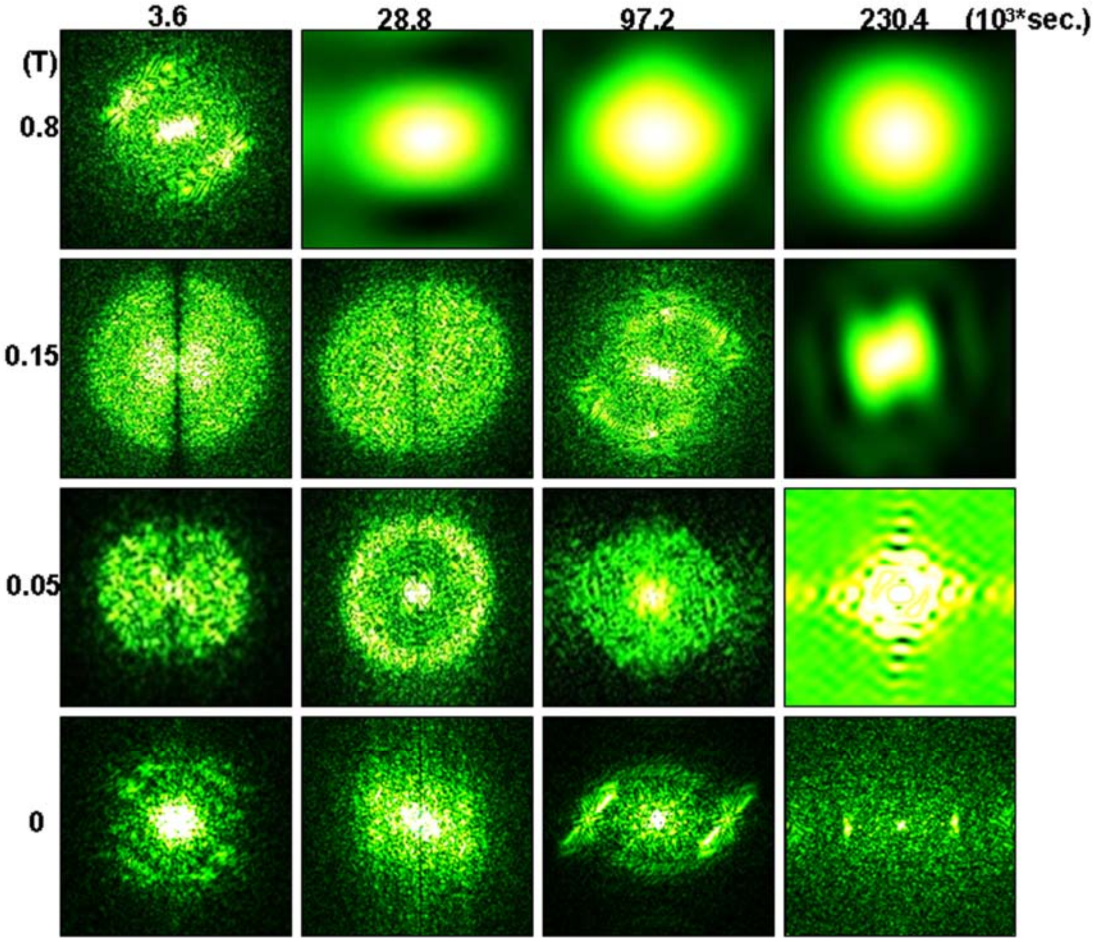

Figure 4.12 Fast Fourier transforms corresponding to the sequence of AFM images

4.8 Conclusion

In conclusion, in this chapter, a novel, simple and inexpensive synthesis route to highly dense arrays of self-organized patterned ME composites using thin-film block copolymers combined with sol-gel chemistry was invented and used to fabricate a strongly coupled ME. Thin films with a CFO precursor in a cylindrical PEO domain and a PZT precursor in the surrounding PS domain were obtained by spin-coating and subsequent heat treatments the latter leading to crystallization. The ferromagnetic, –electric and magnetoelectric characteristics of the film all suggest that the PZT and CFO precursors were selectively incorporated into the PS-*b*-PEO hybrid system. The formation of the magnetoelectric thus corresponds to the "four-phase scenario"[165] in which an interfacial layer of pure PEO lies between the PS and the PEO separating the PZT and CFO precursor mixtures. The method is generally applicable to the synthesis of any two-phase inorganic composite. Specific material combinations and patterns can be selected through the nature of the precursors and the ratio of the diblock copolymer. The ferromagnetic, ferroelectric and ME characteristics are equally tunable over a wide range of parameters as can be seen from the expressions for the controlling magneto- and electromechanical energy densities.

Chapter 5

Spontaneous Phase Separated Multiferroic Bi-Crystal

5. 1 Introduction

The phase separation at nanoscopic length scales in chemically homogeneous complex oxide systems and the resulting multi-functionality is a research area of growing interest in both fundamental science and application oriented technology.[166,167,168] Solid-state self assembly is an especially intriguing approach that has been used recently to form regular morphologies on a nanoscale in a series of perovskite or spinel solid solutions, which phase separate to form pseudoperiodic chessboard-like structures with promising potential functionalities.[169,170,171,172] We used this approach to improve on previous eutectoid[173] and other[174,175,176,177,178,48] syntheses of CFO/BTO composites. Van den Boomgaard[21] *et al.* already demonstrated that directional solidification of eutectic BTO-CFO leads to lamellar microstructures. Phase separated self-assembled BTO/CFO 3D nanostructures are also formed in pulsed laser deposited films.[48] Despite the elegance of this method, economically motivated efforts are continuing[179,180] to synthesize magnetoelectric composites by conventional ceramic processing. However, the resulting micro- or nano-structural control is generally unsatisfactory. Here, we present a novel approach of preparing a periodic two-dimensional lamellar BFO/CFO nanostructure that persists throughout entire crystal grains. We have discovered that the quinary system Fe-Co-Ti-Ba-O spontaneously phase separates into a superlattice of epitaxially joined ferromagnetic CFO and ferroelectric BTO nano-lamellae. This remarkable structure is mediated by the framework of oxygen octahedra that dictates the extraordinary perfection of the CFO/BTO superlattice. Compared to recent reports on other multiferroics[181,182,183], this spontaneous phase separated perovskite-spinel system is unique in many respects. It is a naturally grown nano-lamellar bi-crystal with a large initial ferromagnetic susceptibility and at the same time a ferroelectric relaxor permitting large magnetoelectric tunability.

5.2 Self-Assembled $BaTiO_3$-$CoFe_2O_4$ Nanostructures

Powder samples of BTO-CFO (1:1 ratio) were prepared by a modified PECHINI method.[184] X-ray diffraction (Fig. 5.1) and electron elemental line scan characterization show two set of features matched with the perovskite and spinel phases, consistent with the phase diagram of the quinary system Fe-Co-Ti-Ba-O proposed by Van den Boomgaard.[13] Scanning electron microscopy (SEM) studies show an interesting pattern that consists of a nearly periodic nanostructure, with isolated nanoplates morphological features, see Fig. 5.2. The corresponding nanometer scale transmission electron microscopy (TEM) images (Fig. 5.3) display two types of contrast. Figure 5.3a displays the low magnification TEM contrast whose periodicity is identical to that of the nanolamellae seen in Fig. 5.3b. Figure 5.3b exhibits a periodic arrangement of layers with an average spacing of 2nm. It will be seen that the layers consist alternatingly of CFO and BTO. The BTO layers contain a stacking fault visible as a dark center line. It represents a hexagonal stacking fault in the 3 unit BTO cell layer. The Rietvield analysis of the Xray data, indicates the presence of 50%CFO, 25% cubic and 25% hexagonal BTO, i.e. a 50/50 mixture of cubic and hexagonal BTO. This apparent oddity is resolved by the stacking fault in the BTO layer; since the BTO lamella contains only three lattice units the hexagonal fault occupies 50% of its volume. The Xray data also indicate a c/a ratio of the hexagonal portion of 2.4 in agreement with known data.[185]

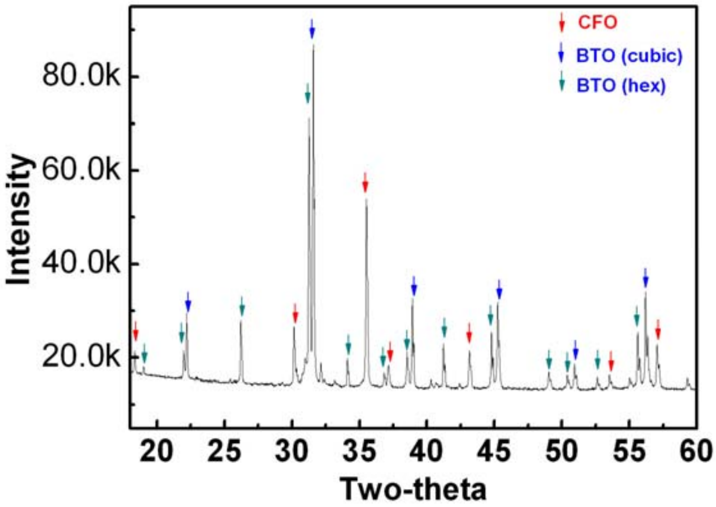

Figure 5.1, Xray diffraction of BTO-CFO compound crystal.

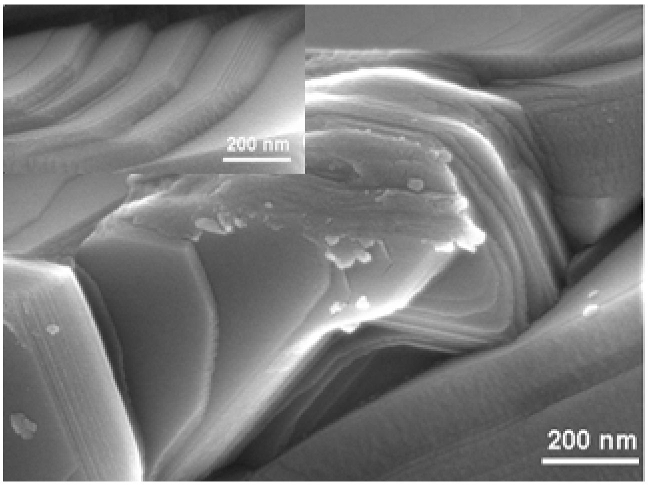

Figure 5. 2, Conventional SEM images of BTO-CFO compound crystal.

Examples of HRTEM images and their corresponding diffraction patterns are shown in Fig 5.3c for representative 50%CFO/50%BTO crystals. TEM images taken at higher resolution (HRTEM, Fig 5.3b) show details of the lamellar structure. Clear lattice fringes with d_{110}= 0.29 nm / d_{220}= 0.296 nm reveal that well-crystallized BTO/CFO is formed. The measured unit supercell is consistent with the periodicities measured from the diffraction pattern (where a_p= 0.4105 nm is the lattice parameter of cubic perovskite and a_s= 0.8391 nm that of spinel). Further confirmation of the phase separation is seen in the elemental mapping imaged at high resolution by TEM. The elemental mapping line scan perpendicular to the interface show the phase separation between BTO and CFO phases. Selected area electron diffraction pattern (SAED) of the superlattice taken along the <111> zone axis (see inset of Fig. 5.3c) indicates the formation of the crystalline cubic phases. Materials studio simulations of the boundary region gave optimum matching for a simple $3a_p$ perovskite and $2a_s$ spinel 1D supercell (Fig. 5.3d), $a_{p,s}$ are the Perovskite and Spinel lattice parameters, which together represent a single period of the BTO-CFO bi-crystal oriented perpendicularly to the <111> axis. This arrangement also agrees with the stoichiometry of the sample. The low- and high resolution TEM images and compositional data in their entirety thus suggest that the lamellar nanostructure consists of three faulted unit cells perovskite BTO and two unit cells spinel CFO meaning, equivalently, that nanometer-scale phase separation has occurred. It is accommodated by low energy (1-10) interface. The oxygen octahedra at the BTO/CFO interfaces are hexagonally arranged and some oxygen octahedra overlap, i.e. the interface is corrugated, see Fig. 5.3d.

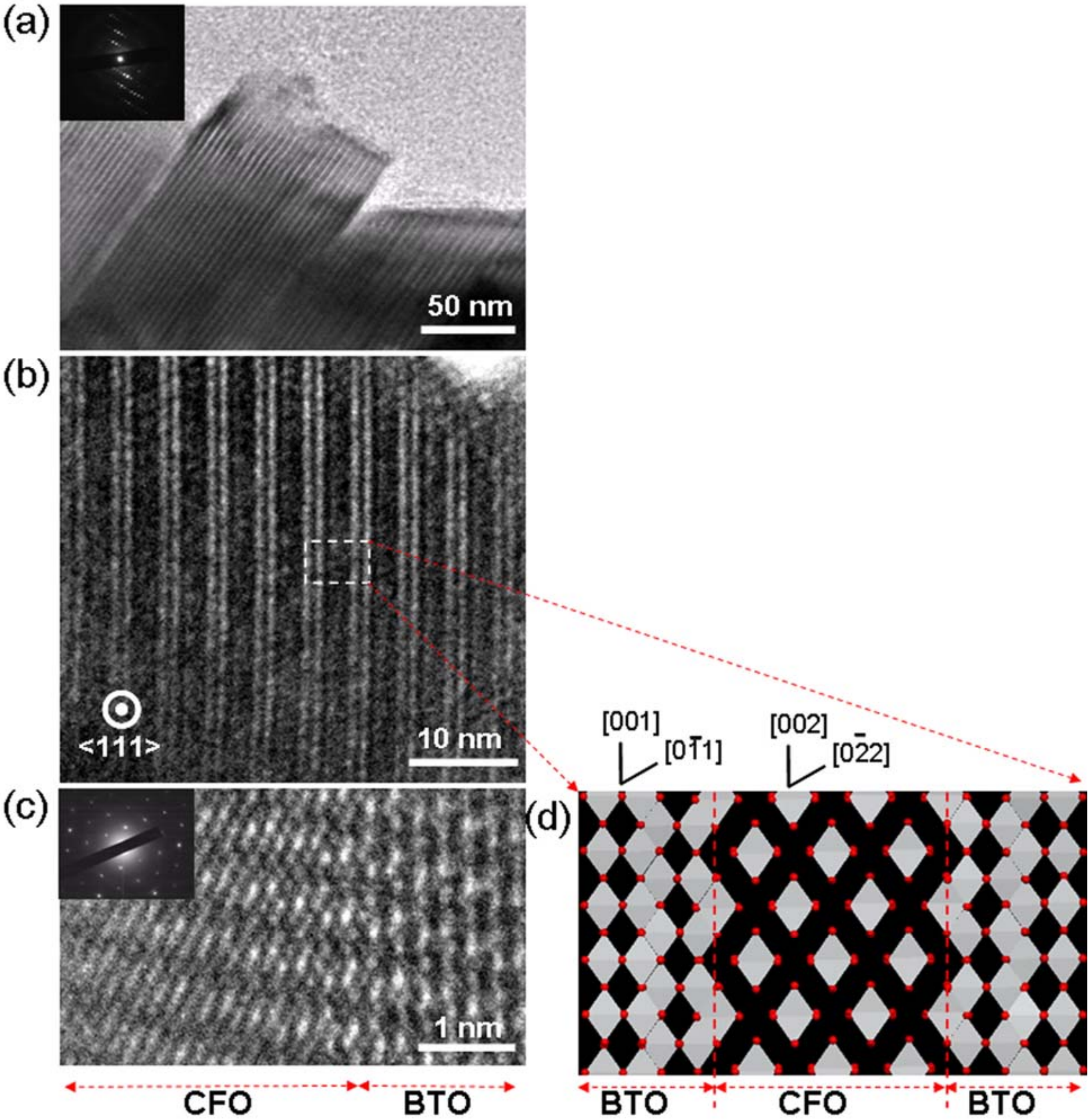

Figure 5.3. TEM images of nanostructure morphologies. (a) Low magnification image including a selected area electron diffraction pattern demonstrating the long coherence length of the periodic structure. (b) Conventional image; the dark and bright areas are CFO and BTO lamellae, respectively and the dark center line in the bright stripes is the image of a stacking fault. (c) [111] zone HRTEM images showing the atomic structure of each layer of the bicrystal. (d) Schematic diagram of the in-plane image corresponding to the common <111> zone axis. It shows the stacking fault in the BTO portion and the corrugated interface at which oxygen octahedra "belonging" to CFO and BTO overlap.

It is known that the decomposition of an amorphous or nanocrystalline CFO/BTO solid solution in a magnetic field results in a periodic nanostructure reminiscent of a spinodal decomposition into two cubic phases. The present decomposition at high temperatures likely occurs via a pseudo-spinodal process[186] during which a periodic structure of cubic CFO and hexagonal BTO[187] is formed first. The stacking fault then represents the remainder of the hexagonal phase after it transformed to the low temperature cubic modification under constraint upon cooling. The resulting epitaxial stress in $CoFe_2O_4$, $\sigma_{110}^{CFO} = Y^{CFO}\varepsilon_{110}^{epi}$, $\varepsilon_{110}^{epi} = \frac{d_{220}^{CFO} - d_{110}^{BTO}}{\frac{1}{2}\left(d_{220}^{CFO} + d_{110}^{BTO}\right)}$ whereas the stored epitaxial elastic energy $U_{111} = \frac{1}{2}\left(\varepsilon_{110}^{epi}\right)^2 Y^{CFO/BTO}$. The quantity $Y^{CFO/BTO}$ is the shear modulus of the CFO/BTO parallel composite. With the values Y^{BTO}= 67 GPa[188] and Y^{CFO}= 141.6 GPa,[189] U_{111}= $4.7*10^6$ J/m^3. This elastic energy is significantly lower than U_{100}= $2.7*10^7$ J/m^3 observed in PLD thin films of the same system, which explains the spontaneous formation of the present composite. The small epitaxial strain also leads to a small magnetoelastic energy density of $CoFe_2O_4$, $U_{mel} = \frac{\lambda_{100}^{CFO} + 3\lambda_{111}^{CFO}}{4}\varepsilon_{110}^{epi}Y^{CFO}$ = $-1.67*10^5 Jm^{-3}$. The λ's represent the magnetostriction coefficients of CFO.[189]

5. 3 Ferroelectric Properties of $BaTiO_3$-$CoFe_2O_4$ Nanostructures

The ferroelectric properties of the BTO/CFO 2D nano-superlattice are equally interesting. Normally, BTO is a typical ferroelectric crystal. However, according to the temperature and frequency dependencies of the dielectric constant ε_r and loss factor, see figure 5.4, as part of the present composite it is a relaxor ferroelectric[190, 191] characterized by a Vogel-Fulcher temperature T_{VF}= 311 K. The dielectric response depends on the external magnetic field as shown clearly in Figs. 5.4c and 5.4d. Note that, for example, the relative dielectric constant at f = 21.5 Hz equals 2250 but decreases to 800 if a field of 100 Oe is applied. Information about the nature of the clusters,[192,193] thought to cause relaxor behavior, can be extracted from the activation enthalpy of the Vogel-Fulcher relationship, $\ln\left(\frac{f}{f_0}\right)=\frac{\Delta H}{k\left(T_m - T_{vf} - T_h\right)}$ shown in the insert of Fig. 5.4d. It is a magnetoelastic energy density $\Delta H_{mel}=T_h k$=8Kk from which it follows that the extent of the cluster equals approximately one perovskite lattice constant. It may thus be argued that the relaxation occurs at the CFO/BTO interface.

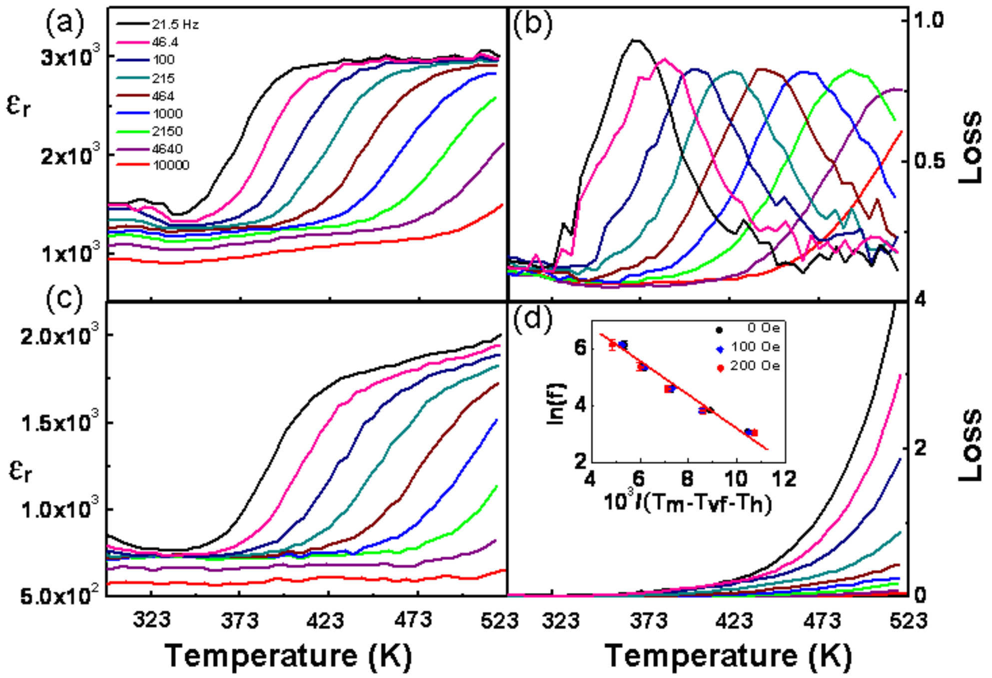

Figure 5.4. Dielectric constant and loss factor of BTO-CFO compound crystal. (a-b) dielectric constant and loss factor versus temperature measured at various frequencies (from left to right: 21.5 Hz, 46.4 Hz, 100 Hz, 215 Hz, 464 Hz, 1000 Hz, 2150 Hz, 4640 Hz, 10 kHz). (c-d) dielectric constant and loss factor versus temperature subjected to an external magnetic field of 100 Oe. The inset of image d demonstrate linear variation of 10^3 (T_m-T_{vf}) as a function of ln(f) validating the Vogel-Fulcher relationship under different magnetic fields: 0 Oe, 100 Oe and 200 Oe.

5. 4 Magnetic Properties of $BaTiO_3$-$CoFe_2O_4$ Nanostructures

The zero room temperature ferromagnetic remanence of the superlattice shown in Fig. 5.6a can be understood if it is assumed that in zero field neighboring CFO layers are antiferromagnetically coupled through their dipolar interaction. This assumption is indirectly supported by Lorentz TEM observations (see Fig 5.5), which did not show any indication of domain walls. Therefore, the initial steep rise of the magnetization is determined by the magnetization rotation in the CFO sheet plane. It's susceptibility, χ, will be determined by the balance of the anisotropy energy density of CFO and the magnetoelastic energy density evaluated above, $\chi = \frac{\left(M_s^{CFO}\right)^2}{2\left(K^{CFO} + U_{mel}\right)}$. Since $K^{CFO}=2*10^5 Jm^{-3}$ [194] and $U_{mel}=-1.7*10^5\ Jm^{-3}$ (see above) the susceptibility is much larger than that of unconstrained single crystalline CFO. The approach to saturation of the sheets is governed by the demagnetization field $\frac{K^{CFO} + U_{mel} + \left(M_s^{CFO}\right)^2}{M_s^{CFO}}$, [195] i.e. saturation would be achieved much more gradually as the magnetization components now rotate against the demagnetization field. The normalized plot of the experimental data confirms these expectations, see Fig 5.6 a.

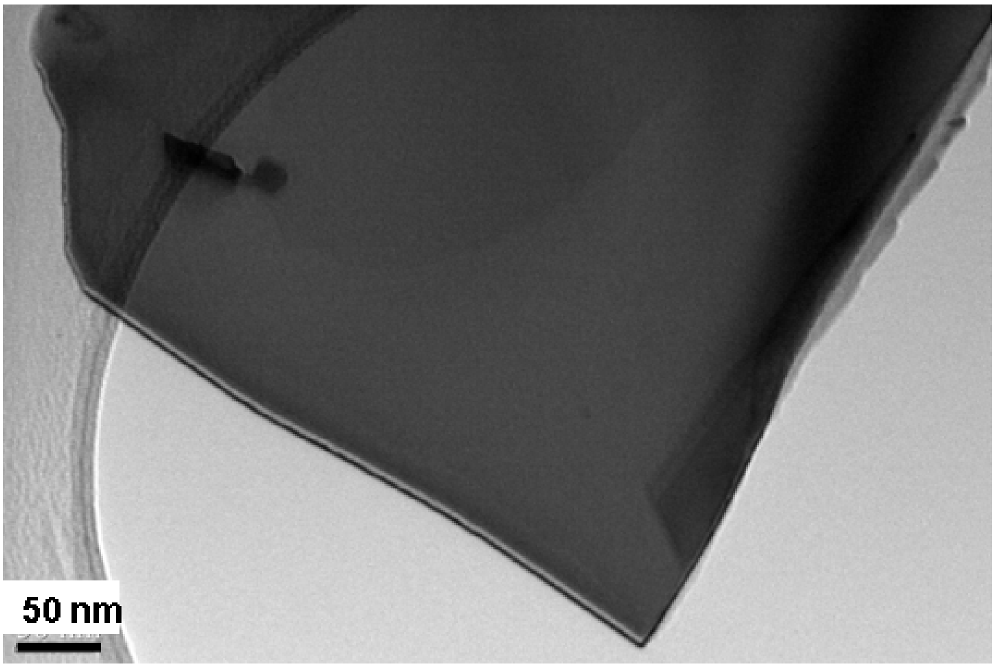

Figure 5.5. Lorentz TEM of BTO-CFO bicrystal

5. 5 Magnetoelectric Coupling of $BaTiO_3$-$CoFe_2O_4$ Nanostructures

The CFO/BTO nano-bicrystal is naturally magnetoelectric at room temperature as the components' critical temperatures are higher than it. The magnetoelectric coupling constant displays a maximum of α_{ME}=20mV/cm*Oe at an extremely small dc bias magnetic field of 10 Oe. This constant is larger than those displayed by any natural magnetoelectric crystal. The inset of Fig. 5.6a displays the field dependence of the coupling constant. The electric field induced polarization (P-E) behavior is shown in Fig. 5.6b. The BTO-CFO compound exhibits well saturated hysteresis loops with a remanent polarization (Pr) and the coercive field (Ec) of about 11 $\mu C/cm^2$ and 1 kV/cm, respectively. The observed Pr value is higher than the reported value of polycrystalline BTO ceramics.[196]

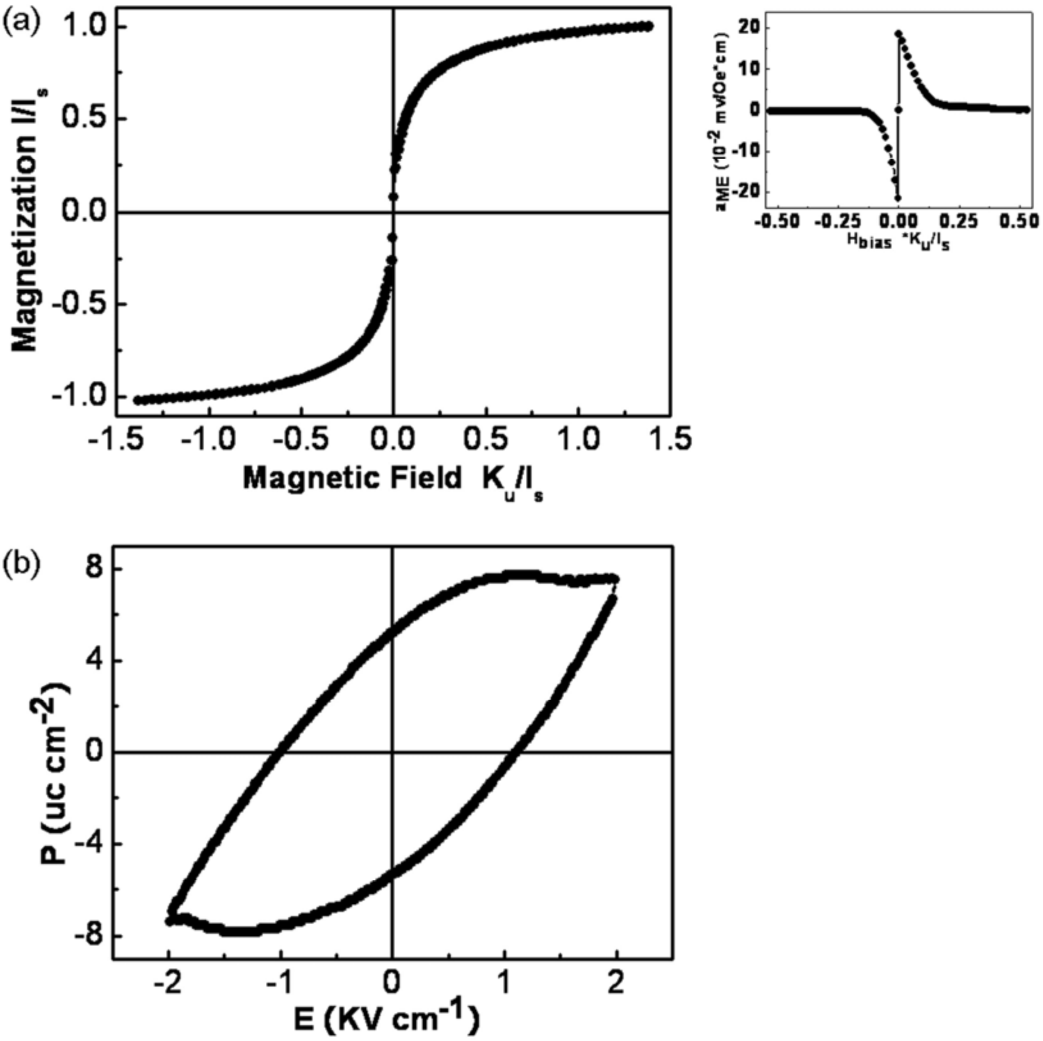

Figure 5.6. Magnetic and electric properties of BTO-CFO compound crystal. (a) magnetic hysteresis loop of BTO-CFO. The right-bottom inset shows the magnetoelectric α_{ME} -dependent variation of the external magnetic field (the bias AC field, 10 Oe). An example of the frequency dependent *M-E* coupling coefficient $\alpha = \partial E/\partial H$ is calculated from the *M-E* output voltage. (b) Polarization loop of the BTO-CFO compound crystal sample at room temperature.

5. 6 Conclusion

Periodicities with the level of perfection we report here have not, to our knowledge, ever been observed in multiferroic perovskite-spinel self-assembled nanostructures. The {111} orientation appears to provide the lowest energy interfacial configurations for spinel-perovskite systems. The coexistence of relaxor ferroelectricity and magnetic order[197] has attracted considerable attention due to their peculiar properties and various applications. [198, 199] We have already shown that within one homologous solid solution, the periodic phase separated perovskite-spinel superlattice can be synthesized. By varying the compositional ratio and introducing chemical substitutes, it should be possible to improve on one or more of the many technologically important functionalities in the combined perovskite and spinel families.

Chapter 6

Summary and Future Work

This dissertation presents a novel self assembly "bottom-up" nanofabrication approach as a general protocol to creating multiferroic nanostructures in a controlled manner. We have conducted a systematic study of such bottom up multiferroic nanostructures by using solid state phase transformation and block copolymer self assembly. The multifunctional nanostructures through bottom up assembly are significant due to their intrinsic scientific value, as well as their potential applications in a wide variety of fields, such as nanolithography for high density storage nanofabrication, nanophotonics, and electronics.

For the solid state phase transformation of "bottom-up":

1, Pseudo-spinodal decomposition mechanism was used to synthesize multiferroic PZT/$NiFe_2O_4$ nanocomposite. Vertical multilamellae nanostructures were produced by crystallizing and decomposing a gel in a magnetic field below the Curie temperature of $NiFe_2O_4$. The decomposition wavelength of the PZT/NFO alternation, 25 nm, agrees within a factor of two with the theoretically estimated value. This wavelength significantly affects the total accumulated charge during ME coupling measurement.

2, The macroscopic ferromagnetic, -electric and magnetoelectric coupling responses correspond qualitatively and semi-quantitatively to the features of the nanostructure. The maximum of the field dependent magnetoelectric susceptibility equals 1.8 V/cm Oe.

3, We successfully extend this technique to the synthesis of a magnetoelectric bi-crystal system. This is the first time to report on a spontaneously phase separated nanolamellae perovskite-spinel $BaTiO_3$-$CoFe_2O_4$ superlattice with a corrugated interface. Epitaxy is achieved by interlacing the two structures over the extent of one oxygen octahedron.

4, The superlattice is magnetoelectric with a frequency dependent coupling coefficient of maximally 20mV/Oe cm. The $BaTiO_3$ component is a ferroelectric relaxor with a Vogel-Fulcher temperature of 311 K. Since the material can be produced by standard ceramic processing methods, the discovery represents great potential for magnetoelectric devices.

For the block copolymer self assembly of "bottom-up":

1, We studied the interplay between the self assembly of block copolymer and sol-gel chemistry to produce multiferroic nanostructures with tunable morphologies and spacings. Two types of multifunctional nanostructures were synthesized: (i) the hexagonally ordered $CoFe_2O_4$ nanopillar arrays embedded in a PZT matrix; (ii) the vertical alternative layers between $CoFe_2O_4$ and PZT components.

2, The hexagonally ordered CFO nanopillars are antiferromagnetic coupled, which has been corroborated by MFM. It has been demonstrated that the application of an electric field changes the initial magnetic permeability of the composite by 500% equivalent to ME_H=10V/A. This coupling can be understood in terms of the composites' geometric configuration and its stress free state.

3, Another example of block copolymer based templating is the lamellar structure annealed in a magnetic field. The resulting onion-like nanostructure is superparamagnetic in the gel state and magnetoelectric in the crystallized state. This method has initiated a new route to creating magnetic toroids. Electric field assisted self assembly allows the vertical multilamellae to line up and long range order. This has been attributed to the dielectric difference of alternative layers between PZT and CFO phases.

More generally, we have shown that block copolymer lithography with sol-gel precursors can be used to fabricate nanoscale patterns with different morphologies while preserving the multifunctional properties of the thin film. We created similar nanostructures in other spinel-perovskite systems, such as $BaTiO_3$-$CoFe_2O_4$, PZT-$CoFe_2O_4$, and PZT-$NiFe_2O_4$ etc. Thus, this work opens scenarios in both the nanostructure formation of complex oxides and the characterization of multiferroic nanostructures with tunable magnetic and electric properties.

Further work can be carried out in two areas: the growth of the long range ordered nanostructures and their coupling properties.

1. While it would have been desirable to form a hexagonally ordered array of magnetic nanopillars and study magnetic properties, much information has already been obtained from the short range ordered sample. A perfectly ordered sample could be fabricated by utilizing faceted surfaces of commercially available miscut silicon wafers to guide the self-assembly of block copolymer microdomains into oriented arrays with long-range crystalline order over large wafer surfaces.
2. The behavior of the block copolymer with multiferroic sol-gel precursors needs to be further examined as it is a very interesting case. Small angle neutron scattering (SANS) studies of the ordering of as-spun films accompanied with

simulation might provide insight into the electric and magnetic precursors that affect the ordering. More importantly, there is much interesting science to be explored in the combination of block copolymer and sol gel chemistry.

3. Additionally, the simple ceramic processing should be explored so that device-grade magnetoelectric material may be generated. In this dissertation, we have demonstrated the ferroelectric relaxor magnetic $BaTiO_3$-$CoFe_2O_4$ bi-crystal. However, it is still a challenge to grow well-controlled complex oxides for magnetoelectric bi-relaxors. The starting point could be a systematic study of different perovskite-spinel systems. In order to choose a suitable system, a variety of factors should be considered, such as the molar ratio and relative lattice unit size of the two phases, lattice mismatch of the two phases with each other, elastic moduli, the solubility between the two components, etc.

Chapter 7

Appendix: Experimental Technique

To synthesize the films investigated in the work, Chemical Solution Deposition (Sol-Gel & Spin-Coating) was used. X-ray diffraction (XRD) and transmission electron microscopy (TEM) were used for structural analysis. Atomic force microscopy (AFM) and Environmental secondary electron microscopy (ESEM) were used to investigate surface morphology such as roughness and/or grain size. Scanning electron microscopy (SEM) and transmission electron microscopy (TEM) were used to study nanostructure and chemical composition. The magnetic properties were measured using a vibrating sample magnetometer (VSM), Magnetic force microscopy (MFM), and a superconducting quantum interference device (SQUID). The electrical properties were measured using an RT6000 test system, TA Instruments DEA 2970 and HP 4192 impedance/gain analyzer.

7.1 Sol-Gel and Chemical Solution Deposition

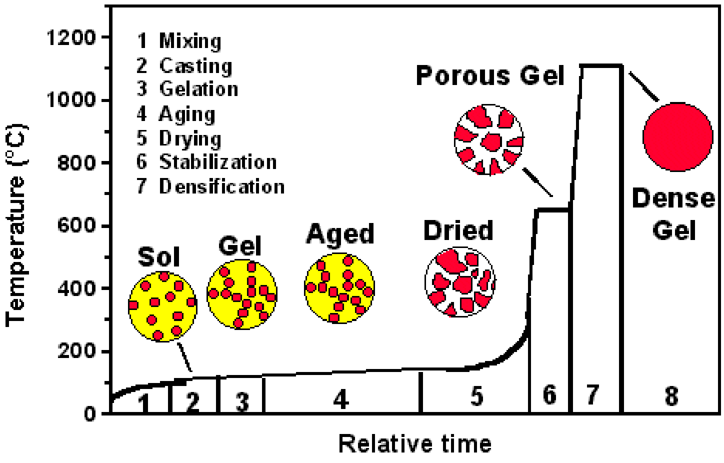

Figure 7.1. Process of sol gel method according to Brinker[200]

The sol-gel method[201, 202, 203] shown in Fig 7.1 is a synthetic process that allows the production of ceramic materials through the formation of a *sol* starting from a solution of precursors, the condensation of the *sol* in a *gel*, and finally the removal of the solvent. The sol can be produced starting both from organic or inorganic precursors, and the whole process is conducted at room temperature. The distinctive thing is that the solid state can be reached at a low temperature starting from a solution, and this fact expands greatly the possibility to prepare new materials or to improve their properties. It becomes possible to synthesize materials under conditions that are not possible in the usual preparation of metal oxides where high temperatures are required. Applying the sol-gel process, it is possible to fabricate ceramic materials in a wide variety of forms: ultra-fine or spherical shaped powders, thin film coatings, ceramic fibers and microporous inorganic membranes.

A sol is defined as a colloidal suspension in a liquid of solid particles, which dimensions, in the range of 1-1000 nm, are small enough to ignore the gravity force. In this way the interaction between the particles are dominated by short-range forces (i.e. Van der Waals and superficial charges).

A gel can be defined as a continuous solid structure that contains a continuous liquid phase. A gel can also be described as a macromolecule formed by all the monomers initially present in solution, which also contains part of the solution itself.

Any of these stages has a large influence on the properties of the resulting material and the great number of variables involved makes the control of the whole process still very practical. Therefore a detailed knowledge of the chemical mechanisms, which permits to control the properties of the final amorphous material at a molecular scale and to synthesize defined structures, is a great challenge for the material scientists. An overview of the sol-gel process is presented in a simple graphic work as below in Fig.7.2.

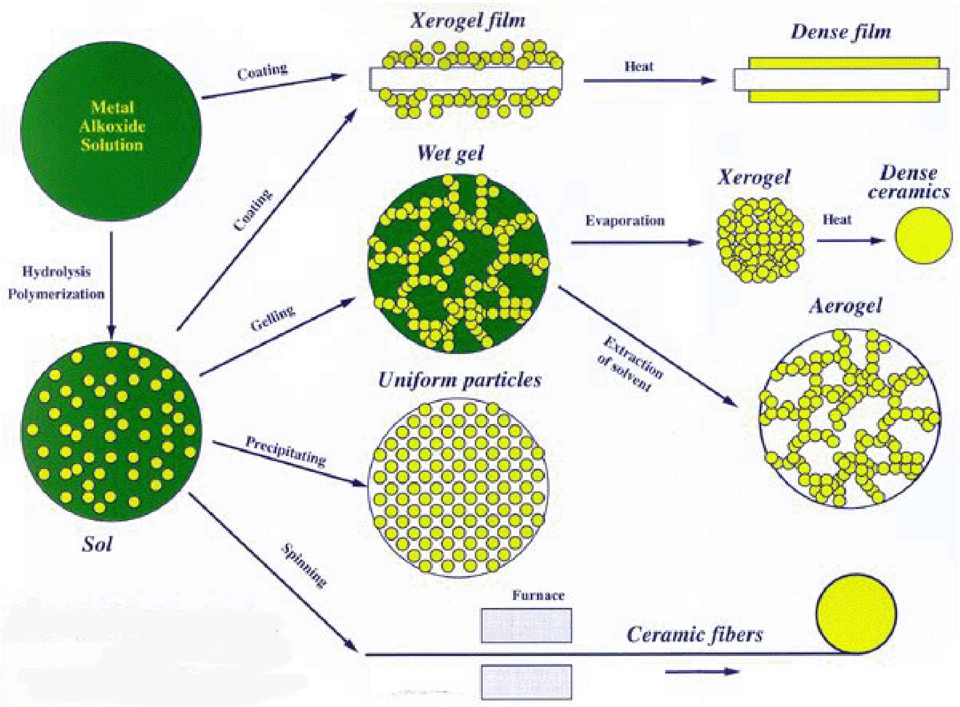

Figure 7. 2 Sol-gel process, different routes possible to synthesize solid materials [204]

Film Deposition – Spin Coating

Films on substrates are easily deposited using the sol-gel technique. Three methods are usually employed: dip coating, spin coating and spraying. The difference between them lies mainly in the different technical arrangement used to deposit a fluid layer of the solution of the precursor on the substrates surface. The technique chosen in this work, because of its operational simplicity is the spin coating technique, which will be further described on this paragraph.

Spin coating involves the acceleration of a liquid puddle on a rotating substrate. The coating material is deposited in the center of the substrate by a robotic arm. The physics behind spin coating involve a balance between centrifugal forces controlled by spin speed and viscous forces which are determined by solvent viscosity. Some variable process parameters involved in spin coating are:

- Solution viscosity
- Solid content
- Angular speed
- Spin Time

The film-forming process is primarily driven by two independent parameters – viscosity and spin speed. The range of film thicknesses easily achieved by spin coating is 50-200 nm. For thicker films, high material viscosity, low spin speed, and a short spin time are needed. However, these parameters can affect the uniformity of the coat. Multiple coatings are preferred for a film thickness greater than 2 micron.

The spin coating technique consists of four basic stages[205] shown in Fig.7.3:

1. The solution is dispensed onto the wafer
2. The solution is spread across the wafer (by spinning)
3. The wafer is then spun at a higher speed (2000-4000 rpm)

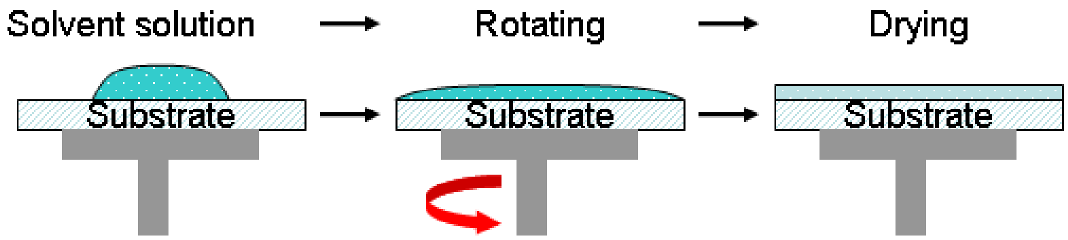

Figure 7.3 Schematic drawing of spin coating process

The technological applications of the sol-gel technique range in a very wide field, because of the versatility and simplicity of the method. The possible applications derive from the various shapes that can be obtained from the gel state and from the compositional and microstructural control of the process, combined with the low processing temperature.

Compared to other techniques, the sol-gel method has the advantages of a good control of the starting material and of the processing parameters, a high purity of the materials, the low temperature of the process and the homogeneity of the product due to the possibility to control the starting solution.

Our research lies in using sol-gel technology to make the self-assembled magnetoelectric thin film nanostructures. There are many advantages including

1) Better homogeneity compared to traditional physical deposition technology;
2) Lower temperature processing and consolidation;
3) More uniform phase distribution in ME composites;
4) Better size and morphological control.

7. 2 Structure Characterization

The structure of the thin films was characterized using scanning x-ray microdiffraction (D8 DISCOVER with GADDS for combinatorial screening by Bruker-AXS). Transmission electron microscopy (TEM) images and microbeam diffraction patterns of the films were obtained with a JEOL 4000-FX TEM operated at an accelerating voltage of 300 KV and JEOL 2100F emission TEM operated at an accelerating voltage of 200 KV that also featured an energy dispersive (chemical) spectroscopy (EDS) attachment. The surface topography was investigated using atomic force microscopy (AFM) in tapping mode using standard silicon cantilevers (Dimension 3100, Digital Instruments). Magnetic force microscopy (MFM) in lift mode was used to characterize the magnetic domain structure of the crystallized thin-film structure

7.2.1 X-Ray Diffraction

The diffraction of X-rays by matter results from the combination of two different phenomena: (a) scattering by each individual atom, and (b) interference between the waves scattered by these atoms. This interference occurs because the waves scattered by the individual atoms are coherent with the incident wave, and therefore between themselves.

X-ray diffraction characterization of the films in this dissertation was conducted by using Cu K_α radiation in a scanning x-ray microdiffraction (D8 DISCOVER with GADDS for combinatorial screening by Bruker-AXS). The scanning of the 2θ angle was started at 15°, and ended at 60°. The scanning rate was 0.5°/min.

7.2.2 Transmission Electron Microscopy

A TEM operates similarly to an optical microscope, except optical microscopes use light sources and focus light beams with glass lenses, while TEMs use electron sources and focus electron beams with electromagnetic lenses. The electrons emitted from the filament are accelerated by a high voltage (100 kV – 1000 kV) and focused through a set of condenser lenses (electromagnetic lenses) onto the specimen. The electron beam is scattered by the specimen. The diffracted beams are then brought to focus by the objective lens on its back focal plane and form a diffraction pattern. A final TEM image or diffraction pattern can be produced on the fluorescent viewing screen by a series of objective lens, intermediate lens and projector lens. The three main imaging and diffraction techniques used in this study include: 1. conventional imaging (bright-field and dark-field TEM); 2. electron diffraction (selected area electron diffraction, SAD); 3. phase-contrast imaging (high-resolution TEM, HRTEM). Besides diffraction and spatial imaging, the high-energy electrons in TEM cause electronic excitations of the atoms in the specimen. Two important spectroscopic techniques make use of these excitations, i.e. energy-dispersive x-ray spectroscopy (EDS) and electron energy-loss spectroscopy (EELS).

The samples for TEM were prepared using conventional slicing, grinding, and polishing followed by ion thinning until performation in a Gatan Precision Polishing System (PIPS) operated at 5 kV and an angle of 5°. The samples were examined in a JEOL 2100F field emission TEM and a JEOL 2100 LaB6 TEM operated at 200 KV. In this dissertation, the conventional bright-field and dark-field imaging, SAD, HRTEM and EDS are used to study the microstructures of the films.

7.2.3 Atomic Force Microscopy (AFM)

The atomic force microscope is one type of scanned-proximity probe microscopes which is used to measure various local properties of the sample, such as height, optical absorption, or magnetism.[206, 207, 208] AFM system consists of a tube scanner, a position-sensitive photo-detector, and a cantilever with a probe located at the free end. There are numerous modes which are designed for specific measurements including magnetic force mode (MFM), which was used to study magnetic domain information of this study. Lift mode for MFM was used in this study to perform magnetic domain measurements.

MFM is a variation of the Atomic Force Microscope (AFM), which is used to map out magnetic domains in the sample. The mode of operation is essentially noncontact imaging. Similar with an AFM, a sharp magnetized probe is attached to the bottom of a cantilever. The magnetic probe used in this study is standard silicon cantilever (or silicon nitride cantilever) coated with a magnetic thin film. The interaction of the tip with various magnetic domains in the sample results in cantilever deflection. The detector can sense the deflection of the cantilever, which will result in a force image in a static mode. Alternatively, it can detect the resonance frequency change of the cantilever, which will result in a force gradient image. The force gradient (F′) detected contains information from both the surface structure and surface magnetization:

$$F' = F'_{surface} + F'_{magnetic} \qquad (7.1)$$

where F'_{surface} is the surface component of the gradient and F'_{magnetic} is a magnetic component of the gradient. Signals from surface topography dominate at a distance close to the surface while, at a distance further away from the surface (typically beyond 100 nm), the magnetic signal dominates.

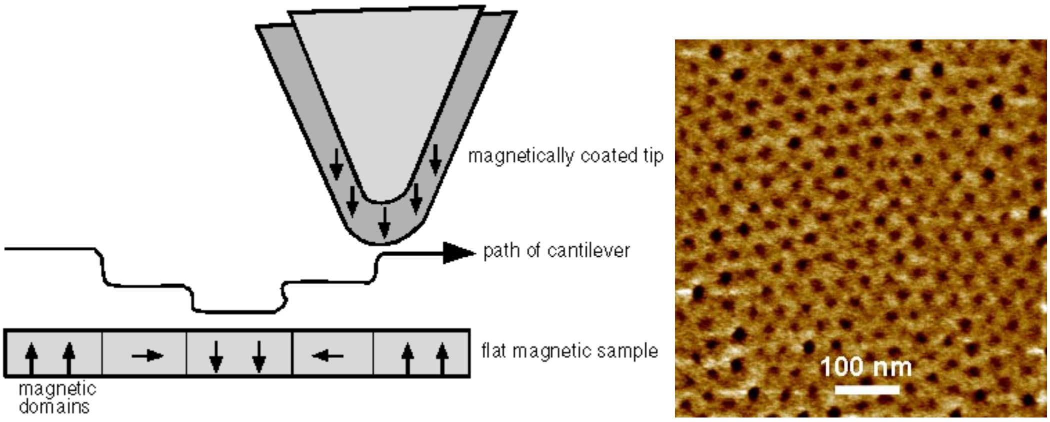

Figure 7.4 MFM maps the magnetic domains of the sample surface.[209]

7.3 Electric Measurement

Ferroelectric measurements (including hysteresis loop, pulsed polarization, polarization retention and fatigue, and resistivity) were conducted using a commercial RT66 test system (Radiant Technologies). Fig. 7.5A shows the picture of the electric set up used in this study. It consists of an Analog Data Precision model 2020 programmable pulse generator, load resistance and oscilloscope with an internal impedance of 50Ω. A series of square bipolar pulses train is generated and traverses to the test ferroelectric capacitor. The pulse sequence shown in is called PUND pulse series.[210] Polarization hysteresis loops were obtained for each test capacitor.

Figure 7.5. A picture of ferroelectric polarization measurement set-up at UMD.

DEA measures dielectric properties as a function of temperature, frequency and time. Dielectric properties define the capacity and conductivity of material. Capacitive properties determine the ability of the material to store electric charge. Conductive properties are proportional to the ability of charges to move in the material. Dielectric analyzer (DEA 2970) was used to measure dielectric properties of the sample in this dissertation.

7.4 Magnetic Measurement

Magnetic analyses of the thin films were done using a vibrating sample magnetometer (VSM), and a superconductive quantum interference device (SQUID). The M-H hysteresis loop and the temperature dependence of the saturation magnetization were all characterized using these instruments.

7.4.1 Vibration Sample Magnetometer

The VSM measurement is based on Faraday's law, which states that an emf will be generated in a coil when there is a change in the flux going through the coil. For a coil with n turns of cross-sectional area, the emf (V) is related to dt/ dB, given as

$$V = -na\ dB/ dt. \qquad (7.2)$$

Since $\Delta B=\mu_0 M$, when we place a magnetic sample into the coil, this relationship becomes

$$V = -\mu_0\ M\ na\ /\ dt. \qquad (7.3)$$

A typical VSM setup is illustrated in Figure 7.6.[211] It has a pair of electromagnets that generate a DC magnetic field, and a pick-up coil that acquires the sample signals. When a sample has a net magnetization, it produces magnetic flux in its vicinity. During VSM measurements, the sample is mechanically vibrated (up and down) at a fixed frequency. This vibration produces a flux change, which creats an AC voltage proportional to the magnetic moment of the sample in the pick-up coil. A lock-in amplifier is then used to measure the voltage. The AC signal is proportional to the frequency and amplitude of the sinusoidal motion and the total magnetic moment of the sample at that applied magnetic field.

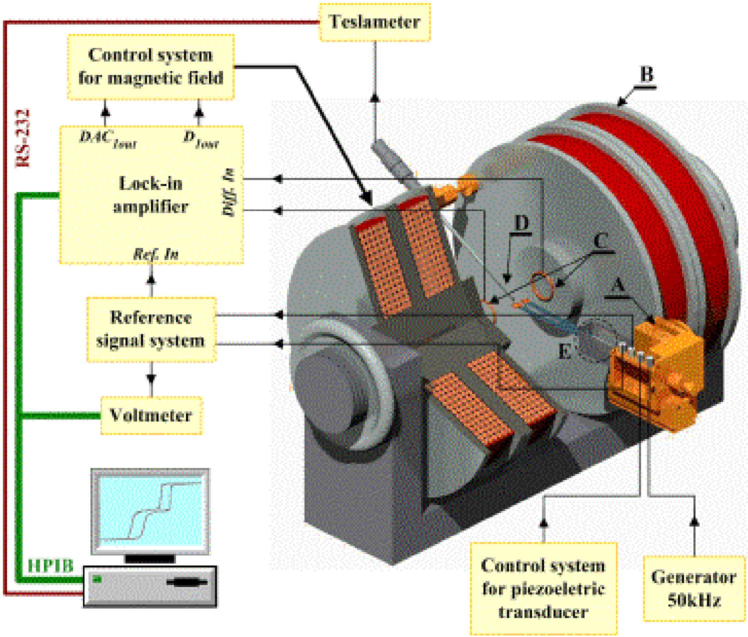

Figure 7.6 Schematic diagram of VSM.

The frequency and amplitude of the sinusoidal motion are held constant, which is controlled by a capacitor (reference signal generator). By feeding the signals from the pick-up coils and the reference signal into a demodulator, the magnetic moment of the sample is extracted. The magnetic moment determined by VSM is given in terms of the basic electromagnetic unit (or, emu), which can be related to the magnetization, susceptibility, and Bohr magnetron. VSM provides a fast and easy way for measuring the magnetic properties of materials. However, it does have a few drawbacks. These include (i) the resolution of VSM is ~10-5 emu, which is insufficient for thin film samples or sample with low intrinsic magnetization, i.e., canted antiferromagnetic or ferrimagnetic materials; and (ii) most VSMs do not have low temperature capability.

7.4.2 Superconducting Quantum Interference Device Magnetometer

The SQUID uses the properties of electron-pair wave coherence and Josephson Junctions to detect very small magnetic fields. A SQUID consists of a Josephson junctions which have two superconductors separated by a thin insulating layer and acts as a flux-to-voltage transducer (schematically shown in Fig. 7.7).

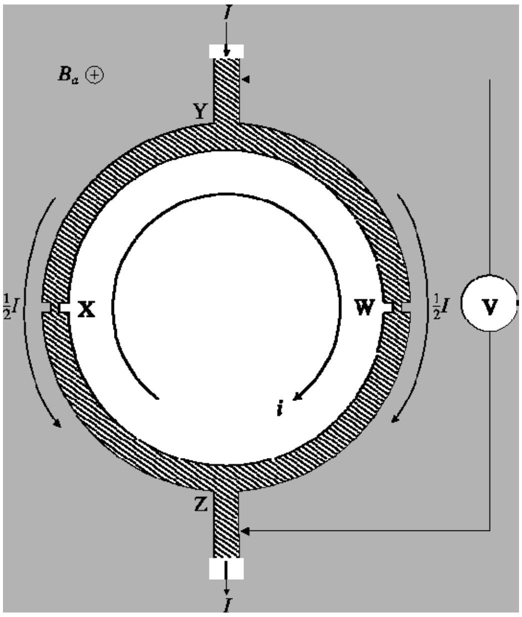

Figure 7.7 Schematic of a SQUID system.

7.5 Magnetoelectric Measurement

The magnetoelectric effect is defined as a coupled two-field effect, in which an application of a magnetic field induces an electrical polarization. This is called “magnetically” induced magnetoelectric effect and denoted by ME_H. The effect in which an application of electrical induces a magnetization is called “electrically” induced magnetoelectric effect and denoted by ME_E.

ME_H Effect:

The experimental set-up is depicted in Figure 7.8. The magnetic field was applied by an electromagnet and the intensity of the field was measured by using a Hall probe. The piezoelectric charge was measured using a KEITHLEY 614 electrometer that allows measuring small charge of the order of a few pico coulombs.

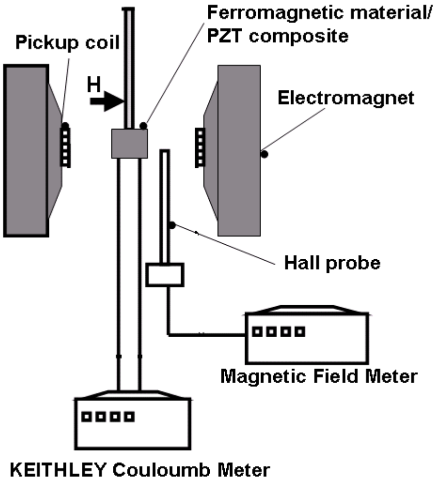

Figure 7.8 Experimental setup for ME_H effect

ME_E effect

Figure 7.9 shows the experimental setup. The magnetization of the composites was measured by using vibrating sample magnetometer (VSM) in the direction parallel to the bias magnetic field. The samples were mounted with the interface of the composite aligned parallel to the magnetic field. The electric field to the sample was applied with a d.c power supply.

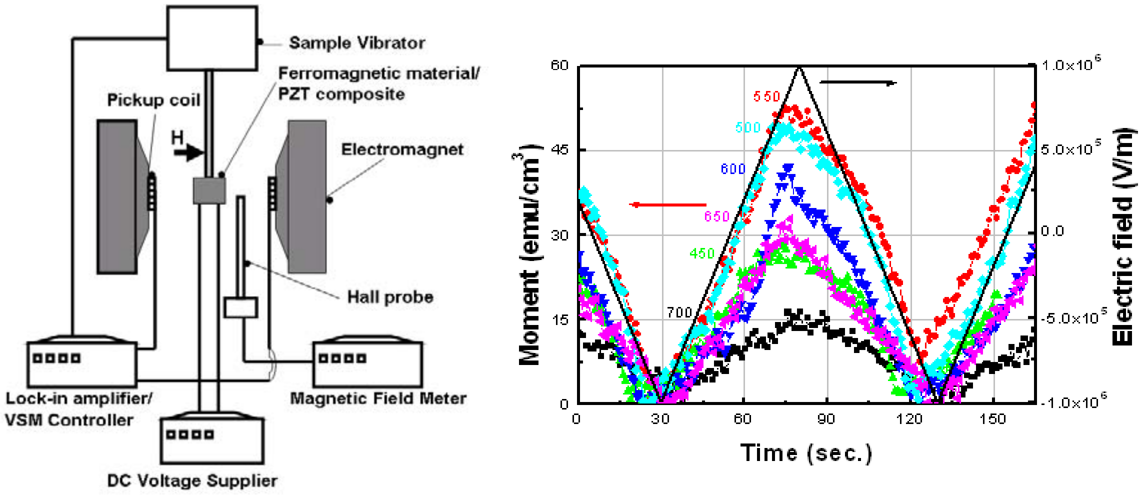

Figure 7.9 Experimental setup for ME_E effect (left) and the experimental data from this measurement (right)

Bibliography

---

[1] Van den Boomgard J, Terrell D R, Born R A J and Giller H F J I, *J. Mater. Sci.* **9** 1705 (1974)

[2] Liz-Marzan, L. M.; Mulvaney, P. *J. Phys. Chem. B*, **107**, 7312 (2003).

[3] Pileni, M. P. *J. Phys. Chem. B*, **105**, 3358 (2001).

[4] Lu, A. H.; Li, W. C.; Kiefer, A.; Schmidt, W.; Bill, E.; Fink, G.; Schuth, F. *J. Am. Chem. Soc.*, **126**, 8616 (2004).

[5] Alexe, M.; Scott, J. F.; Curran, C.; Zakharov, N. D.; Hesse, D.; Pignolet, A. *Appl. Phys. Lett.*, **73**, 1592 (1998)

[6] Bea, H; Gajek, M; Bibes, M, et al. *J Phys. Cond. Matt.* **93**, 669, (2008)

[7] Wood V E and Austin A E, *Int. J. Magn.* **5** 303 (1973)

[8] N.A. Hill, *J. Phys. Chem. B* **104**, 6694 (2000).

[9] Van Suchtelen, J. *Philips Res. Repts,* **27**, 28 (1972)

[10] Tellegen B D H, *Philips Res. Rep.* **3** 81 (1948)

[11] Van Run A M J G, Terrell D R and Scholing J H, *J. Mater. Sci.* **9** 1710 (1974)

[12] Van den Boomgard J, van Run A M J G and van Suchtelen J, *Ferroelectrics* **10** 295 (1976)

[13] Van den Boomgard J and Born R A J, *J. Mater. Sci.* **13** 1538 (1978)

[14] Ryu J, Priya S, Uchino K and Kim H E, *J. Electroceram.* **8** 107 (2002)

[15] Bunget I and Raetchi V, *Rev. Roum. Phys.* **27** 401 (1982)

[16] Mahajan R P, Patankar K K, Patil A N, Chaudhari S C, Ghatge A K and Patil S A, *Indian J. Eng. Mater. Sci.* **7** 203 (2000)

[17] Kothale MB, Patankar K K, Kadam S L, Mathe V L, Rao A V and Chougule B K *Mater. Chem. Phys.* **77** 691 (2003)

[18] Bichurin M I, Petrov V M, Petrov R V, Kiliba Y V, Bukashev F I, Smirnov A Y and Eliseev D N, *Ferroelectrics* **280** 365 (2002)

[19] Kadam S L, Patankar K K, Mathe V L, Kothale M B, Kale R B and Chougule B K *Mater. Chem. Phys.* **78** 684 (2003)

---

[20] Srinivasan G, Rasmussen E T and Hayes R, *Phys. Rev.* B **67** 014418 (2003)

[21] Zhai J Y, Cai N, Liu L, Lin Y H and Nan C W *Mater. Sci. Eng.* B **99** 329 (2003)

[22] Dai Y R, Bao P, Zhu J S, Shen H M, Liu J M and Wang Y N, *Acta Metall. Sin.* **39** 1209 (2003)

[23] Srinivasan G, Rasmussen E T, Bush A A, Kamentsev K E, Meshcheryakov V F and Fetisov Y K, *Appl. Phys.* A **78** 721 (2004)

[24] Engdahl G, Handbook of Giant Magnetoresistive Materials (New York: Academic) (2000)

[25] Ryu J, Carazo A V, Uchino K and Kim H E, *Japan. J. Appl. Phys.* **40** 4948 (2001)

[26] Ryu J H, Priya S, Carazo A V, Uchino K and Kim H E, *J. Am. Ceram. Soc.* **84** 2905 (2001)

[27] Wan J G, Liu J M, Chand H L W, Choy C L, Wang G H and Nan C W, *J. Appl. Phys.* **93** 9916 (2003)

[28] Dong S X, Li J F and Viehland D, *IEEE Trans. Ultrason. Ferroelectr. Frequency Control* **50** 1253 (2003)

[29] Dong S X, Cheng J R, Li J F and Viehland D, *Appl. Phys. Lett.* **83** 4812 (2003)

[30] Dong S X, Li J F and Viehland D, *J. Appl. Phys.* **95** 2625 (2004)

[31] Li J F and Viehland D, *Appl. Phys. Lett.* **84** 4188 (2004)

[32] Zeng M, Wan J G, Wang Y, Yu H, Liu J M, Jiang X P and Nan C W, *J. Appl. Phys.* **95** 8069 (2004)

[33] Dong S X, Li J F and Viehland D, *IEEE Trans. Ultrason. Ferroelectr. Frequency Control* **51** 794 (2004)

[34] Nersessian N, Or S W and Carman G P, *IEEE Trans. Magn.* **40** 2646 (2004)

[35] Dong S X, Li J F and Viehland D, *J. Appl. Phys.* **96** 3382 (2004)

[36] Bayrashev A, Robbins W P and Ziaie B, *Sensors Actuators* A **114** 244 (2004)

[37] Dong S X, Li J F and Viehland D, *Appl. Phys. Lett.* **85** 2307 (2004)

[38] Kuwata J, Uchino K and Nomura S, *Ferroelectrics* **37** 579 (1981)

[39] Kuwata J, Uchino K and Nomura S, *Japan. J. Appl. Phys.* **21** 1298 (1982)

[40] Patankar K K, Nipankar R P, Mathe V L, Mahajan R P and Patil S A, *Ceram. Int.* **27** 853 (2001)

---

[41] Mori K and Wuttig M, *Appl. Phys. Lett.* **81** 100 (2002)

[42] Mathe V L, Patankar K K, Jadhav U V, Patil A N, Lotake S D and Patil S A, *Ceram. Int.* **27** 531 (2001)

[43] Dong S X, Li J F and Viehland D, *Appl. Phys. Lett.* **83** 2265 (2003)

[44] Srinivasan G, Rasmussen E T, Levin B J and Hayes R, *Phys. Rev.* B **65** 134402 (2002)

[45] Shastry S, Srinivasan G, Bichurin M I, Petrov V M and Tatarenko A S, *Phys. Rev.* B **70** 064416 (2004)

[46] Laletsin U, Padubnaya N, Srinivasan G, Devreugd C P, *Appl. Phys.* A **78** 33(2004)

[47] Zhai, J. Dong S. X., Xing Z., Li J. F., and Viehland D., *Appl. Phys. Lett.*, **89**, 083507 (2006)

[48] Zheng H *et al, Science* **303** 661 (2004)

[49] Nan CW, Liu, G., Lin Y., and Chen H., *Phys. Rev. Lett.* **94**, 197203 (2005).

[50] Murugavel P., Padhan P., and Prellier W., *Appl. Phys. Lett.* 85, 4992 (2004)

[51] Singh M. P., Prellier W., Mechin L., Simon C. and Raveau B., *J. Appl. Phys.* **99**, 024105 (2006).

[52] Zhou J. P., He H. C., Shi Z., and Nan C. W., *Appl. Phys. Lett*. **88**, 013111 (2006).

[53] He H. C., Zhou J. P., Wang J., Nan C. W., *Appl. Phys. Lett*. **89**, 052904 (2006).

[54] Ortega N., Bhattacharya P., and Katiyar R. S., *J. Appl. Phys*. **100**, 126105 (2006).

[55] Wan J., *Appl. Phys. Lett.* 86, 202504 (2005)

[56] Zhang J. X., et al, *Appl. Phys. Lett.* **90**, 052909 (2007)

[57] Nan C. W, *Phy. Rev. Lett.* 94, 197203 (2005)

[58] Krupicka S. and Novák P. in *Ferromagnetic Materials*, Wohlfarth E.D., ed., North Holland, Oxford, p. 189, 1982 (1968)

[59] Zheng H., Wang J., Mohaddes-Ardabili L., Wuttig M., Salamanca-Riba L., Schlom D. G., and Ramesh R., *Appl. Phys. Lett.,* **85**, 2035 (2004)

[60] Dale D., Fleet A., Brock J. D. and Suzuki Y., *Appl. Phys. Lett.*, **82**, 3725 *(*2003)

[61] Stein S., Wuttig M., Viehland D., and Quandt E., *J. Appl. Phys.*, **97,**10Q301 (2005)

[62] Chopdekar R.V and Suzuki Y., *Appl. Phys. Lett.*, **89**, 182506 (2006)

[63] http://www.physics.ubc.ca/~stm/

---

[64] Whitesides G M and Grzybowski B, *Science* **295** 2418 (2002)

[65] Brust M and Kiely C J, *Colloids Surf.* A **202** 175 (2002)

[66] Pan Z., Alem N., Sun T. and Dravid V. P., *Nano Letters*, 6, 2344 (2006)

[67] V. A. Shchukin and Dieter Bimberg, *Rev. Mod. Phys.* **71**, 1125 (1999).

[68] Cahn J. W., *Acta Metallurgica* **9**, 795 (1961)

[69] Cahn J. W., *Acta Metallurgica* **10**, 179 (1962)

[70] Cahn J. W., *Acta Metallurgica*, **14**, 1685 (1966)

[71] Cahn J. W., *J. Appl. Phys.* **34,** *Acta Metallurgica*, **14**, 1685 (1966)

[72] Patrick M. Woodward, *Nature Mater.* **6**, 549 (2007)

[73] Cahn, J. W. *Acta Metallurgica* **9**, 795 (1961).

[74] Cahn, J. W. *Acta Metallurgica* **10**, 179 (1962).

[75] Haskell, R. W. *Journal of the American Ceramic Society* **56**, 355 (1973).

[76] Morral, J. E. & Cahn, J. W. *Acta Metallurgica* **19**, 1037 (1971).

[77] Seol, D. J. et al. *Acta Materialia* **51**, 5173 (2003).

[78] Monette, L. *International Journal of Modern Physics B* **8**, 1417 (1994).

[79] Ragone, Therm. of Mater. Vol. I, John Wiley (1995)

[80] Cahn J, *J. Appl. Phys.,* **34**, 3581, (1963).

[81] Iwama, Y. & Takeuchi, M. *Transactions of the Japan Institute of Metals* **15**, 371 (1974)

[82] Mebed, A. M. & Howe, J. M. *Journal of Applied Physics* **100** (2006).

[83] Greaney, P. A., Chrzan, D. C., Clemens, B. M. & Nix, W. D. *Applied Physics Letters* **83**, 1364 (2003).

[84] Tanaka, K., Ichitsubo, T. & Koiwa, M. *Materials Science and Engineering a-Structural Materials Properties Microstructure and Processing* **312**, 118 (2001).

[85] Yeo, S. et al. *Appl. Phys. Lett.* **89**, 233120 (2006).

[86] Zhang, C. L. et al. *Appl. Phys. Lett.* **90**, 133123 (2007).

[87] Zhang, C. L. et al. *Appl. Phys. Lett.* **91**, 233110 (2007).

[88] Guiton, B. S. & Davies, P. K. *Nature Mater.* **6**, 586 (2007).

---

[89] Matsen M. Wand Schick M. *Phys. Rev. Lett.* **72**, 2660 (1994)

[90] Madelung O. , Rössler U.and Schul M. Z, Landolt-Börnstein - Group III Condensed Matter, V 41E, 1-7,springer, 2000

[91] Li F., Wang H., Wang L.and Wang J., *J. Mag. Mag. Mat.* **309**, 256 (2007)

[92] Forster R. H. and Hall E. O., *Acta Cryst*. **18**, 857, (1965)

[93] Nagarajan V., Jia C. L., Kohlstedt H., and Waser R., Misirlioglu I. B., Alpay S. P., Ramesh R., *Appl. Phys. Lett,* **86**, 192910 (2005)

[94] Choi K. J., Biegalski M., Li Y. L., Sharan A., Schubert J., Uecker R., Reiche P., Chen Y. B., Pan X. Q., Gopalan V., Chen L.-Q., Schlom D. G., Eom C. B., *Science*, 3**06**, 1005 (2004)

[95] Mabud S. A. andGlazer A. M., *J. Appl. Cryst.* **12**, 49, (1972)

[96] Mcurrie R.A., *Ferromagnetic Materials*, vol. 3, E.P. Wohlfarth, ed. North Holland, Amsterdam, (1982)

[97] Takahashi M., Guimarae J.R.and Fine M.E., *J. Amer. Cera. Soci.*, **54,** 291 (1971)

[98] Herman H. and Maccrone R. K., *J. Amer. Cera. Soc.*, **55**, 50 (1972)

[99] Wise M., Kim J.S. and Johnson W.C., *Thin Solid Films* **243**, 151 (2005)

[100] Das, S.K.; Rey, A.D., *Macro. Theo. Sim.*, **15**, 6, 469 (2006)

[101] Ni, y., and Khachaturyan a., *Nature Mater.* **8**, 410-414 (2009)

[102] Zhen, L.; Sun, X.Y.; Xu, C.Y.; Lu, L.X.; Qin, L.-C., *J. Mag. Mag. Mat.,* **06**, 69 (2006)

[103] Baibich, M.N.; Miranda, M.G.M.; da Rosa, A.T.; Hinrichs, R.; Golla-Schindler, U.; Antunes, A.B.; Martinez, G.; Estevez-Rams, E., *Physica B*,.**384,** 175 (2006)

[104] Li, H.F.; Ramanujan, R.V., *IEEE Transactions on Nanotechnology*, **5**, 295 (2006)

[105] Ostberg, G.; Jansson, B.; Andren, H.-O., *Scripta Materialia*, **54**, 4, 595 (2006)

[106] Enomoto, M., *Materials Transactions*, **46**, 6, 1088 (2005)

[107] Fukushima, T.; Sato, K.; Katayama-Yoshida, H.; Dederichs, P.H., *Physica Status Solidi A*, **203**, 2751 (2006)

[108] Van Suchetelen J., *Philips Res. Rep.*, **27**, 28 (1972)

[109] Nan C W, Liu G., Lin Y. and Chen H., *Phys. Rev. Lett.* **94**, 197203 (2005)

[110] Van den Boomgaard J. and Born R. A. J., *J. Mater. Sci.*, **13** 1538 (1978)

---

[111] Zheng H., Zhan Q., Zavaliche F., Sherburne M., Straub F., Cruz M. P., Chen Long-Qing, Dahmen U. and Ramesh R., *Nano Lett.* **6**, 1401 (2006)

[112] Chang K. S., Aronova M. A., Lin C. L., Murakami M., Yu M. H., Hattrick-Simpers J., Famodu O. O., Lee S. Y., Ramesh R., Wuttig M., Takeuchi I., Gao C., and Bendersky L. A., *Appl. Phys. Lett.* **84**, 3091 (2004)

[113] Van den Boomgaard J. and Born R. A. J., *J. Mater. Sci.* **13** 1538 (1978)

[114] Prellier W., Rajeswari M., Venkatesan T., and Greene R., *Appl. Phys. Lett.* **75**, 1446 (1999)

[115] Thomas K. A., de Silva P. S., Cohen L. F., Hossain A., Rajeswari M., Venkatesan T., Hiskes R., and MacManus-Driscoll J. L., *J. Appl. Phys.* **84**, 3939 (1998)

[116] Cullity B.D., *Introduction to Magnetic Materials* (Addison Wesley, Reading, MA, 1972)

[117] Koch A. J. J., Van der Steeg M. G., and Devos K. J., *Proceedings 1956 Conference on Magnetism and Magnetic Materials* (AIEE Technical Publication T-91, 173, 1957)

[118] Parker R. J., *Advances in Permanent Magnetism* (Wiley,New York, 1990)

[119] Nesbitt E. A. and Williams A. J., *Proc. 1956 Conf. Magnetism and Magnetic Materials* (AIEE Tech. Publ. T-91, 184, 1957)

[120] Iwama Y., and Takeuchi M., *Trans. Japan Inst. Meta.* **15**, 371 (1974)

[121] Holm E. A., Srolovitz D. J. and Cahn J. W. *Acta Meta, Mater.* **41**, 1119 (1993)

[122] Calzada ML and Milne S J, *J. Mater. Sci. Lett.* **12**,1221 (1993)

[123] Srinivasan G., Rasmussen E. T., Gallegos J., and Srinivasan R., *Phys.Rev. B* **64**, 214408 (2001)

[124] Morrison A.H. and Haneda K., *J. Appl. Phys.* **52,** 2496 (1981)

[125] Kim M.T., *Thin Solid Films* **283**, 12 (1996)

[126] Bozorth R. M. , Tilden E. F.,Williams A.J., *Phys. Rev.* **99**, 1788 (1955)

[127] Kimura T., Goto T., Shintani H., Ishizaka K., Arima T., and Tokura Y., *Nature* **426**, 55 (2003)

[128] Grimmer H., *Acta Cryst.* A**48**, 266 (1992)

[129] Fiebig, M. *J. Phys. D* **38**, R1 (2005)

---

[130] Spaldin, N. A. and Fiebig, M. *Science* **309**, 391 (2005)

[131] Schubert, U., Hu sing, N., Lorenz, A. *Chem. Mater.* **7**, 2010 (1995)

[132] Judeinstein, P., Sanchez, C. J. *Mater. Chem.* **6**, 511 (1996)

[133] Fredrickson,G. H., Bates, F. S., *Annu. Rev. Mater. Sci.* **26**,501 (1996)

[134] Bates, F. S., Fredrickson, G. H., *Phys. Today* **52**, 32 (1999)

[135] Muthukumar, M., Ober, C. K., Thomas, E. L., *Science* **277**, 1225 (1997)

[136] Hashimoto, T., Shibayma, M., Fujimura, M., Kawai, H., *in Block Copolymers,* (Science and Technology, Harwood Academic, London 1983), pp. 63-108

[137] Yu, K., Hurd, A. J., Eisenberg, A., Brinker, C. J., *Langmuir* **17**, 7961 (2001)

[138] Templin, M. *et al.*, *Science* **278**, 1795 (1997)

[139] Lee, J., Orilall, M. C., Warren, S. C. *et al.*, *Nature Mate.* **7**, 222 (2008)

[140] Fasolka, M. J., Mayes, A. M., *Annu. Rev. Mater. Res.* **31**, 323 (2001)

[141] Kim, S. O., Kim, B. H., *Macromolecules* **39**, 5466 (2006)

[142] Kim, D. H., Jia, X., Lin, Z., Guarini, K. W., Russell, T. P., *Adv. Mater.* **16**,702 (2004)

[143] Kim, D. H., Kim, S., Lavery, H. K., Russell, T. P. *Nano Lett.* **4**, 1841 (2004)

[144] Kim, D. H., Sun, Z., Russell, T. P., *Adv. Func. Mater.* **15**, 1160 (2005)

[145] Zhang, M., Yang, L., *Adv. Mater.* **19**, 1571 (2007)

[146] Kim, S., Briber, R. M., *Macromolecules* **40**, 4102 (2007)

[147] Kim, S. H. *et al.*, *Adv. Mater.* **16**, 226 (2004)

[148] Sundström, L., Krupp, L. *Appl. Phys. Lett.* **88**, 243107 (2006)

[149] Calzada, M. L. and Milne, S. J. *J. Mater. Sci. Lett.* **12**,1221 (1993)

[150] Vasiliu, F., Lucuta, P. Gr., Constantinescu, F., *Physica Status Solidi (a),* **80**, 637 (2006)

[151] Thang, P.D., Rijnders, G. and Blank, D. H. A., *J. Mag. Mag. Mat.*, **310,** 2621 (2007)

[152] Kingon, A. I and Srinivasan, S., *Nature Mater.*, **4**, 233 (2005)

[153] Pramanik, N., Fujii, T., Nakanishi, M. and Takada, J., *J. Mater. Sci.*, **40**,4169 (2005)

---

[154] Ramirez, A.P. in *Geometrical frustration* (Handbook of Magnetic Materials, Volume 13, Chapter 4, 2001) pp 423-520

[155] Bozorth, R. M. *Ferromagnetism* (IEEE Press, Piscataway, NJ, 1993).

[156] Morrison, A. H. and Hanada, K. *J. Appl. Phys.* 52, 2496 (1981).

[157] Wang, Q. M. and Ding, Y., *Appl. Phys. Lett.* **86**, 162903 (2005)

[158] CMI Inc., (available at http://www.gwyddion.net/).

[159] F. Liu, N. Goldenfeld, *Phys. Rev.* **A39**, 4805 (1989).

[160] J. J. Christensen, A.J. Bray, *Phys. Rev.* **E58**, 5364 (1998).

[161] L. M. Liz-Marzan, M. Giersig, P. Mulvaney, *Langmuir* **12**, 4329 (1996).

[162] Y. Lu, H. Fan, A. Stump, T. Ward, T. Rieker, C. Brinker, *Nature* **398**, 223 (1999).

[163] S. Kim, W. Zhang, T. J. Pinnavaia, *Science* **282**,1302 (1998).

[164] S.Warren, F. Disalvo, U. Wiesner, *Nature Mater.*, **6**, 156 (2007).

[165] Matsen, M.W. *Macromolecules* **28**, 5765 (1995)

[166] Dagotto, E., Nanoscale Phase Separation and Colossal Magnetoresistance (Berlin: Springer, 2002)

[167] Stubican, V. S. & Schultz, A. H. *J. Am. Ceram. Soc.* **51**, 290 (1968).

[168] H. U Habermeier, *J. Phys.: Condens. Matter* **20**, 434228 (2008)

[169] Guiton, B.S. & Davies, P. K., *Nature Mater.* **6**, 586 (2007)

[170] Garcia-Martin, S., Urones-Garrote, E., Knapp, M. C., King, G.,Woodward, P. M. *J. Amer. Chem. Soc.* **130,** 15028 (2008)

[171] Yeo, S., Horibe, Y., Mori, S., Tseng, C. M., Chen, C. H., Khachaturyan, A. G., Zhang, C. L., Cheong, S.-W. *Appl. Phys. Lett.* **89**, 233120 (2006)

[172] Wang,Y., Martinez, I., Guyot, F., Liebermann, R., *Science*, **275**, 510 (1997)

[173] Van Suchtelen, J. *Philips Res. Repts,* **27**, 28 (1972)

[174] Echigoya, J., Hayashi, S., Obi, Y., *J. Mater. Sci.* **35,** 5587 (2000).

[175] Van Run, A. M. D. G., Terrell, D. R., Scholing, D. H., *J. Mater. Sci.* **9,** 1710 (1974)

[176] Ren, S. & Wuttig, M., *Appl. Phys. Letters* **91**, 083501 (2007)

[177] Van Den Boomgaard, J., Terrell, D. R., Born, R. A. J., Giller, H. F. J. I., *J. Mater. Sci.* **9,** 1705 (1974)

---

[178] Ren, S. & Wuttig, M., *Appl. Phys. Lett.* **92,** 083502 (2008)

[179] Avellaneda, M. & Harshe, G., *J. Intel. Mater. Syst. Struct.* **5,** 501 (1994).

[180] Lopatin, S., Lopatina, I.& Lisnevskaya, I., *Ferroelectrics* **162,** 63 (1994)

[181] Kimura, T. et al. *Nature* **426**, 55 (2003).

[182] Lottermoser, Th. et al. *Nature* **430**, 541 (2004).

[183] Eerenstein, W., Wiora, M., Prieto, J. L., Scott, J. F., Mathur, N. D,. *Nature Mater.* **6**, 348 (2007)

[184] Ren, S. Q., Weng, L. Q., Song, S.H., Li, F., *J. Mater. Sci.* **40,** 4375 (2005)

[185] Burbank, R.D and Evans, H.T., *Acta. Cryst.* **1**, 330 (1948)

[186] Ni, Y. and Khachaturyan, A., *Nature Mater.,* **8**, 410 (2009)

[187] Wu, Y., Wang, S., Lu, H., *J. Am. Ceram. Soc.*, **89**, 3778-3787 (2006)

[188] Duffy, W., Cheng, B., Gabbay M., Fantozzi, G., *Metal. Mater. Tran.* A **26**, 1735 (1995)

[189] Folen, V. J., in Landolt-Börnstein, vol. 3, part 4b, Magnetic and Other Properties of Oxides and Related Compounds (Springer, Berlin, Heidelberg, New York, 1970)

[190] Viehland, D., Li, J. F., Cross, L. E., Wuttig, M., *Phys. Rev. B* **46**, 8013 (1992)

[191] Hemberger, J., Lunkenheimer, P., Fichtl, R., Krug von Nidda, H.-A., Tsurkan, V., Loidl, A., *Nature* **434**, 364 (2005)

[192] Samara, G. A. *J. Phys. Condens. Matter* **15**, 367 (2003)

[193] Cross, L. E., *Ferroelectrics* **76**, 241 (1987)

[194] Valenzuela, R. Magnetic ceramics (Cambridge university press, Cambridge, 1994)

[195] Chikazumi, S., Physics of Magnetism, 2nd edition, (Oxford Univ. Press 1997, p. 491)

[196] Wang, X., Deng, X., Wen, H., Li, L., *Appl. Phys. Lett.* **89**, 162902 (2006)

[197] Kumar, A., Sharma, G., Katiyar, R., Pirc, R., Blinc, R., Scott, J. F., arXiv:0812.3875v2 (2009)

[198] Hur, N., Park, S., Sharma, P.A., Ahn, J.S., Guha, S., Cheong, S-W., *Nature* **429,** 394 (2004)

[199] Ye, ZG, Schmid, H. *Ferroelectrics* **162**, 119 (1994)

---

[200] Brinker C.J., Scherer G.W., *Sol-Gel Science: The Physics and Chemistry of Sol-Gel Processing*, Academic Press, New York, (1990)

[201] Corriu R. J. P., Leclerq D., *Angew. Chem. Int. Ed. Engl.,* **35**, 1420 (1996)

[202] Schubert U., *J. Chem. Soc., Dalton Trans.,* 3343, (1996)

[203] C. Roger, M. Hampden-Smith, *Chemtech*, 26, (1993)

[204] http://www.chemat.com/html/solgel.html

[205] http://materials.web.psi.ch/Research/Thin_Films/Methods/Spin.htm

[206] Maiwa H. and Ichinose N, *Jpn. J. Appld. Phys Part 1*-Regular papers, short notes and review papers **39**, 5403 (2000)

[207] Buhlman S, Dwir B, Baborowski J, and Muralt P, *Appl. Phys. Lett.* **75**, 3195 (2002)

[208] Nagarajan V., et al., *Appl. Phys. Lett.* **81**, 4215 (2002)

[209] http://www.mechmat.caltech.edu/~kaushik/park/1-3-0.htm

[210] Traynor D S, Hadnagy D T., and Kammerdiner L, *Integrated Ferroelectrics* **16**, 63 (1997)

[211] http://layer.uci.agh.edu.pl/maglay/wrona/ang/index.php?go=badania_obszerne

---

Publications

1. **Shenqiang Ren,** Mark Laver and Manfred Wuttig,"*Nanolamellar Magnetoelectric $BaTiO_3$-$CoFe_2O_4$ Bi-Crystal*" Submitted to Adv. Func. Mater., 07, 2009.
2. **Shenqiang Ren,** Robert M. Briber and Manfred Wuttig, "*Self-Organized Magnetolectric 2D Onions* " Appl. Phys. Lett., 94, 113507 (2009); selected by Virtual Journal of Nanoscale Science & Technology, 30, 19 (2009)
3. **Shenqiang Ren**, Robert M. Briber and Manfred Wuttig, "*Diblock Copolymer Based Self-Assembled Nanomagnetoelectric*" Appl. Phys. Lett. 93, 173507 (2008); selected by Virtual Journal of Nanoscale Science & Technology, 18, 20 (2008)
4. **Shenqiang Ren** and Manfred Wuttig, "*Magnetoelectric nano-Fe_3O_4 $CoFe_2O_4$//$PbZr_{0.53}Ti_{0.47}O_3$ Composite*", Appl. Phys. Lett. 92, 083502 (2008); selected by Virtual Journal of Nanoscale Science & Technology, 17, 10 (2008)
5. **Shenqiang Ren** and Manfred Wuttig, "*Spinodally Synthesized Magnetoelctrics*" Appl. Phys. Lett. 91, 083501 (2007).
6. **Shenqiang Ren** and Manfred Wuttig, "*Self-Assembled Highly Tunable Magnetoelectric*", SMASIS**,** 417 (2008)
7. S. Lim, M. Murakami, W. Sarney, **Shenqiang Ren**, A.Varatharajan, V. Nagarajan, S. Fujino, M. Wuttig, I. Takeuchi, and L.G. Salamanca-Riba, "*The Effects of Multiphase Formation on Strain Relaxation and Magnetization in Multiferroic $BiFeO_3$ Thin Films*" Adv. Func. Mater. 17, 14, 2594-2599 (2007).

Conference Presentations

1. **Shenqiang Ren,** Robert M. Briber and Manfred Wuttig; **"***Bottom up Magnetoelectric Nanostructures***"** Oral Presentation, MRS Spring meeting, 2009, San Francisco, CA.
2. **Shenqiang Ren,** Robert M. Briber and Manfred Wuttig; **"***Self-Organized Magnetolectric 2D Onions***"** Oral Presentation, APS March meeting, 2009, Pittsburgh, PA.
3. **Shenqiang Ren,** Robert M. Briber and Manfred Wuttig; **"***Solution Processed Multiferroic Nanostructure through Diblock Copolymer Self-Assembly***"** Oral Presentation, MRS Fall meeting, 2008, Boston, MA.
4. **Shenqiang Ren**, Robert M. Briber and Manfred Wuttig, "*Diblock Copolymer Self-organization Based Two Phase Magnetoelectric*", Maryland Nanoday, May 14th , 2008, College Park, MD
5. **Shenqiang Ren** and Manfred Wuttig; **"***Spinodally Synthesized Multiferroics***"** Oral Presentation, MRS Fall meeting, 2007, Boston, MA.
6. **Shenqiang Ren** and Manfred Wuttig; "*Multiferroic $Pb(Zr_{0.53}Ti_{0.47})O_3$/$NiFe_2O_4$ Sol-gel Thin Films* " MRS Fall meeting, 2006, Boston, MA.